1-1-2014

# The Role of the Exocyst in Membrane Deformation, Cell Migration and Exocytosis

Yuting Zhao
*University of Pennsylvania*, yuting_zhao@hotmail.com

# The Role of the Exocyst in Membrane Deformation, Cell Migration and Exocytosis

**Abstract**
Dynamic shape changes of the plasma membrane are fundamental to many processes ranging from morphogenesis and cell migration to phagocytosis and viral propagation. In this study, I showed that Exo70, a component of the exocyst complex, induces tubular membrane invaginations towards the lumen of synthetic vesicles in vitro and generates actin-free protrusions on the surface of cells. Analyses using Exo70 mutants suggest that Exo70 generates negative membrane curvature through an oligomerization-based mechanism. The membrane-deformation function of Exo70 is likely to be independent of the other exocyst subunits. Exo70 thus represents a novel membrane-deforming protein for plasma membrane remodeling. Directional cell migration requires the coordination of actin assembly and membrane remodeling. Exo70 directly interacts with and activates the Arp2/3 complex, a central nucleating factor for the generation of branched actin networks for cell morphogenesis and migration. Here I found that both the stimulatory effect of Exo70 on Arp2/3 and the membrane-deformation function of Exo70 are required for lamellipodia formation and maintaining directional persistence of cell migration. Exo70 thus may couple actin dynamics and plasma membrane remodeling during cell migration. The late stage of exocytosis is regulated by the exocyst and SNARE complexes. The secretory vesicles are first tethered to the plasma membrane by the exocyst and then docked and fused to the plasma membrane by SNARE complex. Here I showed that the exocyst component Sec3, based on its sequence similarity to a SNARE-binding protein amisyn, directly binds to the plasma membrane SNARE Syntaxin4. Both Sec3 and amisyn binds to PI(4,5)P2 through basic residues on the N-terminus. Sec3 may regulate MMP and VSV-G exocytosis in cells. These results reveal a novel direct interaction between the exocyst and the plasma membrane SNARE and suggest that Sec3 may regulate the SNARE activity during exocytosis.

**Degree Type**
Dissertation

**Degree Name**
Doctor of Philosophy (PhD)

**Graduate Group**
Biology

**First Advisor**
Wei Guo

**Keywords**
Actin, Cell migration, Exocyst, Membrane curvature, SNARE complex, Vesicle trafficking

**Subject Categories**
Cell Biology

# THE ROLE OF THE EXOCYST IN MEMBRANE DEFORMATION, CELL MIGRATION AND EXOCYTOSIS

Yuting Zhao

A DISSERTATION

in

Biology

Presented to the Faculties of the University of Pennsylvania

in

Partial Fulfillment of the Requirements for the

Degree of Doctor of Philosophy

2014

| **Supervisor of Dissertation** | **Graduate Group Chairperson** |
| --- | --- |
| _____ | _____ |
| Wei Guo | Doris Wagner |
| Associate Professor of Biology | Professor of Biology |

**Dissertation Committee**

David S. Roos, E. Otis Kendall Professor of Biology

Tatyana Svitkina, Associate Professor of Biology

Erfei Bi, Professor of Cell and Developmental Biology

Michael S. Marks, Professor of Pathology and Laboratory Medicine

Paul Janmey, Professor of Physiology and Bioengineering

## ACKNOWLEDGEMENTS

I would like to express my gratitude to all the people who make my graduate study possible, meaningful and enjoyable.

First, I would like to give my deepest gratitude to my supervisor Dr. Wei Guo. He is truly enthusiastic for science and extremely broad-minded. He has shown me his way to do research and how to do it efficiently and effectively. He has also given me great supports and encouragements during these years. He has shaped me into a cell biologist.

Second, I really appreciate all the members in my thesis committee: Drs. David Roos, Tatyana Svitkina, Erfei Bi, Mickey Marks, and Paul Janmey. They have committed much time and efforts to help my research and have always been a constant source of constructive suggestions and encouragements.

Third, I want to thank my collaborators who contribute greatly to my research. I want to thank Dr. Jianglan Liu for the collaboration on Exo70 projects, for all the scientific discussions and the efforts to work out the manuscripts. I want to thank Drs. Changsong Yang and Tatyana Svitkina for all the help on fluorescence and electron microscopy since my rotation in Svitkina lab. I want to thank Dr. Ben Capraro for his help on giant unilamellar vesicles (GUVs) experiment. I want to thank Dr. Ravi Radhakrishnan and his group member Ryan P. Bradley, and Dr. N. Ramakrishnan, for the inspiring collaboration on simulation studies on Exo70-membrane interaction *in silico*. I

also want to thank Dr. Yujie Sun for the collaboration using stochastic optical reconstruction microscopy (STORM) to study Exo70-membrane interaction in cells.

Next, I want to give my gratitude to all the current and former members of Guo lab. They have made the lab a convivial place to work. In particular, I am grateful to Peng Yue for the discussions on Sec3 projects. I am grateful to the former lab manager Jian Zhang for all her help. I am grateful to the former lab fellow Dr. Bing He for all the advices and discussions. I also want to say special thanks to lab gals for the company, especially during dinner at school.

I would also like to extend thanks to the people who have been instrumental in completion of this work. I want to thank Ruchira Ranaweera and Dr. Yide Mei in Dr. Xiaolu Yang lab for the help on gel filtration assay. I want to thank Dr. Shaohui Huang for the help on FRAP experiment. I want to thank Dr. Clara Franzini-Armstrong for the help on rotary-shadowing EM.

Last but not least, I thank all my family and friends. I really appreciate my mother Ying Li and my father Wenquan Zhao for their endless care and support all these years. I sincerely appreciate my classmates and friends at Penn who make the journey of graduate study full of joys.

## ABSTRACT

## THE ROLE OF THE EXOCYST IN MEMBRANE DEFORMATION, CELL MIGRATION AND EXOCYTOSIS

Yuting Zhao

Wei Guo

Dynamic shape changes of the plasma membrane are fundamental to many processes ranging from morphogenesis and cell migration to phagocytosis and viral propagation. In this study, I showed that Exo70, a component of the exocyst complex, induces tubular membrane invaginations towards the lumen of synthetic vesicles in vitro and generates actin-free protrusions on the surface of cells. Analyses using Exo70 mutants suggest that Exo70 generates negative membrane curvature through an oligomerization-based mechanism. The membrane-deformation function of Exo70 is likely to be independent of the other exocyst subunits. Exo70 thus represents a novel membrane-deforming protein for plasma membrane remodeling. Directional cell migration requires the coordination of actin assembly and membrane remodeling. Exo70 directly interacts with and activates the Arp2/3 complex, a central nucleating factor for the generation of branched actin networks for cell morphogenesis and migration. Here I found that both the stimulatory effect of Exo70 on Arp2/3 and the membrane-deformation function of Exo70 are required for lamellipodia formation and maintaining directional persistence of cell migration. Exo70 thus may couple actin dynamics and plasma membrane remodeling during cell migration.

The late stage of exocytosis is regulated by the exocyst and SNARE complexes. The secretory vesicles are first tethered to the plasma membrane by the exocyst and then docked and fused to the plasma membrane by SNARE complex. Here I showed that the exocyst component Sec3, based on its sequence similarity to a SNARE-binding protein amisyn, directly binds to the plasma membrane SNARE Syntaxin4. Both Sec3 and amisyn binds to $PI(4,5)P_2$ through basic residues on the N-terminus. Sec3 may regulate MMP and VSV-G exocytosis in cells. These results reveal a novel direct interaction between the exocyst and the plasma membrane SNARE and suggest that Sec3 may regulate the SNARE activity during exocytosis.

## TABLE OF CONTENTS

**LIST OF FIGURES**

# CHAPTER 1 INTRODUCTION

## 1.1 Membrane trafficking

Cells utilize membrane trafficking (a.k.a vesicle trafficking) to transport cargos from one membrane compartment to another. Secretory cargos such as hormones and neurotransmitters are packed in secretory vesicles, which are transported along the cytoskeleton, docked and fused with the plasma membrane to release the content. Membrane cargos such as receptors and ion channels are incorporated to their destination in a similar manner. Signal transduction of certain growth factors and hormones and uptake of nutrients are also mediated by vesicle trafficking. The biogenesis, maturation and maintenance of membrane organelles such as ER, Golgi and endosomes involve vesicle trafficking as well. The vesicle trafficking is crucial not only for cellular compartmentalization and function in a single cell, but also for cells to communicate with their environment in multicellular organisms. Deficiency in vesicle trafficking pathways leads to a full range of human diseases from metabolic diseases such as diabetes (Leto and Saltiel, 2012) to neurodegenerative diseases such as Parkinson's disease (Esposito et al., 2012).

The molecular players of membrane trafficking have been identified and characterized during the past few decades by researchers, using genetic, biochemical, biophysical and cell biological approaches. In 2013, Drs. James E. Rothman, Randy W. Schekman, and Thomas C. Südhof were awarded the Nobel Prize in Physiology or Medicine for their discoveries of the machinery regulating vesicle trafficking. These

molecules involved in vesicle trafficking include small GTPases, coat proteins, tethering factors, SNAREs (short for soluble N-ethylmaleimide–sensitive factor attachment protein receptors), their regulators and others. In general, as illustrated in Figure 1.1 (adapted from Cai et al., 2007), vesicles which are coated with coat proteins are budded from the donor compartment. Vesicles thus formed are transported along the cytoskeleton towards the destination. Tethering factors mediate the initial interaction between the vesicles and the target membrane while the SNAREs mediate the fusion of the two membranes. Small GTPases such as Rabs regulate the specificity of the donor and target membranes as well as the activities of lipids, coat proteins and tethering factors (Cai et al., 2007; James et al., 2008; Starai et al., 2008; Ohya et al., 2009). Proteins such as the Sec1/Munc18 (SM) family proteins and NSF (short for N-ethylmaleimide–sensitive factor) regulate the assembly and disassembly of SNARE complexes repectively (Weber et al., 1998; Shen et al., 2007; Jahn and Scheller, 2006; Rizo and Südhof, 2012). The multi-layer regulations assure the fidelity and efficiency of vesicle trafficking.

### 1.2 The exocyst complex

The exocyst is an octameric protein complex consisting of Sec3, Sec5, Sec6, Sec8, Sec10, Sec15, Exo70 and Exo84. The exocyst complex was originally identified from the budding yeast Saccharomyces cerevisiae by genetic and biochemical approaches and later found to be evolutionarily conserved in higher eukaryotic cells (Hsu et al., 2004; Munson and Novick, 2006).

The exocyst is localized in a polarized fashion to sites of active exocytosis and cell surface expansion, acting as a tethering factor for post-Golgi vesicles to the plasma membrane (He and Guo, 2009; Heider and Munson, 2012). Based on the tertiary structure, it belongs to the CATCHR (complexes associated with tethering containing helical rods) family (Yu and Hughson, 2010; Spang, 2012). The other members of CATCHR family include COG (conserved oligomeric Golgi) complex acting at the Golgi, GARP (Golgi-associated retrograde protein) complex at endosomes, and Dsl1 complex at ER. Recent studies have revealed partial structural information of the exocyst component Exo70 (Dong et al., 2005; Hamburger et al., 2006; Moore et al., 2007), Exo84 (Dong et al., 2005), Sec15 (Wu et al., 2005), Sec6 (Sivaram et al., 2006), COG component Cog2 (Cavanaugh et al., 2007) and Cog4 (Richardson et al., 2009), GARP component Vps53 (Vasan et al., 2010) and Vps54 (Pérez-Victoria et al., 2010), and the Dsl1 complex (Ren et al., 2009). As shown in Figure 1.2, these CATCHER tethering factors share a similar fold consisting of α-helical bundles; this fold is also seen in the cargo-binding domain of the yeast myosin V motor Myo2p (Pashkova et al., 2006) and the MUN domain of Munc13, which is required for priming synaptic vesicles (Pei et al., 2009; Croteau et al., 2009; Li et al., 2011).

The major role of the exocyst is thought to be tethering post-Golgi vesicles to the plasma membrane for exocytosis (Figure 1.3A). Inhibition of the exocyst in yeast cells leads to vesicle accumulation in bud tips and growth defects (Novick and Guo, 2002; Hsu et al., 2004). In mammalian cells, loss of function of exocyst components results in blockade of vesicle trafficking or cargo incorporation to target membranes, such as

**Figure 1.1**

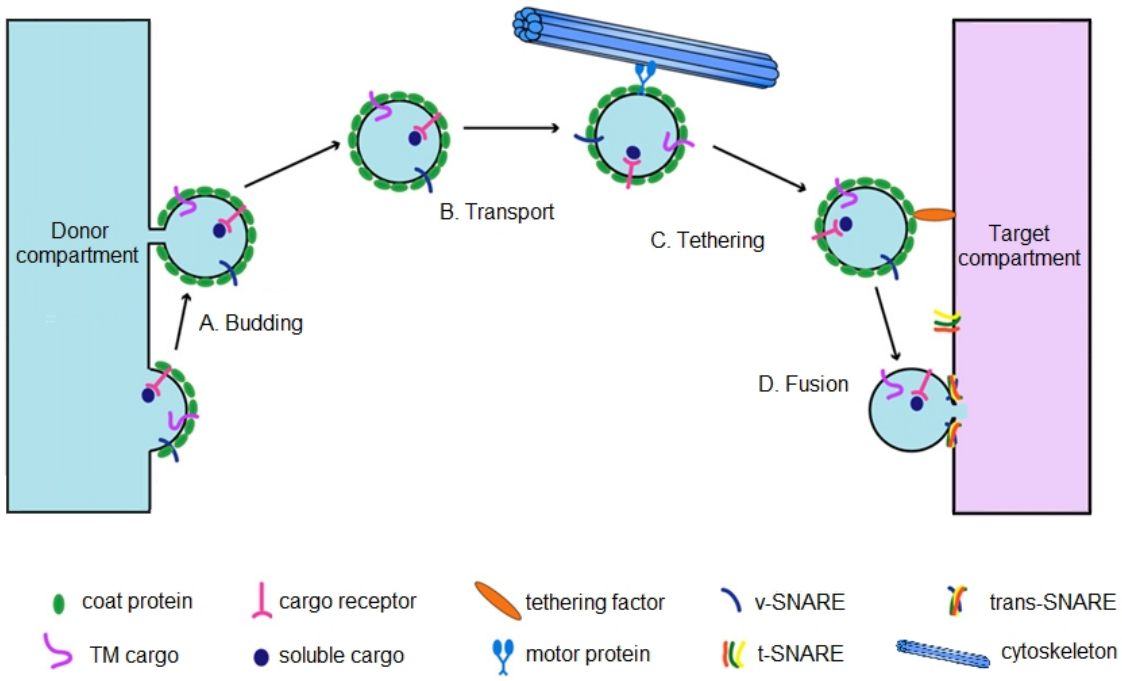
Donor compartment
A. Budding
B. Transport
C. Tethering
Target compartment
D. Fusion
coat protein
cargo receptor
tethering factor
v-SNARE
trans-SNARE
TM cargo
soluble cargo
motor protein
t-SNARE
cytoskeleton

**Figure 1.1 The major steps in vesicle trafficking**

Four steps are essential for vesicle trafficking. **(A)** Budding: coat proteins are recruited onto the donor membrane and the formation of a vesicle is initiated. Cargo and SNAREs are incorporated into the budding vesicle by interacting with coat subunits or adaptor proteins. **(B)** Transport: the vesicle moves toward the acceptor compartment by diffusion or on a cytoskeletal track. **(C)** Tethering: tethering factors work in conjunction with upstream regulators Rab GTPases to tether the vesicle to their target membrane. **(D)** Fusion: the vesicle-associated SNARE (v-SNARE) and the SNARE on the target membrane assemble (t-SNARE) into a four-helix bundle trans-SNARE complex, which drives membrane fusion and the delivery of cargo. Figure is adapted from Cai et al., 2007.

**Figure 1.2**

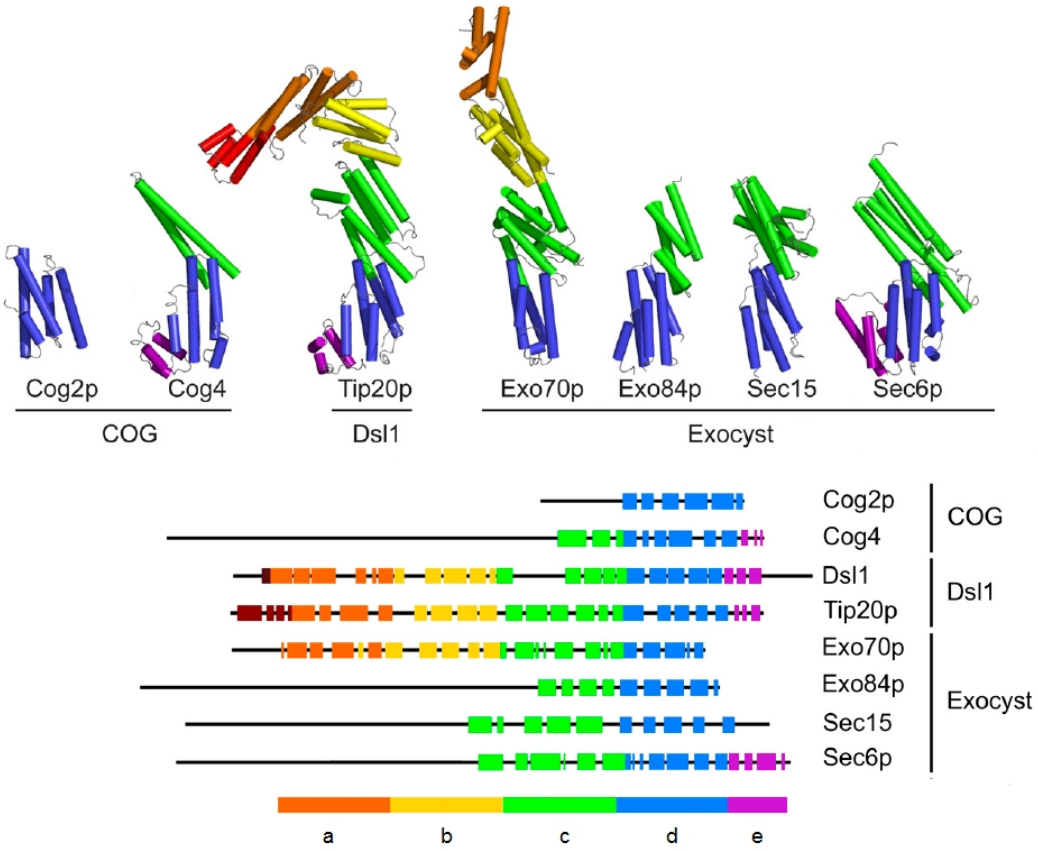
Cog2p
Cog4
Tip20p
Exo70p
Exo84p
Sec15
Sec6p
COG
Dsl1
Exocyst
Cog2p
Cog4
Dsl1
Tip20p
Exo70p
Exo84p
Sec15
Sec6p
COG
Dsl1
Exocyst
a
b
c
d
e

**Figure 1.2 Structural similarities among CATCHR tethering factors**

Structures and α-helical bundle domain organizations of CATCHR tethering factors COG, exocyst and Dsl1p subunits: Cog2p (PDB ID: 2JQQ), Cog4 (3HRO), Dsl1(combined model of 3K8P and 3ETU), Tip20p (3FHN), Exo70p (2PFV), Exo84p (2D2S), Sec15 (2A2F), and Sec6p (2FJI). Figure is adapted from Richardson et al., 2009 and Pérez-Victoria et al., 2010.

**Figure 1.3**

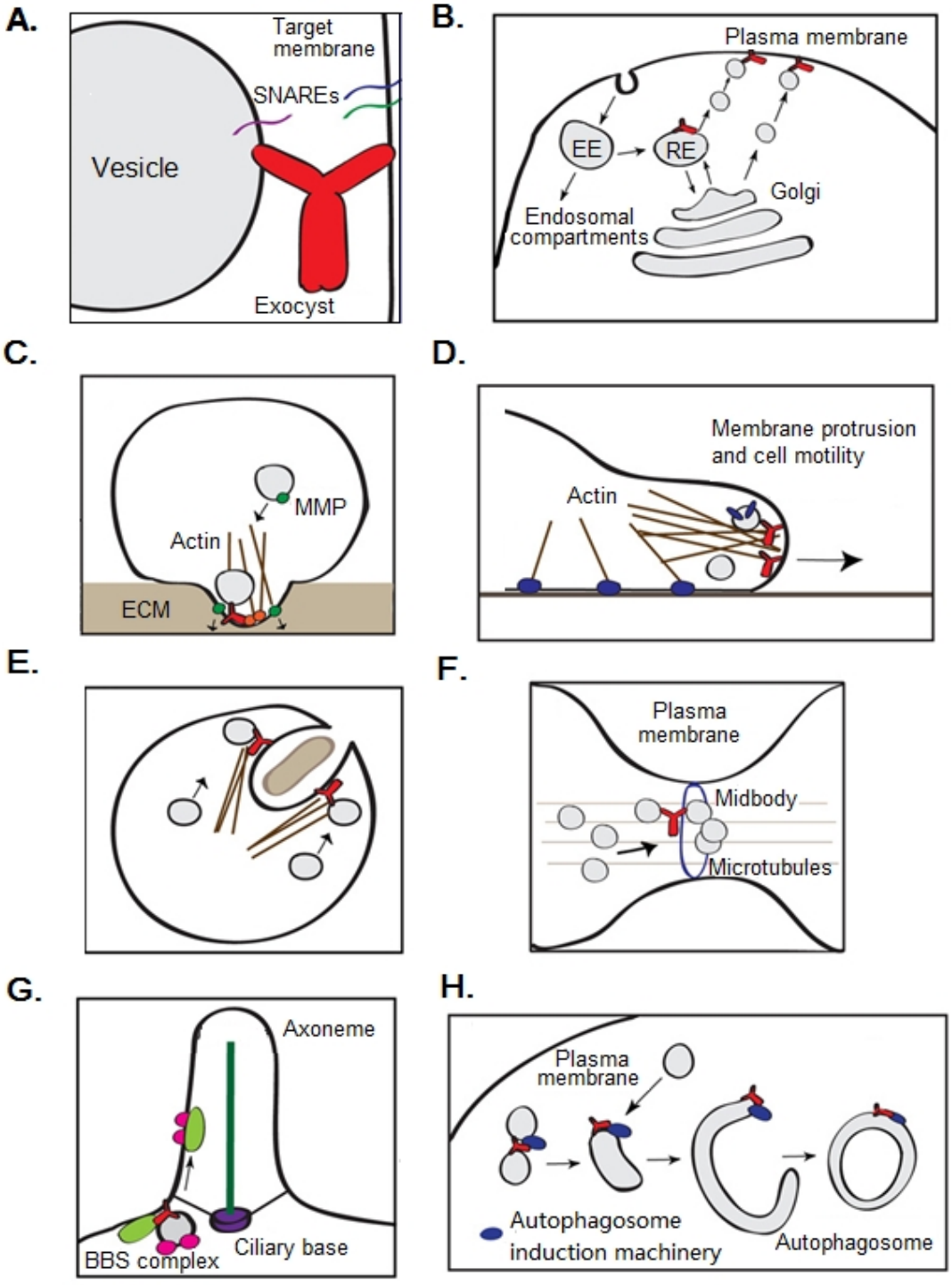
A.
Target membrane
SNAREs
Vesicle
Exocyst
B.
Plasma membrane
EE
RE
Golgi
Endosomal compartments
C.
MMP
Actin
ECM
D.
Membrane protrusion and cell motility
Actin
E.
F.
Plasma membrane
Midbody
Microtubules
G.
Axoneme
BBS complex
Ciliary base
H.
Plasma membrane
Autophagosome induction machinery
Autophagosome

**Figure 1.3 The exocyst functions in a variety of cellular processes**

**(A)** The exocyst is thought to form an initial connection between vesicle and the plasma membrane through interactions with proteins and lipids on both surfaces. The interactions may bring the membranes close enough to promote SNARE complex formation and membrane fusion. **(B)** During polarized secretion, the exocyst tethers both exocytic vesicles generated at the Golgi apparatus such as GLUT4 transporter trafficking in adipocytes (Inoue et al., 2003) and vesicles that are being recycled to the plasma membrane from the recycling endosome (RE=Recycling Endosome; EE=Early Endosome) (Oztan et al., 2007). **(C)** The exocyst localizes in invadopodia and regulates the delivery of matrix metalloproteinases (MMPs) that degrade the extracellular matrix (ECM) (Sakurai-Yageta et al., 2008; Liu et al., 2009a). **(D)** The exocyst localizes to the leading edge of migrating cells and interacts with actin regulators (Zuo et al., 2006), and mediates the recycling of focal adhesion (blue) components to the rear (Thapa et al., 2012). **(E)** An invading pathogen mediates its entry into the cell by promoting localized membrane expansion mediated by the exocyst (Nichols and Casanova, 2010). **(F)** The exocyst is recruited to the middle body during cytokinesis for new membrane addition and abscission (Gromley et al., 2005). **(G)** The exocyst directs membrane and protein delivery to the ciliary base to promote ciliogenesis (Das and Guo, 2011; Feng et al., 2012) and the BBsome complex shuttles proteins into the cilium (Nachury et al., 2011). **(H)** The exocyst is implicated in the formation of the autophagosome (Bodemann et al., 2011). Figure is adapted from Heider and Munson, 2012.

GLUT4 transporter trafficking to the plasma membrane in adipocytes (Inoue et al., 2003), AMPA receptor trafficking to the postsynaptic membrane in neuronal cells (Gerges et al., 2006), and recycling to the basolateral and apical plasma membrane in epithelial cells (Oztan et al., 2007) (Figure 1.3B). The exocyst is also involved in other cellular processes when it is targeted to specialized regions of the cellular membrane (Figure 1.3C-H), for instance, invadopodia formation (Sakurai-Yageta et al., 2008; Liu et al., 2009a), directional cell migration (Zuo et al., 2006; Rosse et al., 2006; Spiczka and Yeaman, 2008; Liu et al., 2009a; Thapa et al., 2012; Ren and Guo, 2012), pathogen invasion (Nichols and Casanova, 2010), cytokinesis (Gromley et al., 2005), primary ciliogenesis (Das and Guo, 2011; Feng et al., 2012) and autophagy (Bodemann et al., 2011).

### 1.3 Membrane curvature

Cells can be shaped by proteins that directly bind to the plasma membrane and sense, induce, or stabilize its curvature (McMahon and Gallop, 2005; Zimmerberg and Kozlov, 2006; Frost et al., 2009; Baumgart et al., 2011). To describe the shapes of the membrane, the curvature of the membrane is defined as the reciprocal of its radius (C=1/R; C, curvature; R; radius of the vesicle); positive curvature corresponds to bulging towards the cytosol, while negative curvature buldges away from the cytosol (McMahon and Gallop, 2005; Zimmerberg and Kozlov, 2006). Membrane curvature can be generated by proteins via different mechanisms (Figure 1.4). For example, membrane proteins can bend the bilayer through their intrinsic shape; peripheral proteins can bend the membrane by

## Figure 1.4

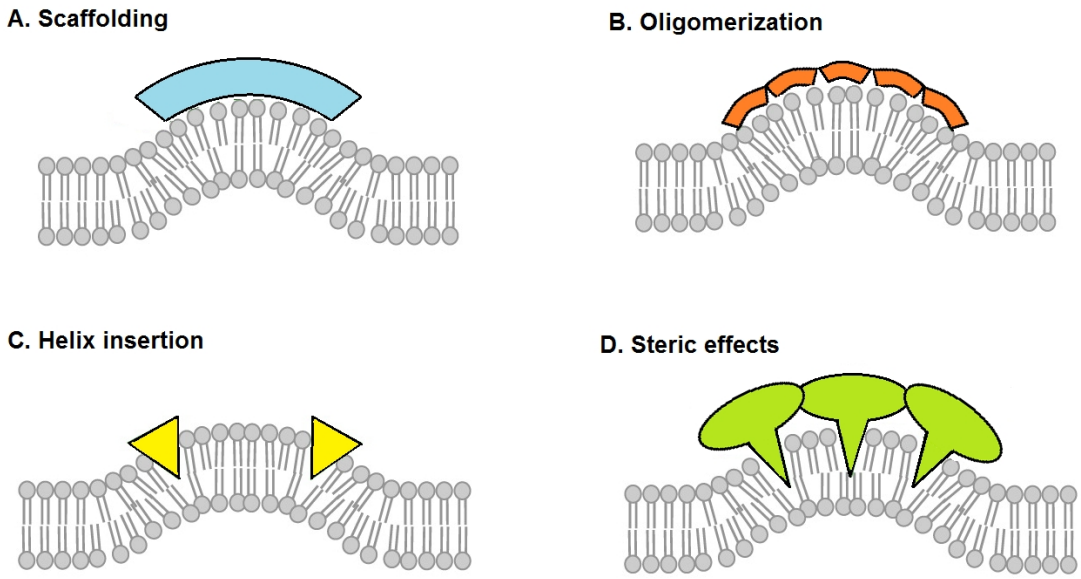
A. Scaffolding
B. Oligomerization
C. Helix insertion
D. Steric effects

**Figure 1.4 Mechanisms of membrane curvature generation by proteins**

**(A)** Curvature generation by peripheral proteins with an intrinsic curvature, e.g., BAR domain of Amphiphysin (Peter et al., 2004). (B) Protein oligomerization can cooperatively amplify curvature generation, e.g., F-BAR domain of CIP4 (Frost et al., 2008). **(C)** Curvature generation by insertion of amphipathic helices to the membrane leaflet, e.g., ENTH domain of Epsin (Ford et al., 2002). **(D)** Crowding of proteins with high affinity binding to the lipids may also contribute to curvature generation (Stachowiak et al., 2010). Figure is adapted from Baumgart et al., 2011.

scaffolding and/or wedge (helix) insertion, as exemplified by the BAR domain superfamily proteins, Epsin and dynamin (McMahon and Gallop, 2005; Zimmerberg and Kozlov, 2006; Hinshaw et al., 1995; Takei et al., 1995; Farsad et al., 2001; Ford et al., 2002; Frost et al., 2008). Oligomerization of membrane deforming proteins can also amplify curvature induction (Baumgart et al., 2011).

The best characterized membrane-deforming proteins are BAR family proteins, which form oligomeric crescent-shaped domains that abut the membrane through their concave surfaces (McMahon and Gallop, 2005; Frost et al., 2009). They induce tubular extensions from synthetic vesicles in vitro and, in cells, cause invaginations of the plasma membrane towards the cytoplasm during processes such as endocytosis. On the other hand, most I-BAR (inverse-BAR) proteins bind to the membrane through their convex surface, and induce membrane tubules towards the lumen of the vesicles in vitro and generate surface protrusions such as filopodia in cells (Mattila and Lappalainen, 2008; Scita et al., 2008; Saarikangas et al., 2009; Zhao et al., 2011).

### 1.4 Leading edge protrusions and directional cell migration

Membrane protrusions at the leading edge are important for directional cell migration (Pollard and Borisy, 2003; Mattila and Lappalainen, 2008; Ridley, 2011). When cells are migrating, they first send out protrusions at the leading edge, adhere to the substratum, retract at the rear and move forward, and disassemble the adhesion in order to start a new cycle (Figure 1.5).

**Figure 1.5**

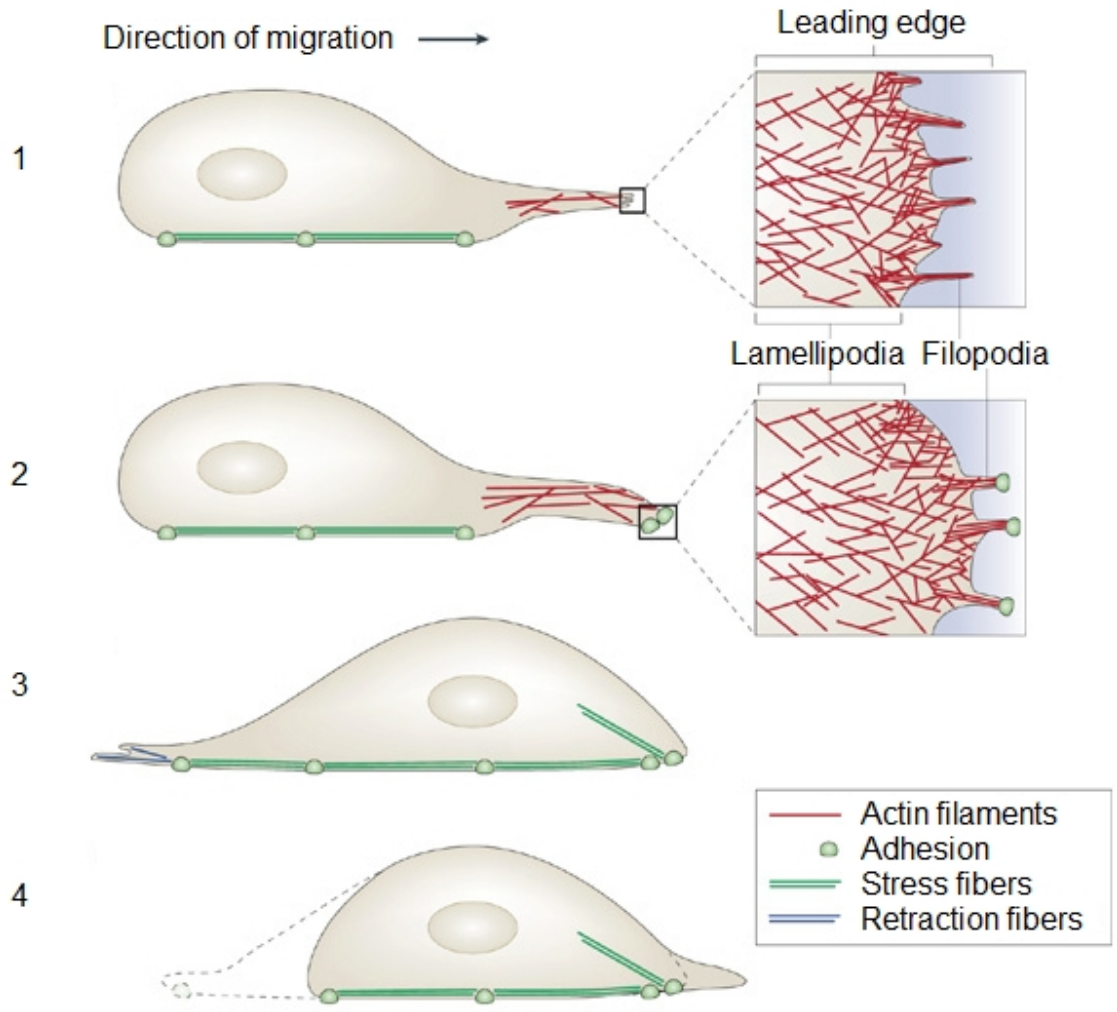
Direction of migration
Leading edge
1
Lamellipodia
Filopodia
2
3
4
Actin filaments
Adhesion
Stress fibers
Retraction fibers

**Figure 1.5 Leading edge protrusions and directional cell migration**

Directional cell migration usually involves a four-step cycle: (1) protrusion at the leading edge, (2) adhesion to the substratum, (3) retraction of the rear and translocation of the cell body, and (4) release of the adhesion. At the leading edge, lamellipodia contain branched actin filaments and filopodia contain bundled actin filaments. Figure is adapted from Mattila and Lappalainen, 2008.

Two major types of protrusions are found at the leading edge, thin sheet-like protrusions called lamellipodia and finger-like protrusions called filopodia (Figure 1.5). In lamellipodia, a branched actin network mediated by the Arp2/3 complex "pushes" the plasma membrane to generate surface protrusions, which is the physical step that initiates directional cell migration (Pollard and Borisy, 2003; Ridley, 2011). The Arp2/3 complex consists of seven subunits Arp2, Arp3, Arpc1, Arpc2, Arpc3, Arpc4 and Arpc5. In the presence of nucleation-promoting factors (NPFs), a monomeric actin is brought close to the Arp2 and Arp3 subunits of the Arp2/3 complex to form a heterotrimer, from which actin polymerization is initiated; the Arp2/3 complex binds to an existing actin filament, and the newly assembled actin filament makes a 70 degree branch (Goley and Welch, 2006; Campellone and Welch, 2010). Filopodia are exploratory extensions filled with parallel bundled actin filaments, which is mediated by another type of actin nucleator formin (Mattila and Lappalainen, 2008; Campellone and Welch, 2010). Actin assembly is thought to be the only driving force for membrane protrusions; however, recent studies reveal that membrane-deforming proteins may be sufficient to induce filopodia (Bereiter-Hahn, 2005; Suetsugu et al., 2006; Mattila et al., 2007; Ji et al., 2008; Yang et al., 2009; Guerrier et al., 2009), which argue for an active role of membrane dynamics in the formation of membrane protrusions.

The exocyst component Exo70 has been shown to directly interact with the Arpc1 subunit of the Arp2/3 complex (Zuo et al., 2006) and to kinetically stimulate Arp2/3-mediated actin polymerization and branching *in vitro* (Liu et al., 2012). Moreover, Exo70 directly interacts with the plasma membrane through $PI(4,5)P_2$ (Liu et al., 2007) and

induces filopodia protrusions (Zuo et al., 2006), similar to the membrane-deforming protein I-BAR domains (Suetsugu et al., 2006; Mattila et al., 2007; Yang et al., 2009) and srGAP2 F-BAR (Guerrier et al., 2009). Exo70 may serve as a great candidate to address how membrane dynamics and actin dynamics are coordinated at the leading edge.

### 1.5 Membrane fusion

The final step of vesicle trafficking is membrane fusion, which is mediated by the SNARE proteins. The SNARE complex is a four-helical bundle formed by cognate v- and t-SNAREs, which reside in donor and target membrane compartments, respectively; the formation of the SNARE complex brings close the two membranes and provides the driving force for membrane fusion (Jahn and Scheller, 2006; Martens and McMahon, 2008; Rizo and Südhof, 2012) (Figure 1.6).

SNARE-mediated fusion is tightly regulated by a variety of proteins and lipids, spatially and temporally. Recent studies have successfully reconstituted homotypic fusion processes, such as endosome fusion (Ohya et al., 2009) and yeast vacuole fusion (Stroupe et al., 2009), using purified components *in vitro*, which requires Rab GTPase, tethering factors (EEA1 for endosome and HOPS for yeast vacuole), SNAREs, SNARE chaperones, Sec1/Munc-18 (SM) proteins, and regulatory lipids. For heterotypic fusion, such as synaptic vesicles fusing to the plasma membrane, SM proteins (Scott et al., 2004; Shen et al., 2007; Ma et al., 2013), $Ca^{2+}$ -binding protein synaptotagmin-1 (Hui et al., 2009) and regulatory lipids (James et al., 2008), have been demonstrated to regulate SNARE-mediated fusion in reconstitution systems in vitro; however, it remains unclear

**Figure 1.6**

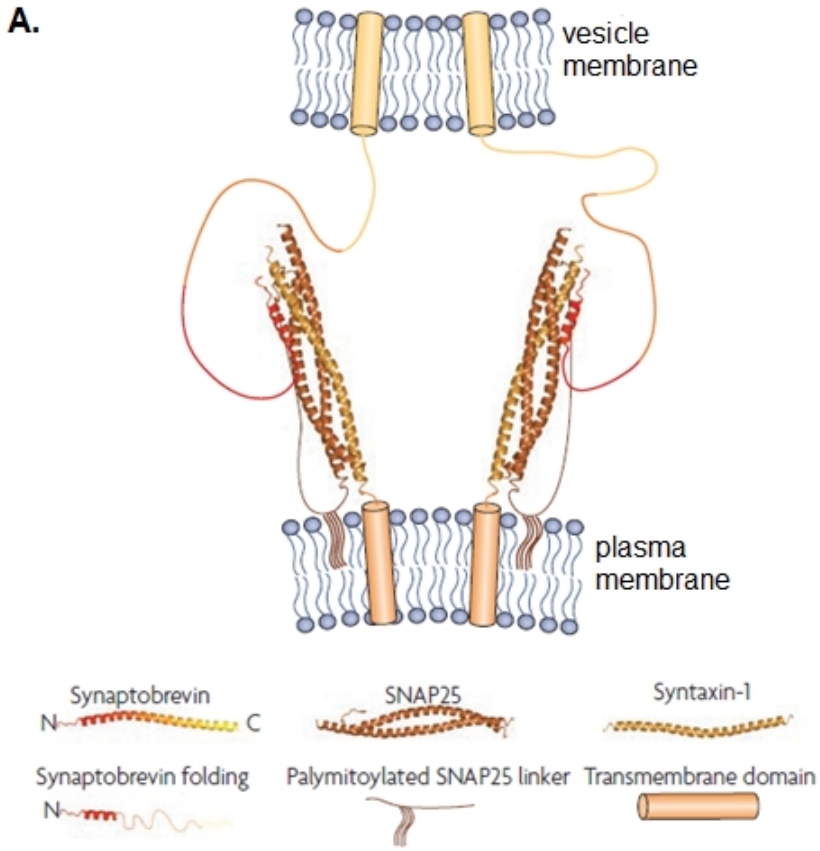
A.
vesicle membrane
plasma membrane
Synaptobrevin
N
C
SNAP25
Syntaxin-1
Synaptobrevin folding
N
Palymitoylated SNAP25 linker
Transmembrane domain
B.
Before fusion
After fusion
vesicle
vesicle
plasma membrane
plasma membrane

**Figure 1.6 SNARE complex mediates membrane fusion**

**(A)** The formation of SNARE complex between v-SNARE synaptobrevin on the vesicle membrane and t-SNAREs Syntaxin-1 and SNAP25 on the plasma membrane into a four-helical bundle. **(B)** SNARE complex drives the fusion between the vesicle membrane and the plasma membrane into one membrane. Figure is adapted from Martens and McMahon, 2008; Rizo and Südhof, 2012.

whether the tethering factors, especially the exocyst, are involved in heterotypic fusion like EEA1 and HOPS do for homotypic fusion to tether the vesicles and regulate the assembly of cognate SNARE complexes.

Several lines of evidence suggest that the exocyst complex may cross talk to the SNARE complex for exocytosis. In budding yeast, the exocytic SNARE complex (t-SNAREs: SSO1/2 + Sec9, v-SNARE: Snc1/2) assembly is blocked in exocyst mutants indicating that the exocyst acts upstream of SNARE (Grote et al., 2000). The yeast exocyst component Sec6p biochemically interacts with the yeast plasma membrane t-SNARE Sec9p (Sivaram et al., 2005). The exocyst and the plasma membrane SNAREs also share several binding partners such as SM family proteins(Wiederkehr et al., 2004; Zhang et al., 2005; Hattendorf et al., 2007; Bao et al., 2008). Some known SNARE binding proteins share sequence homology and structural similarity with the exocyst components. For example, Amisyn, a mammalian protein which contains a v-SNARE domain and binds to the plasma membrane t-SNAREs like Syntaxin 1A, is homologous to the Sec3 N-terminus (Scales et al., 2002). The MUN domain of the SM protein Munc-13, which binds to the t-SNARE complex of Syntaxin 1A and SNAP25(Guan et al., 2008) and regulates fusion activity (Ma et al., 2013), shows remote homology and structural similarity to the tethering complexes including the exocyst (Pei et al., 2009; Croteau et al., 2009; Li et al., 2011). Moreover, the Dsl1p complex, which is the tethering factor for Golgi-to-ER trafficking, directly stimulates the assembly of its cognate SNARE complex (Ren et al., 2009; Spang, 2012) and belongs to the CATCHR family of tethering factors

as the exocyst does. Taken together, the exocyst is a good candidate for the regulation of the activity of SNARE complex for exocytosis.

### 1.6 Thesis overview

The exocyst mediates post-Golgi vesicle tethering to the plasma membrane. It is associated with the membrane; but whether it actively participates in dynamic membrane events such as membrane protrusions and membrane fusion remains elusive. Accumulating evidence leads to my hypothesis that the exocyst plays a direct role in regulating membrane dynamics. In my thesis, I will address how the exocyst is involved in the plasma membrane remodeling and SNARE-mediated membrane fusion. Understanding these mechanisms not only reveals novel functions of the exocyst, but also sheds light on the molecular mechanisms by which cytosolic tethering factors regulate their target membranes in general.

In my thesis, Chapter 2 elaborates how the exocyst component Exo70 generates membrane curvature, and represents a novel class of membrane-deforming protein. Chapter 3 describes the role of Exo70 in regulating morphogenesis and directional cell migration, providing a case study of a protein that coordinates both membrane and actin dynamics. Chapter 4 discusses how the exocyst component Sec3, interacts with a t-SNARE on the plasma membrane for fusion, shedding light on how the tethering factor regulates heterotypic fusion.

# CHAPTER 2 EXO70 GENERATES NEGATIVE MEMBRANE CURVATURE

## ABSTRACT

Dynamic shape changes of the plasma membrane are fundamental to many processes ranging from morphogenesis and cell migration to phagocytosis and viral propagation. In this study, I showed that Exo70, a component of the exocyst complex, induces tubular membrane invaginations towards the lumen of synthetic vesicles in vitro and generates actin-free protrusions on the surface of cells. Analyses using Exo70 mutants suggest that Exo70 generates negative membrane curvature through an oligomerization-based mechanism. The membrane-deformation function of Exo70 is likely to be independent of the other exocyst subunits. Exo70 thus represents a novel membrane-deforming protein for plasma membrane remodeling.

## 2.1 INTRODUCTION

The shapes of the cells are integral to their physiological functions. Cells undergo dynamic shape changes during a variety of cellular processes such as phagocytosis, morphogenesis, viral propagation, and cell migration (McMahon and Gallop, 2005; Zimmerberg and Kozlov, 2006). Cells can be shaped by proteins that directly bind to the plasma membrane and sense, induce, or stabilize its curvature (McMahon and Gallop, 2005; Zimmerberg and Kozlov, 2006; Frost et al., 2009). The BAR family of proteins form oligomeric crescent-shaped domains that abut the membrane through their concave surfaces (McMahon and Gallop, 2005; Frost et al., 2009). They induce tubular extensions from synthetic vesicles *in vitro* and, in cells, cause invaginations of the plasma membrane towards the cytoplasm during processes such as endocytosis. On the other hand, most I-BAR (inverse-BAR) proteins bind to the membrane through their convex surface, and induce membrane tubules towards the lumen of the vesicles *in vitro* and generate surface protrusions such as filopodia in cells (Mattila and Lappalainen, 2008; Scita et al., 2008; Zhao et al., 2011). The curvatures generated towards the cytoplasm by BAR proteins are often termed as “positive curvature”, whereas those generated in the form of surface protrusions by I-BAR proteins are termed “negative curvature” (McMahon and Gallop, 2005; Zimmerberg and Kozlov, 2006).

The exocyst complex, consisting of Sec3, Sec5, Sec6, Sec8, Sec10, Sec15, Exo70 and Exo84, mediates the tethering of secretory vesicles at the plasma membrane for exocytosis and cell surface expansion (Hsu et al., 2004; Munson and Novick, 2006; He

and Guo, 2009). The exocyst is implicated in many cellular processes such as epithelia formation, cytokinesis, neurite branching and cell migration (He and Guo, 2009). One exocyst component Exo70 has a long rod-like structure that binds to $PI(4,5)P_2$ through positively charged residues on its surface (Dong et al., 2005; Hamburger et al., 2006; Moore et al., 2007; Liu et al., 2007). Overexpression of Exo70, but not any other subunit of the exocyst complex, induces filopodia formation in cells independent of its function in exocytosis (Zuo et al., 2006).

In this study, combining biochemical and cell biological analyses and mathematical simulations, I demonstrate that Exo70 induces negative membrane curvature through an oligomerization-based scaffolding mechanism similar to I-BAR proteins. In cells, Exo70 can induce actin-free protrusions, which requires the membrane-deformation by Exo70 but not the exocyst holo-complex. My study reveals a novel function of Exo70 in membrane deformation and membrane remodeling for morphogenesis.

## 2.2 RESULTS

### Exo70 induces membrane tubules towards the lumen of synthetic vesicles

Exo70 was previously shown to bind to $PI(4,5)P_2$ and associate with the cytosolic side of the plasma membrane (Liu et al., 2007; He et al., 2007). Moreover, overexpression of Exo70 induces membrane protrusions similar to the I-BAR proteins (Zuo et al., 2006; Mattila et al., 2007; Yang et al., 2009). I thus tested whether Exo70, like I-BAR, affects

membrane morphology under the same condition used in previous study (Mattila et al., 2007). Synthetic large unilamellar vesicles (LUVs) containing 30% PI(4,5)$P_2$ were incubated with recombinant Exo70 or the I-BAR domain of MIM. The morphology of these LUVs was then analyzed by transmission electron microscopy (EM). Strikingly, the LUVs incubated with GST-Exo70 displayed tubular invaginations that extended towards the lumen (Figure 2.1A). The average diameter of these membrane tubules was 68.8 ± 13.8 nm (Figure 2.1B). Exo70 without the GST tag also induced membrane invaginations (Figure 2.1C), albeit the average diameter of the tubules was smaller (49.5 ± 9.6 nm) (Figure 2.1B). The I-BAR domain of MIM induced membrane tubules that were slightly larger in diameter than those induced by Exo70 (76.1 ± 17.4 nm) (Figure 2.1A and 2.1B). As a negative control, GST had no effect on the LUVs, and the Exo70 (K571A/E572A) mutant, which is defective in PI(4,5)$P_2$ binding (Liu et al., 2007), failed to induce invaginations (Figure 2.1A). Three-dimensional reconstruction of the deformed LUVs using a series of tilted images demonstrated the connectivity of the tubular invaginations with the exterior (see arrow in Figure 2.1C). I have also performed the experiment using LUVs containing 5% PI(4,5)$P_2$. Exo70 induced invaginations, albeit the number of tubules was smaller than samples using LUVs containing 30% PI(4,5)$P_2$ (Figure 2.1D, the connectivity of the tubular invaginations with the exterior indicated by the arrow).

In addition to using LUVs and EM, I also investigated membrane tubulation induced by Exo70 using giant unilamellar vesicles (GUVs) containing 5% PI(4,5)$P_2$ and fluorescence-labeled lipids. The large size of GUVs and the fluorescence labeling allow the direct visualization of membrane deformation in real-time. As shown in Figure 2.2A,

**Figure 2.1**

**A.**

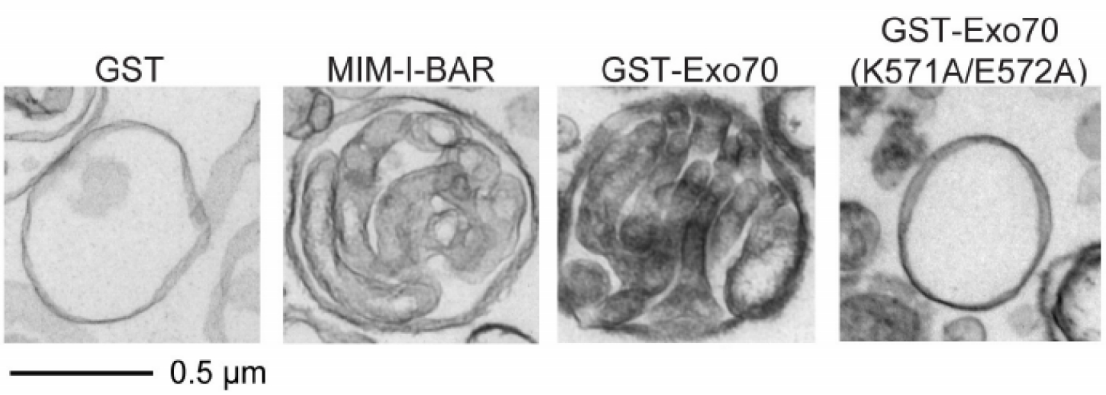


**B.**

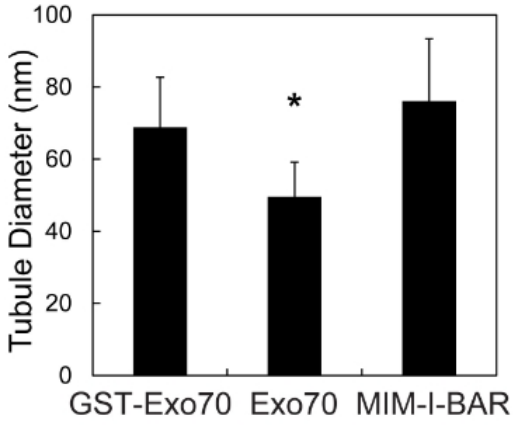


**C.**

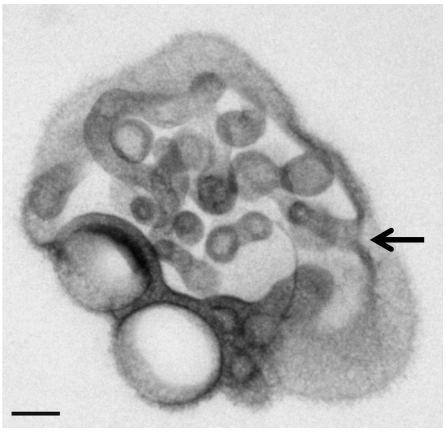


**D.**

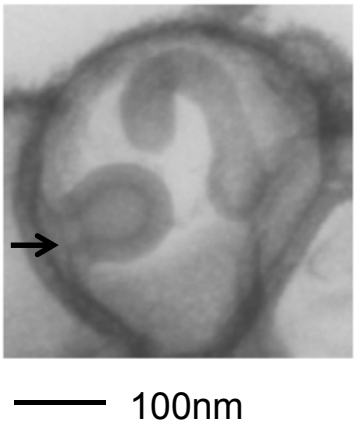

**Figure 2.1 Exo70 induces tubular invaginations on synthetic LUV vesicles**

**(A)** Transmission EM showing that GST-Exo70 induced tubular invaginations towards the interior of the lumen of LUVs similar to the MIM I-BAR domain. GST, GST-Exo70(K571A/E572A) did not induce any membrane tubules. See **MATERIALS AND METHODS** for details. Scale bar, 0.5 μm. **(B)** Comparison of the diameters of the membrane tubules induced by different proteins. Error bars represent standard deviation (SD). n=80; *, $p<0.01$. **(C-D)** Untagged Exo70 induced membrane invaginations. The arrow shows a representative region where the tubular invagination was connected to the exterior. LUVs contained **(C)** 30% $PI(4,5)P_2$ or **(D)** 5% $PI(4,5)P_2$. Scale bar, 100 nm.

**Figure 2.2**

**A.**

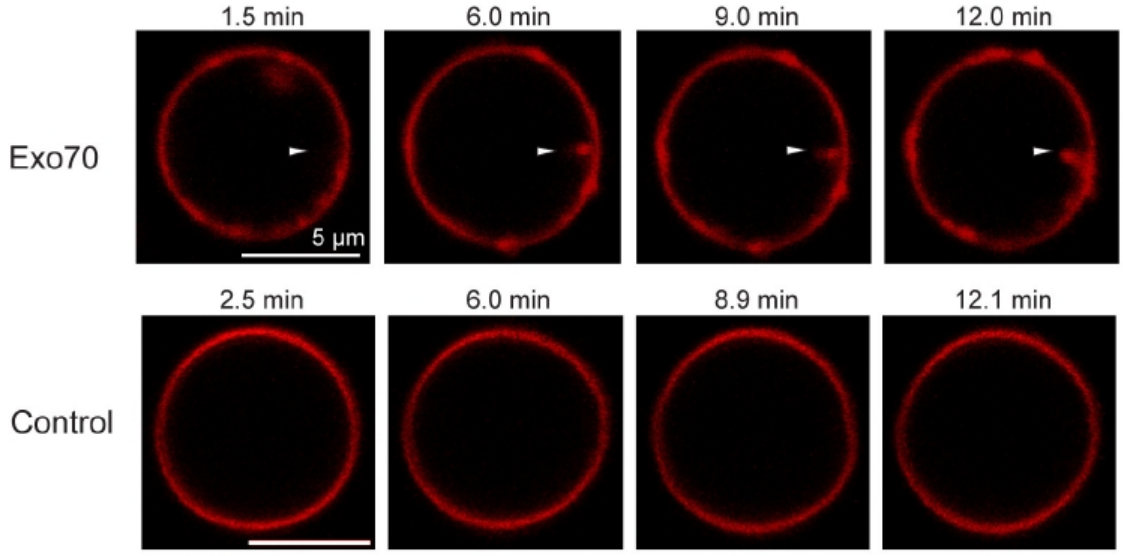


**B.**

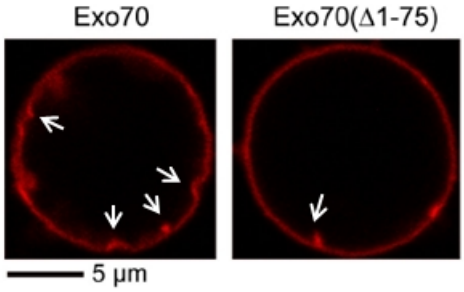


**C.**

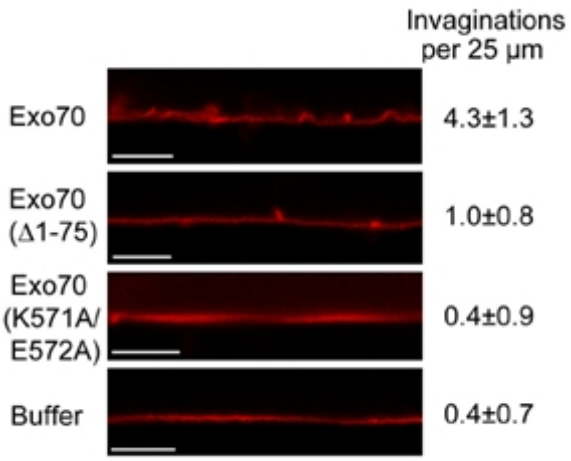

**Figure 2.2 Exo70 induces tubular invaginations on synthetic GUV vesicles**

**(A)** Confocal microscopy of fluorescence-labeled Giant Unilamellar Vesicles (GUVs) incubated with Exo70 (upper panel) or buffer control (lower panel). Sequential frames show the inward growth of a tubule (arrowhead) from a GUV incubated with Exo70. Scale bar, 5 μm. **(B)** Exo70 or Exo70(Δ1-75) was incubated with GUVs and subjected to confocal microscopy. Exo70(Δ1-75) induced much fewer invaginations (white arrows) than Exo70. **(C)** The contours of GUV membranes were linearized. The numbers of invaginations per 25 μm were calculated (average ± SD). Exo70(Δ1-75) and Exo70(K571A/E572A) induced much fewer invaginations than the full-length Exo70 ($n=10$; $p<0.01$). Scale bar, 5 μm.

addition of Exo70 induced inward growth of membrane tubules from these GUVs, which was not observed in the absence of Exo70.

**Oligomerization of Exo70**

BAR proteins usually deform membrane by forming α-helical dimers or oligomers that scaffold the negatively charged membranes (McMahon and Gallop, 2005; Frost et al., 2009; Zhao et al., 2011). I therefore examined the potential oligomerization of recombinant Exo70 by gel-filtration chromatography. The full-length Exo70 was distributed in high-molecular weight (MW) fractions (Figure 2.3A), suggesting that Exo70 formed oligomers. Sequence analysis by COILS program (Lupas et al., 1991) predicts that the N-terminus of Exo70 has a high probability to form a coiled-coil structure, which may participate in Exo70 oligomerization. I found that Exo70(Δ1-75), which lacks the N-terminal 75 amino acids, was distributed in low-MW chromatographic fractions, suggesting that Exo70(Δ1-75) is a monomer.

To further confirm the oligomerization of Exo70, I treated the fractions with the cysteine cross-linker $BM(PEG)_2$. A range of oligomeric species was detected in Exo70 but not Exo70(Δ1-75) samples (Figure 2.3B), suggesting that the high-MW fractions of Exo70 were indeed formed by oligomerization rather than due to the elongated shape of the protein.

I also tested the self-association of Exo70 by immunoprecipitation assay (Figure 2.3C). FLAG-tagged Exo70 and GFP-tagged Exo70 and Exo70(Δ1-75) were co-

**Figure 2.3**

**A.**

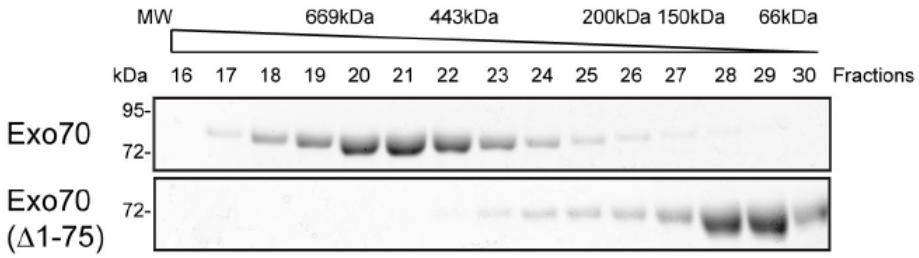


**B.**

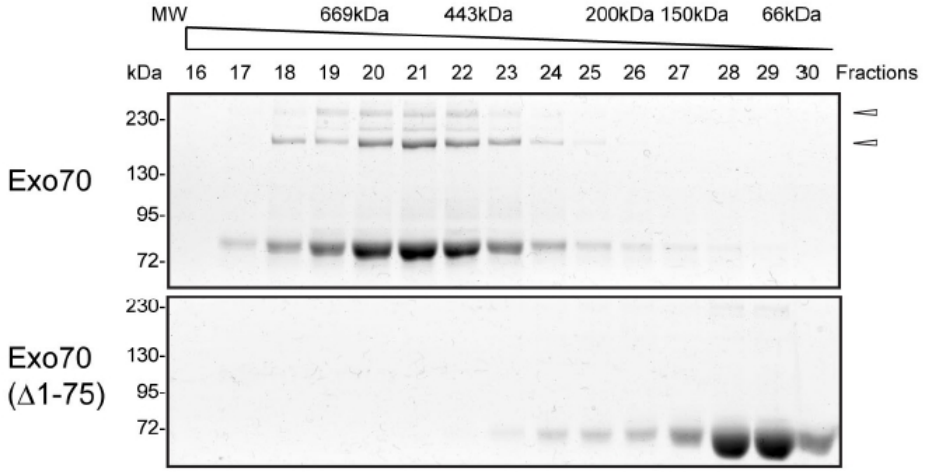


**C.**

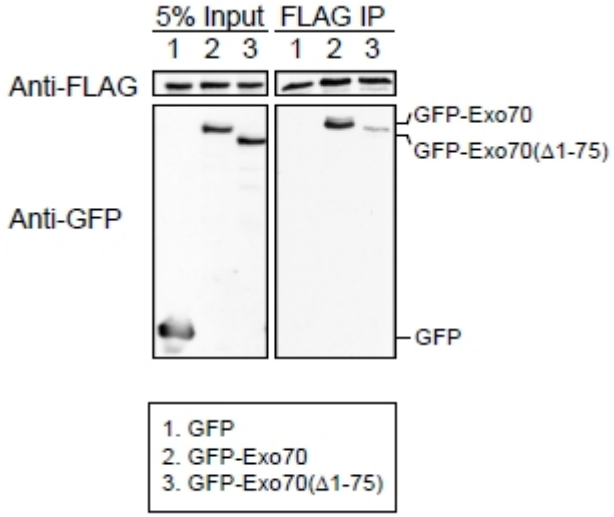

**Figure 2.3 Oligomerization of Exo70**

**(A)** Recombinant Exo70 proteins were loaded onto a Superdex 200 10/300GL column and eluted fractions were subjected to SDS-PAGE. Exo70, but not Exo70(Δ1-75), was eluted in high MW fractions. **(B)** Gel-filtration fractions were lightly treated with cross-linker $BM(PEG)_2$, which links proteins in vicinity. High MW species were observed in Exo70 but not in Exo70(Δ1-75) fractions. Arrowheads: Exo70 oligomers. **(C)** Lysates of HEK293T cell expressing Exo70-FLAG together with GFP, GFP-Exo70, or GFP-Exo70(Δ1-75) were incubated with anti-FLAG (M2) beads. The inputs and bound proteins were analyzed by Western blotting using anti-FLAG (upper panels) and anti-GFP monoclonal antibodies (lower panels). Exo70-FLAG was able to pull down GFP-Exo70, but to a much lesser extent, GFP-Exo70(Δ1-75).

expressed in HEK293T cells. Exo70-FLAG was able to pull down GFP-Exo70 and, to a much lesser extent, GFP-Exo70(Δ1–75). These results suggest that Exo70 can self-associate and the first 75aa are required for the self-association.

**Oligomerization and lipid binding of Exo70 is required for the generation of membrane tubules towards the lumen of synthetic vesicles**

The ability of Exo70(Δ1-75) to deform membrane was examined using fluorescence-labeled GUVs (Figure 2.2B). Exo70(Δ1-75) induced fewer invaginations than the full-length Exo70 (white arrows). To quantify the extent of membrane deformation among Exo70 variants, the contours of GUV membranes were linearized. The numbers of invaginations per 25 μm were calculated. As shown in Figure 2.2C, Exo70(Δ1-75) and Exo70(K571A/E572A) induced fewer invaginations than the full-length Exo70.

Exo70(K571A/E572A) is defective in $PI(4,5)P_2$ binding (Liu et al., 2007) and failed to induce membrane invaginations (Figure 2.1A and 2.2C), suggesting that membrane binding is required for membrane deformation. To test whether lipid binding is affected in the Exo70(Δ1-75) mutant, I performed a liposome co-sedimentation experiment (Figure 2.4). Exo70(Δ1-75) bound the liposomes to the same extent as Exo70 when the binding reached full capacity (150nM protein and 120 μM LUVs); in GUV deformation assay, both Exo70 and Exo70(Δ1-75) were present at a molar excess comparing to $PI(4,5)P_2$ thus the binding reached full capacity. Therefore, the reduced activity of Exo70(Δ1-75) in membrane deformation on GUV (Figure 2.2B) was likely

**Figure 2.4**

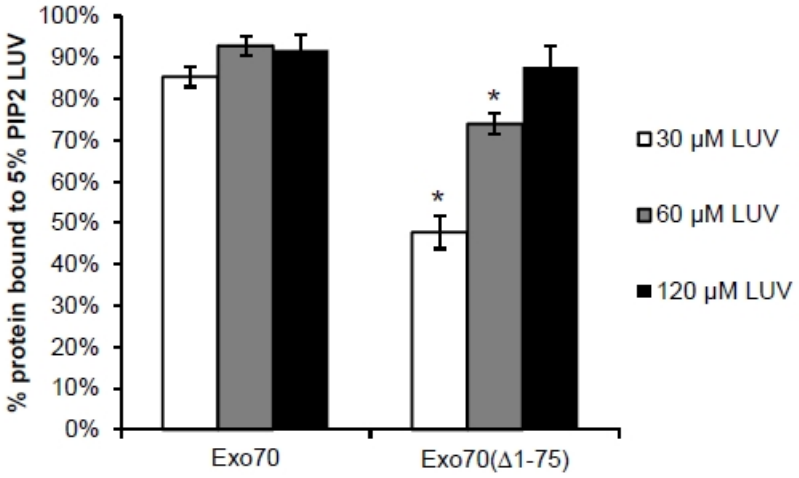
% protein bound to 5% PIP2 LUV
100%
90%
80%
70%
60%
50%
40%
30%
20%
10%
0%
*
*
Exo70
Exo70(Δ1-75)
30 μM LUV
60 μM LUV
120 μM LUV

**Figure 2.4 The effect of oligomerization of Exo70 on lipid binding**

Sucrose-loaded LUVs were prepared as described (Liu et al., 2007) except that the buffer used contained 20mM HEPES, pH 7.5, 150 mM NaCl, 1mM EGTA and 1mM DTT. 150 nM Exo70 or Exo70Δ(1-75) were mixed with 5% PI(4,5)$P_2$+95% DOPC or 100% DOPC LUVs at indicated concentration and centrifuged at 62,000 rpm for 30 min at 25°C in a TLA-100 rotor. The supernatants and pellets were subjected to 10% SDS-PAGE and stained with SYPRO-Ruby (Invitrogen) for quantification of bound and unbound materials with the Image J. The percentage of bound proteins to PI(4,5)$P_2$ LUVs were normalized to 100% DOPC LUVs. Three independent experiments were carried out; error bars, SD. Exo70Δ(1-75) bound less than the wild type to 30 and 60 μM LUVs (*, $p<0.01$), while bound equally to 120 μM LUVs as the wild type Exo70.

due to the defects in protein oligomerization and not to impaired lipid binding. Interestingly, oligomerization of Exo70 may cooperatively facilitate lipid binding since Exo70(Δ1-75) impaired lipid binding at lower LUV concentrations (Figure 2.4, in the presence of 30 and 60 μM LUVs).

The above results suggest that Exo70 employs a scaffolding mechanism to deform PI(4,5)$P_2$-containing membranes, which requires both membrane binding and protein oligomerization.

**Exo70 induces actin-free membrane protrusions in cells**

In cells, overexpression of membrane-deforming proteins often results in the formation of numerous tubules in the cytoplasm (for BAR proteins such as amphiphysin) (Takei et al., 1999; Peter et al., 2004) or protrusions at the cell surface (for I-BAR proteins such as IRSp53) (Mattila et al., 2007). The expression of these BAR proteins at non-physiological levels in cells had served to test their role in generating membrane curvatures *in vivo*. Exo70 overexpression was previously shown to induce filopodial protrusions (Zuo et al., 2006). The protrusions on the cell surface are topologically equivalent to the inward membrane tubules observed in the synthetic vesicles shown above in Figure 2.1 and Figure 2.2. However, filopodial protrusions on the cell surface also involve filamentous actin bundles (Mattila and Lappalainen, 2008). Therefore, a careful examination of these Exo70-induced protrusions is needed to better differentiate the contributions from actin and curvature induction, respectively.

Using time-lapse fluorescence microscopy, the dynamics of Exo70 and F-actin in filopodial protrusions induced by over-expressing GFP-Exo70 in B16F1 cells was examined (Figure 2.5A). GFP-Exo70 and F-actin (labeled by mCherry-Lifeact) frequently co-distributed along the entire length of filopodia and displayed coordinated dynamics (Figure 2.5B and 2.5D). Interestingly, there was a substantial fraction (20.8%) of GFP-Exo70-positive filopodia that were devoid of F-actin (Figure 2.5C-E). This phenotype was also observed previously with the overexpression of I-BAR domains, where ~10% actin-free protrusions were found (Yang et al., 2009). Here approximately 5% of the protrusions were first positive only with GFP-Exo70, and later filled with F-actin (Figure 2.5C and 2.5D).

I also performed line scan analysis of the GFP-Exo70-induced protrusions (Figure 2.6). For each protrusion, the fluorescence intensities of GFP-Exo70 and actin signals along the length of protrusion were measured, and estimated the Full Width at Half Maximum (FWHM) by Gaussian fitting using Matlab (Mathworks). The ratio between GFP-Exo70 and actin is above 1 in all protrusions analyzed (n=20), usually higher in the distal region of the protrusions, suggesting that the GFP-Exo70 signal is outside actin signal, especially at the tips.

While the wild-type GFP-Exo70 stimulated protrusion formation, the Exo70 mutants, Exo70(Δ1-75) (defective in oligomerization), Exo70(K571A/E572A) (defective in membrane binding) and Exo70(Δ628-630) (defective in binding the Arp2/3 complex) (Zuo et al., 2006; Liu et al., 2012) lost their ability to stimulate protrusions. Furthermore,

**Figure 2.5**

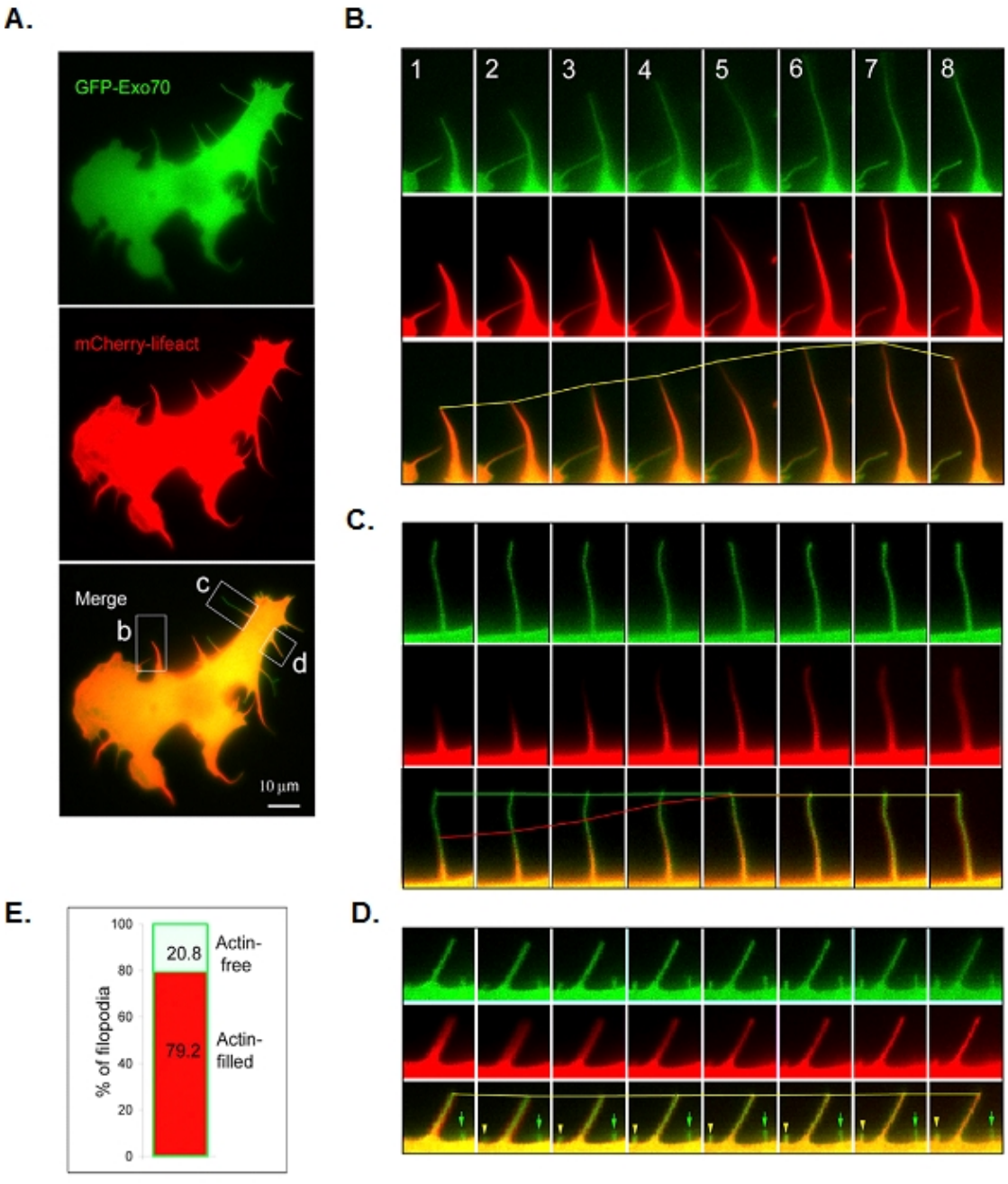
A.
GFP-Exo70
mCherry-lifeact
Merge
b
c
d
10 µm
B.
1
2
3
4
5
6
7
8
C.
D.
E.
% of filopodia
100
80
60
40
20
0
20.8
79.2
Actin-free
Actin-filled

**Figure 2.5 Dynamics of Exo70-induced filopodial protrusions**

**(A)** Overview of a B16F1 cell co-expressing GFP-Exo70 and mCherry-Lifeact (labeling F-actin). **(B-D)** Time-lapse microscopy showing dynamics of individual filopodia in Box b, c, d, of **(A)**. Time interval between frames is 42 seconds. The lines mark the most distal points of GFP-Exo70 (green) and actin (red) signals in the filopodia over time; the yellow lines indicate the coincidence of these signals. **(B)** For a regular filopodium, the dynamics of GFP-Exo70 and F-actin were indistinguishable. **(C)** While GFP-Exo70 signal was stationary, F-actin lagged behind and gradually filled the filopodium. **(D)** GFP-Exo70 and F-actin co-localized in the long stationary filopodium, whereas the nascent GFP-Exo70-positive filopodium (green arrow) was actin-free. In the same field, a new membrane protrusion (yellow arrowhead) was emerging and gradually filled with F-actin. **(E)** The percentage of filopodia completely filled with F-actin (red) and lacking F-actin (blue) in the interior. A total of 1687 filopodia in 31 cells were counted.

**Figure 2.6**

**A.**

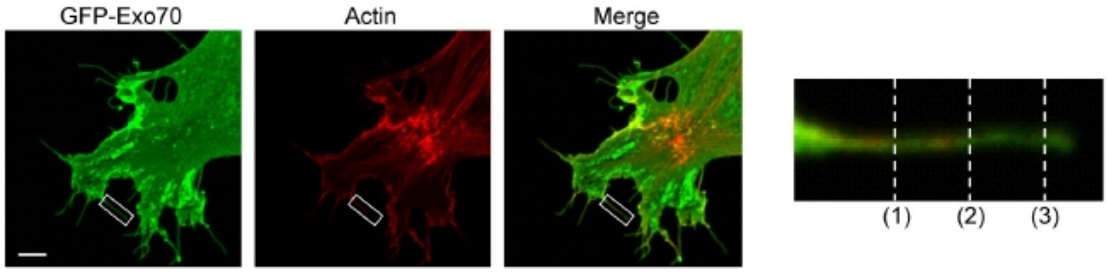


**B.**

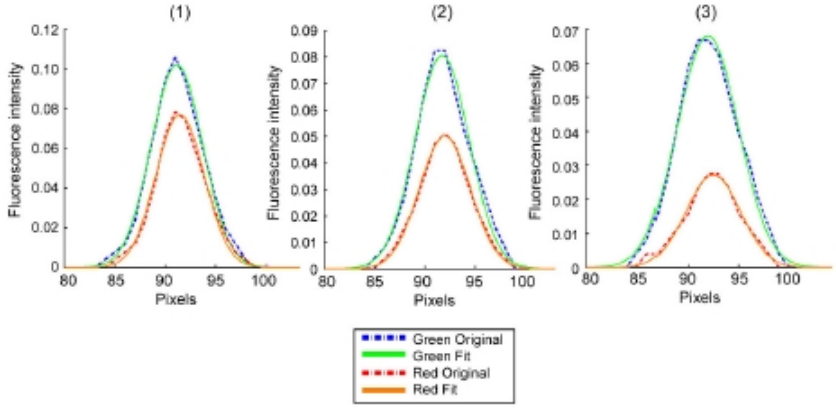


**C.**

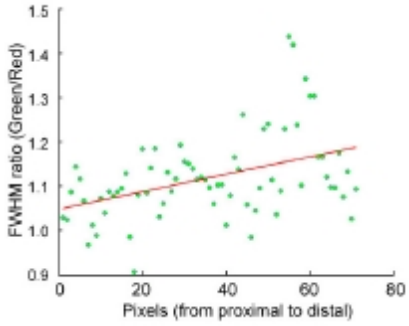

**Figure 2.6 Line analysis of Exo70-induced filopodial protrusions**

**(A)** A B16F1 cell expressing GFP-Exo70, the box region was enlarged and lines were drawn perpendicular to the filopodia for fluorescence intensity measurements. Scale bar, 5 μm. **(B)** Fluorescence intensity profiles of lines 1-3 in (**A**) (dashed lines) and Gaussian fitting (solid lines). **(C)** The Full Widths at Half Maximum (FWHMs) were estimated from the Gaussian fitting. The ratios of GFP-Exo70 over actin signals for each line perpendicular to the protrusion were plotted, which are above 1 in all filopodia analyzed (n=20), usually higher in the distal region.

**Figure 2.7**

**A.**

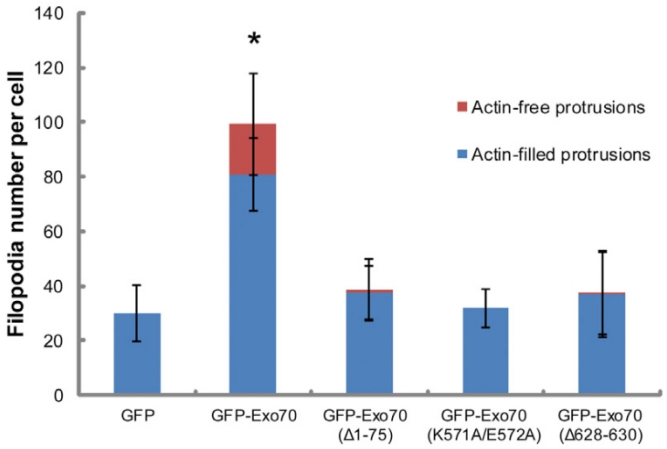


**B.**

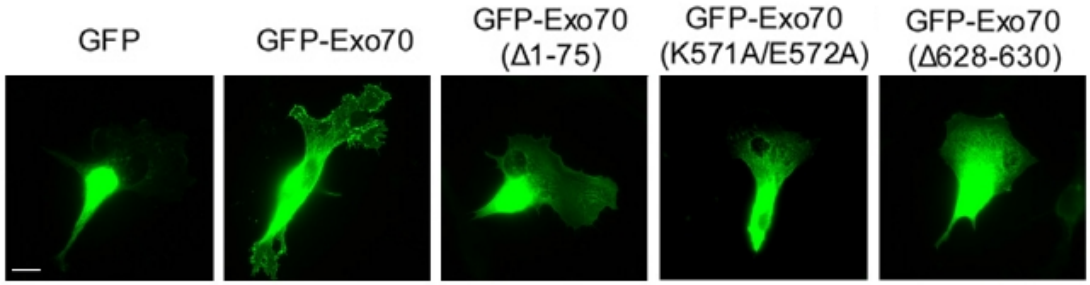


**C.**

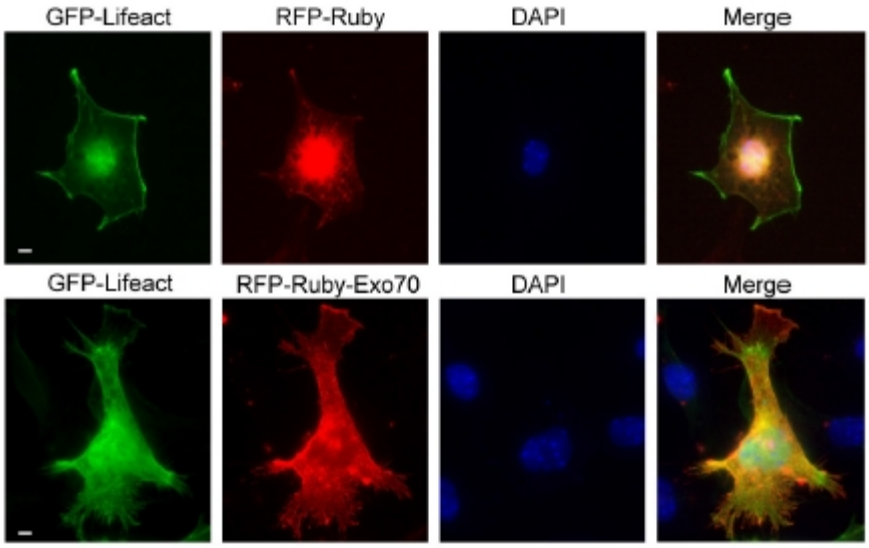

**Figure 2.7 Characterization of Exo70 variants in inducing filopodial protrusions**

**(A)** B16F1 cells expressing GFP-Exo70 variants were stained for F-actin. GFP-Exo70 induced significantly more filopodia than GFP or GFP-Exo70 mutants. In addition, approximately 20% of the GFP-Exo70-induced membrane protrusions were actin-free. Much lower percentages of the protrusions in cells expressing GFP or GFP-Exo70 mutants (see text for description of the mutants) were actin-free. Error bars, SD. n=10; *, $p<0.01$. **(B)** GFP-Exo70 variants were expressed in B16F1 cells. The wild type Exo70 induced numerous filopodia. Exo70(Δ1-75) (oligomerization-defective) and Exo70(Δ628-630) (Arp2/3-binding-defective), though associated with the plasma membrane, failed to induce filopodia. GFP-Exo70(K571A/E572A) ($PIP_2$-binding-defective) did not associate with the plasma membrane. Scale bar, 10 μm. **(C)** Exo70 was tagged by RFP-Ruby, a monomeric fluorescence protein. GFP-Lifeact was co-transfected with either RFP-Ruby-Exo70 or RFP-Ruby in B16F1 cells. Similar to GFP-Exo70, RFP-Ruby-Exo70 induced numerous protrusions. Scale bar, 5 μm.

in these cells, actin-free protrusions were barely detectable in the existing filopodia (Figure 2.7A and B). The formation of filopodia requires intact Exo70 functions.

In addition to GFP-tagged Exo70, the monomeric RFP-Ruby-tagged Exo70 induced membrane protrusions in a similar manner (Figure 2.7C). Therefore the generation of the observed protrusions was unlikely an artifact of GFP dimerization.

To examine the ultrastructure of actin in GFP-Exo70 induced protrusions, platinum replica EM was performed. For filopodia that did contain actin, there were fewer (2-4 filaments, usually more than 15 filaments in normal filopodia, Lewis and Bridgman, 1992) or loosely bundled actin filaments (data not shown). Correlative time-lapse fluorescence and platinum replica EM were performed on GFP-Exo70 expressing cells. Many filopodial protrusions were either empty or contained very few linear actin filaments (a representative cell shown in Figure 2.8).

The observations that Exo70 induces membrane protrusions devoid of actin are consistent with the *in vitro* finding of tubule generation inside the lumen of synthetic vesicles (Figure 2.1 and Figure 2.2) as they are topologically equivalent in the direction of tubulation ("negative curvature").

**Exo70 induces protrusions independent of other exocyst components**

To test whether the ability of Exo70 to stimulate membrane protrusion depends on the other members of the exocyst complex, I examined the filopodial protrusions in B16F1 cells in which Sec8 and Sec15 (two other components of the exocyst complex)

**Figure 2.8**

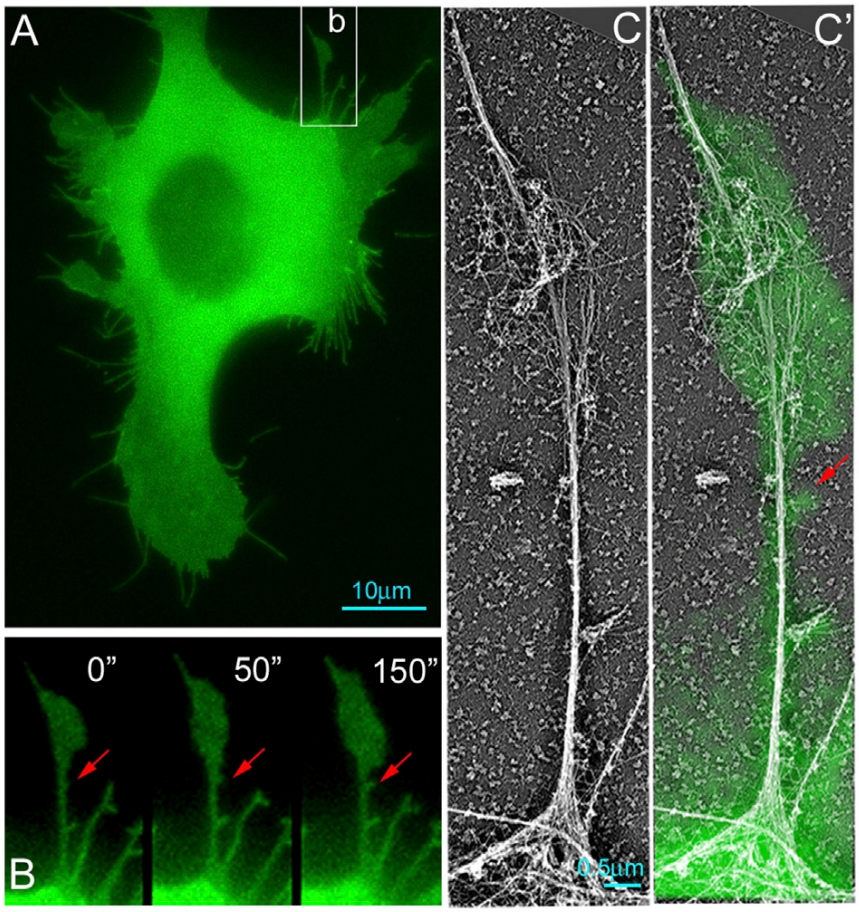

**Figure 2.8 Ultrastructures of Exo70-induced membrane protrusions**

**(A-C)** Correlative fluorescence and platinum replica EM showing the organization of actin in protrusive structures in a GFP-Exo70-expressing cell. **(A)** Overview of a B16F1 cell expressing GFP-Exo70. Scale bar, 10 μm. **(B)** Frames from the time-lapse sequence showing dynamics of a protruding filopodium (corresponding to **box b** in **A**). Correlative EM of region **B** is shown in **C** or with overlaid GFP-Exo70 fluorescence (green) **(C')**. The red arrows show a newly generated membrane protrusion that was devoid of actin.

were knocked down by RNAi. GFP-Exo70 induced numerous protrusions in these knockdown cells similar to the control cells, with approximately 20% of the protrusions actin-free (Figure 2.9A, see METHODS). The constitutively active form of Cdc42, Cdc42(Q61L), stimulated filopodia formation in B16F1 cells (Zuo et al., 2006; Figure 2.9B). Knockdown of Exo70 reduced the number of filopodia induced by Cdc42(Q61L), whereas knockdown of Sec8 or Sec15 had no effect, further suggesting that Exo70 is specifically required for filopodia induction.

In cells, higher percentage of endogenous Exo70 was localized to the plasma membrane relative to Exo84 and Sec10 (Figure 2.10A and B). By gel filtration, I found that the endogenous Exo70 exists in a free pool in addition to the holo-complex (Figure 2.10C). Taken together, it is likely that Exo70 induces membrane protrusions independent of the other exocyst components.

**Exo70-induced membrane deformation in simulations**

Molecular dynamics simulations were previously used to study the BAR domain-induced positive curvature and resolve at the molecular level the mechanisms, by which BAR domains sculpt the lipid bilayers (Humphrey et al., 1996; Arkhipov et al., 2008; Yin et al., 2009; Ayton and Voth, 2009). Recently, coarse-grained molecular dynamics (CGMD) simulations were employed to study the molecular interactions of ENTH domain oligomerization and association with membranes leading to the stabilization of tubular membrane geometries (Lai et al., 2012). We employed similar approaches to investigate the interaction between Exo70 and the membrane. We test whether the

**Figure 2.9**

**A.**

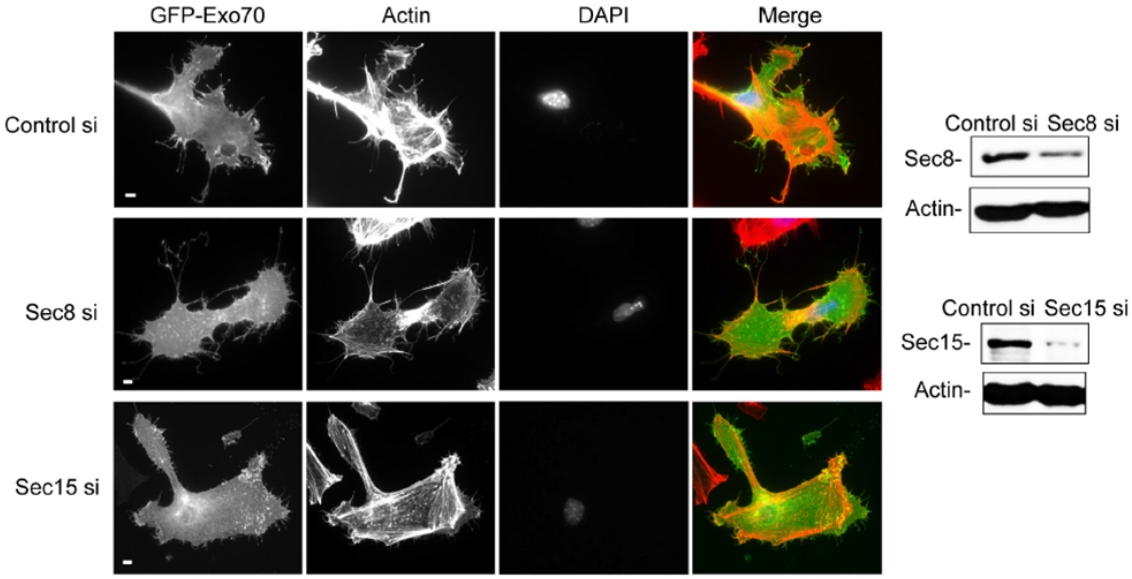
GFP-Exo70
Actin
DAPI
Merge
Control si
Sec8 si
Sec15 si
Control si Sec8 si
Sec8-
Actin-
Control si Sec15 si
Sec15-
Actin-

**B.**

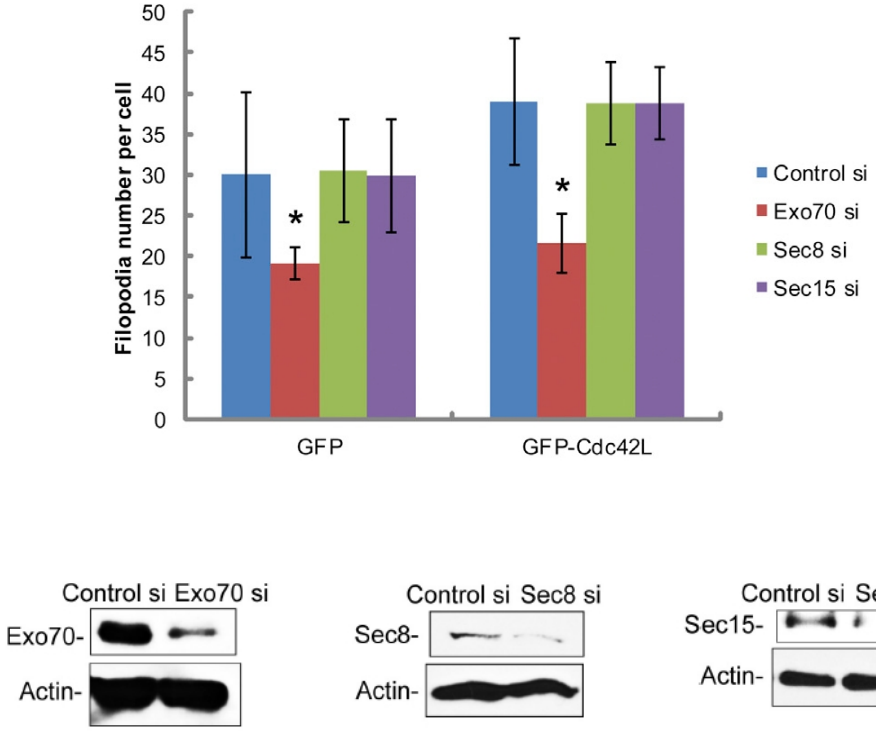
Filopodia number per cell
50
45
40
35
30
25
20
15
10
5
0
*
*
GFP
GFP-Cdc42L
Control si
Exo70 si
Sec8 si
Sec15 si
Control si Exo70 si
Exo70-
Actin-
Control si Sec8 si
Sec8-
Actin-
Control si Sec15 si
Sec15-
Actin-

**Figure 2.9 Exo70-induced filopodia are independent of other exocyst components**

**(A)** GFP-Exo70 induced actin protrusions are independent of other exocyst subunits. B16F1 cells expressing GFP-Exo70 and siRNA targeting Sec8 or Sec15 were stained for F-actin (red) and nuclei (blue). Scale bar, 5 μm. The efficiency of siRNA treatment was examined by Western blotting. GFP-Exo70 induced approximately 20% of actin-free protrusions when Sec8 or Sec15 was depleted, similar to the control cells. In each treatment, 10 cells were counted. The total filopodia numbers are 1159 for control siRNA, 1038 for Sec8 siRNA and 1134 for Sec15 siRNA. **(B)** B16F1 cells treated with siRNA targeting Exo70, Sec8 or Sec15 were transfected with GFP or GFP-Cdc42L. The expression of GFP-Cdc42L induced more filopodia comparing to GFP cells. The number of filopodia was significantly reduced upon Exo70 knockdown. Knockdown of Sec8 or Sec15 did not affect the filopodia formation in GFP-Cdc42L or GFP cells. Error bars, SD. n=10; *, $p<0.01$. The efficiencies of siRNA treatment in (B) were tested by Western blotting.

**Figure 2.10**

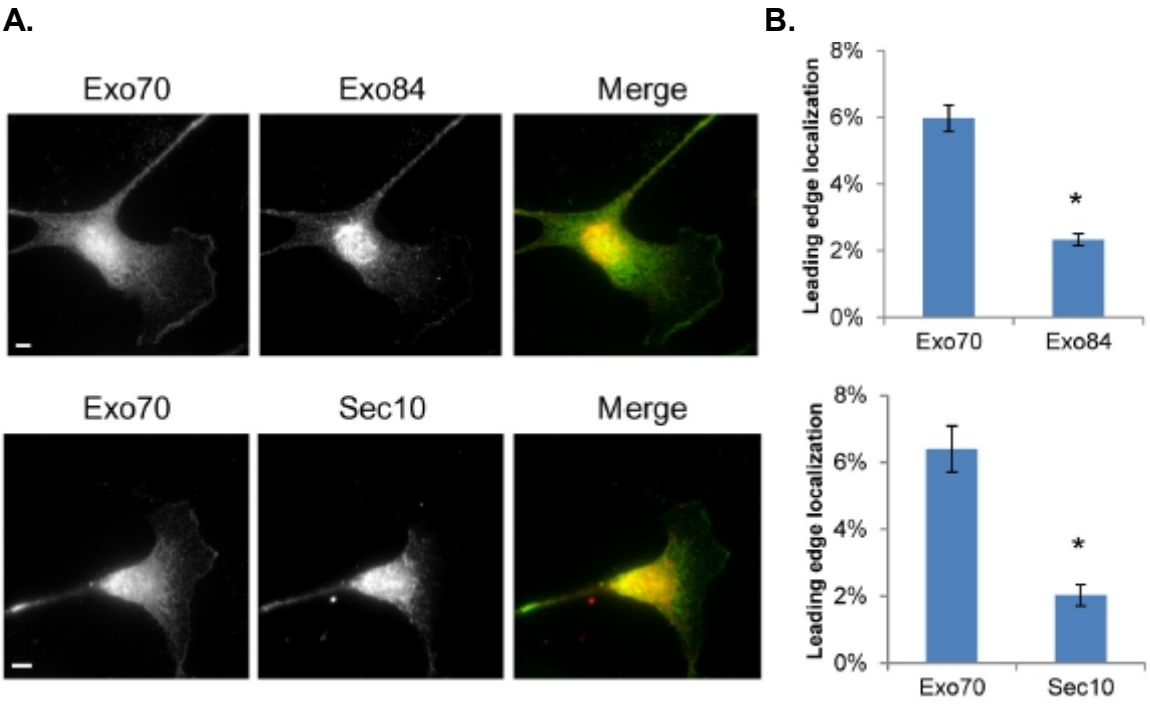
A.
Exo70
Exo84
Merge
Exo70
Sec10
Merge
B.
Leading edge localization
8%
6%
4%
2%
0%
Exo70
Exo84
*
Leading edge localization
8%
6%
4%
2%
0%
Exo70
Sec10
*

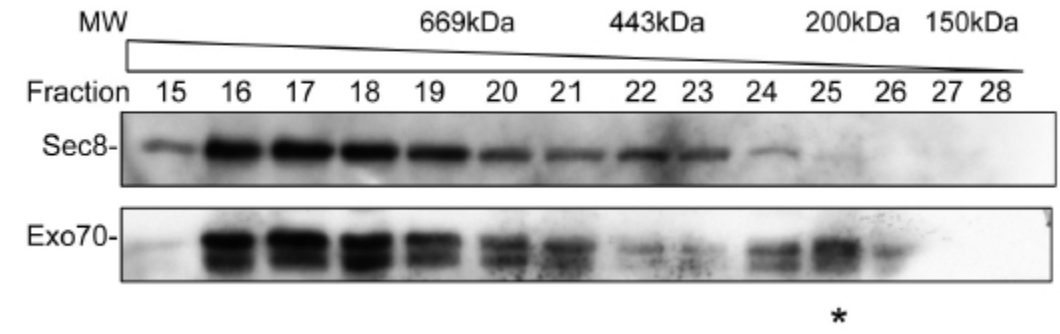
C.
MW
669kDa
443kDa
200kDa
150kDa
Fraction 15 16 17 18 19 20 21 22 23 24 25 26 27 28
Sec8-
Exo70-
*

**Figure 2.10 Exo70 exists in a free pool**

**(A)** B16F1 cells were co-immunostained with mouse monoclonal antibody against endogenous Exo70 (green) and rabbit polyclonal antibody against the exocyst subunit Exo84 (red, upper panel) or Sec10 (red, lower panel). The localization of Exo70 at the protruding plasma membrane was stronger than Exo84 or Sec10 in the same cell. Scale bars, 5 μm. **(B)** Quantification of the localization of different exocyst subunits at the protruding plasma membrane. The fluorescence intensities at the protruding plasma membrane and the whole cell were measured using ImageJ. Shown are the percentages of the leading edge intensities. Error bars, s.e.m; n=10; *, $p<0.01$. **(C)** Gel filtration of MDA-MB-231 cell lysates using a Superdex 200 10/300GL column in a buffer containing 20 mM HEPES, pH 7.4, 1 % NP-40, 100 mM KCl, 5 mM $MgCl_2$, 1 mM NaF, 1 mM DTT, 1mM PMSF. Fractions were collected and separated by SDS-PAGE and blotted for Sec8 and Exo70. Exo70 existed in a free pool (as indicated by "*", fraction 24-26) as well as the holo-complex that co-migrated with Sec8.

minimal oligomerized state (namely a dimer) shows enhanced curvature induction in comparison to the monomer. If the enhancement is present at the dimer level, this effect is expected to be accentuated further in the case of higher-order oligomers. The crystal structure of mouse Exo70 (amino acid 85–653) features a 170 x 35 Å rod composed of α-helical bundles slightly curved in the middle (Hamburger et al., 2006; Moore et al., 2007); and the N-terminal, non-crystalized region is predicted to be a coiled-coil structure. Based on the structural information, coarse-grained Exo70 anti-parallel and parallel dimer models were constructed using MODELLER and relaxed using all-atom molecular dynamics simulations, and then attached to an equilibrated bilayer containing 12,800 lipids with a 4:1 DOPC:DOPS ratio (Figure 2.11A). The system was simulated with a standard MARTINI model with time step of 40 fs up to 300 ns in real-time. In addition, we simulated Exo70(Δ1-75) monomer, Exo70(K571A/E572A) mutant dimers and no protein control in the system. We have characterized the induced curvature as well as the fluctuations associated with the curvature according to a statistical procedure (see METHODS), in which we fit frame-by-frame a two-dimensional Gaussian function to the height of the bilayer mid-plane. These fits characterize the dynamic negative-curvature and anisotropy associated with dimples induced by Exo70 on the bilayer in each conformation; the anisotropy is particularly pronounced in the wild-type dimers. We computed the average maximum induced curvature for each system, the extent of the curvature field (and the associated anisotropy by defining the standard deviation of the Gaussian fit to the mid-plane deformation along the major and minor axes), as well as the estimate of the deformation energy to create the equivalent membrane deformation

**Figure 2.11**

**A.**

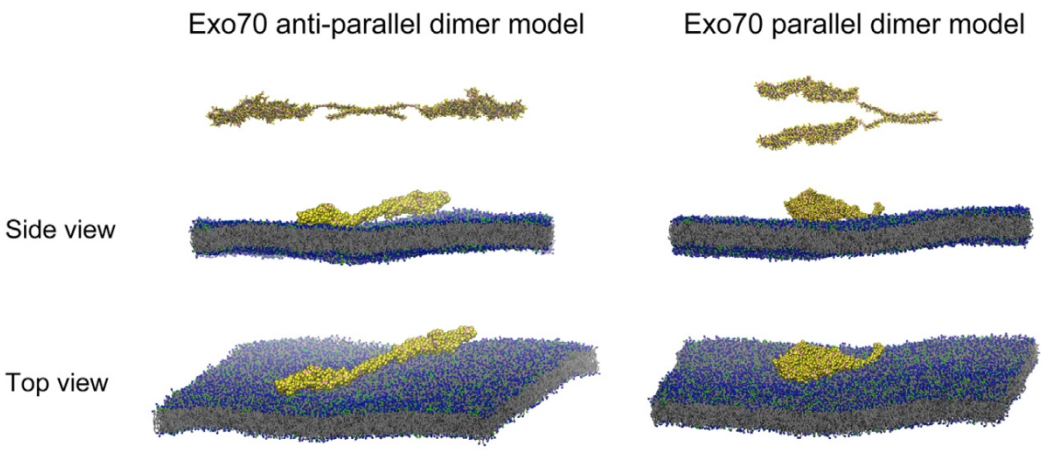


**B.**

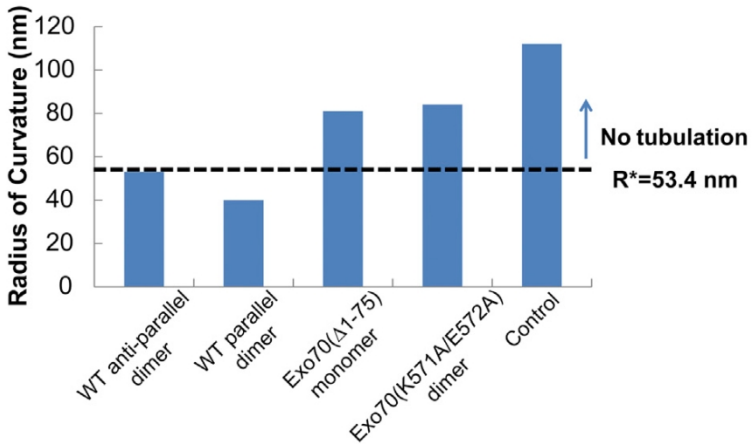


**C.**

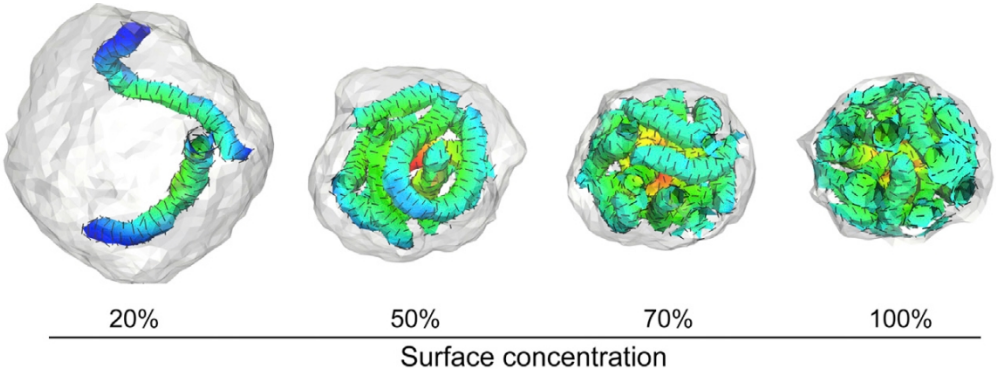

**Figure 2.11. Molecular dynamics and mesoscale simulations demonstrate that Exo70 induces negative membrane curvature.**

**(A)** Molecular dynamics simulation of modeled Exo70 anti-parallel (left) and parallel (right) dimers on a DOPC/DOPS bilayer. Top and side views of the simulation snapshots show negative curvature formed in both directions. All snapshots were rendered with VMD (Humphrey et al., 1996). **(B)** Comparison of the radius of curvature estimates (here $R = \langle 2H_{\max} \rangle^{-1}$) for different Exo70 variants on the membrane. Dashed line at 53.4 nm represents the threshold above which no inward membrane tubulation was detected in mesoscale simulations. **(C)** Snapshots from mesoscale simulations of inward growing tubules for model Exo70 domains at different surface concentration (from 20% to 100%); $a_0$=14 nm, $H_0^{\parallel}$=-1.0/$a_0$ and $\varepsilon_{LL}$=1$k_B$T. The extent of tubulation is Exo70 concentration-dependent. Exo70 proteins on the outer surface of the membrane are not shown in order to enhance the visibility of the tubules. See also Figure 2.12.

induced by the protein (Figure 2.12A-C and METHODS). These estimates for a single unit (*i.e.* protein monomer or protein dimer) interacting with a patch of a bilayer indicate that both anti-parallel and parallel dimers induce significantly more negative curvature than Exo70(Δ1-75) monomer, Exo70(K571A/E572A) mutant dimer, and control simulations of a bare membrane. The results are presented in Figure 2.11B in terms of R, the radius of curvature estimates (here $R = \langle 2H_{\max} \rangle^{-1}$). Analysis of the protein and lipid conformations in our simulations revealed that the induction of the curvature was mediated by the positively charged residues throughout the surface of the Exo70 dimers that interact with the negatively charged phospholipids, which suggests that curvature induction requires a scaffold of at least two linked Exo70 monomers that act in concert to remodel the associated lipid bilayer from its native planar state; a representation of the electrostatic map depicting this charge complementarity between the protein and the lipid interfaces is shown in Figure 2.12D-E.

Mesoscale simulations have been carried out in the field to investigate endocytic vesicle formation in yeast and mammalian cells, which provide important mechanistic insights of protein-lipid interplays during endocytosis (Liu et al., 2006; Liu et al., 2009b; Agrawal et al., 2010). More recently, an extension of this approach along with concepts from the theory of self-assembly in liquid crystalline phases has been employed to study the nucleation of tubular morphologies (Ramakrishnan et al., 2010). Using this new approach, we performed Monte Carlo simulations starting from a closed vesicle with Exo70 dimers (Figure 2.11C). The equations and parameter settings are explained in detail in METHODS. We have examined the collective effect of negative curvature-

## Figure 2.12

**A.**

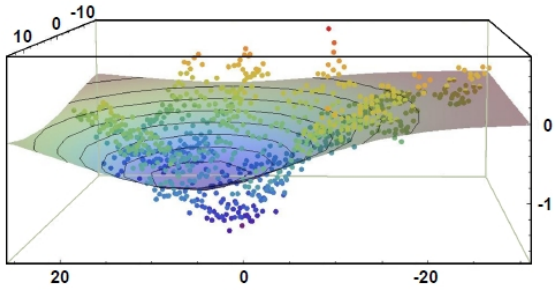


$$z(x,y) = A_0 \exp\left\{\frac{(x-x_0)^2}{2\sigma_x^2}\right\}\exp\left\{\frac{(y-y_0)^2}{2\sigma_y^2}\right\}$$

(CGMD-eq-1)

**B.**

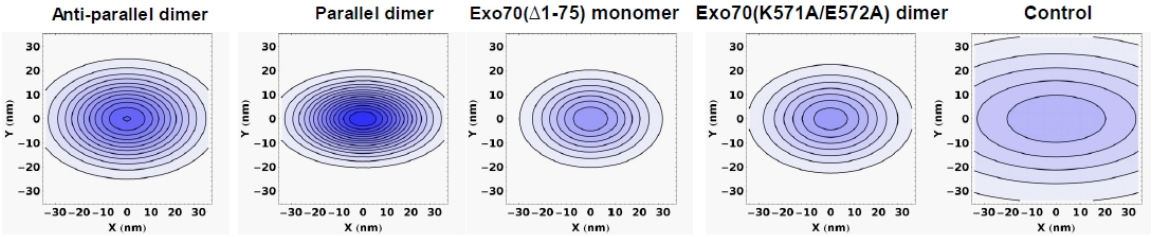


**C.**

| System | $\langle H_{max} \rangle$ ($nm^{-1}$) | $\langle \sigma_x \rangle$ (nm) | $\langle \sigma_y \rangle$ (nm) | Radius (nm) | $\langle E \rangle = \iint \langle H \rangle^2 dxdy$ |
|---|---|---|---|---|---|
| Anti-parallel dimer | $-9.4 \times 10^{-3}$ | 11.2 | 17.4 | 53 | 0.0537 |
| Parallel dimer | $-12.4 \times 10^{-3}$ | 8.6 | 16.1 | 40 | 0.0667 |
| Exo70(Δ1-75) monomer | $-6.2 \times 10^{-3}$ | 9.9 | 14.6 | 81 | 0.0174 |
| Exo70(K571A/ E572A) dimer | $-5.9 \times 10^{-3}$ | 11.1 | 17.2 | 84 | 0.0208 |
| Control | $-4.4 \times 10^{-3}$ | 18.6 | 38.9 | 112 | N/A |

**E.**

| Position | Residue | Position | Residue |
|---|---|---|---|
| 404 | ASP | 407 | LYS |
| 408 | GLU | 336 | ARG |
| 329 | GLU | 330 | ASN |
| 343 | ASP | 484 | VAL |
| 501 | LYS | 502 | GLU |

**D.**

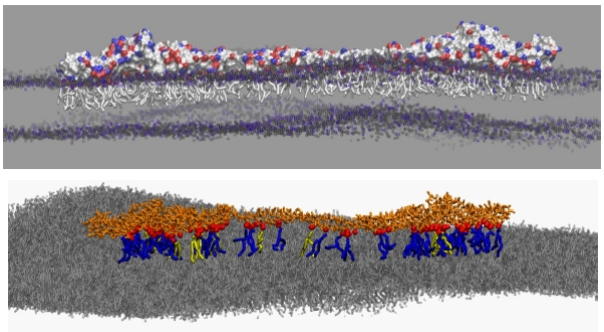

**F.**

| System | n (α = -0.6) | n (α = -1.0) | n* |
|---|---|---|---|
| Anti-parallel dimer | 1.22 | 3.40 | 1.23 |
| Parallel dimer | 0.99 | 2.74 | 1.47 |
| Exo70(Δ1-75) monomer | 3.78 | 10.49 | 1.96 |
| Exo70(K571A/ E572A) dimer | 3.17 | 8.80 | 1.23 |

**Figure 2.12. Quantification of membrane deformation from molecular dynamics simulations.**

**(A)** An example of the fitted two-dimensional Gaussian function (CGMD-eq-1) for a single frame from the antiparallel dimer simulation, pictured with contours. The protein is aligned horizontally, and mid-plane heights are depicted as points, colored by height. The fit shows significant negative curvature. (**B**) Visualization of the integrand of deformation energy. (**C**) Summary of induced curvature fields measured and computed from CGMD simulations. (**D**) An electrostatic map demonstrates the positive (blue) and negative (red) residues on the surface of Exo70. The membrane-contacting face of the protein interacts with both negatively-charged (DOPS, shown in yellow) and zwitterionic (DOPC, shown in blue) lipids in the bilayer. The figure shows all lipids bound within 12Å. (**E**) List of membrane-contacting residues that make persistent contacts with lipids. (**F**) Predicted number of proteins ("n") required to induce tubular membranes for $\alpha$=-0.6 and $\alpha$=-1.0 for the various Exo70 systems.

inducing fields on membrane morphology. In our model, the membrane surface is triangulated and each vertex can have up to one field vector of strength $H_0^{\parallel}$; we note that each field vector on a vertex can represent the collective effect of multiple (but a fixed number of) proteins acting on the membrane area associated with that vertex. The average length of a link between two adjacent vertices is $1.3a_0$, where $a_0$ is the intrinsic length of the triangulated membrane lattice. We set the value of $a_0$ to be 14 nm by requiring the span of the field vector ($1.3a_0$) in the mesoscale model to be consistent with the extent of the long-axis of the curvature field in the CGMD model for the protein (see $\sigma_y$ values in Figure 2.12C), *i.e.* $1.3a_0=\sigma_y$. We explore surface concentrations of the field vector (*i.e.* percentage of vertices at which a curvature field vector resides) in the range 20% to 100% and field vector strength in the range $H_0^{\parallel} = -0.4/a_0$ to $-1.0/a_0$ to find parameter regimes which stabilize inward tubulation. Figure 2.11C depicts typical membrane morphologies when $H_0^{\parallel} = -1.0/a_0$ and surface concentration of curvature fields from 20% to 100%. At 50% and 70% surface concentration, the resulting tubular morphologies are remarkably similar to the experimentally observed morphologies depicted in the electron micrograph of Figure 2.1. The extent of tubulation depends on Exo70 concentration: inward tubules were observed to form at low field vector surface concentration (20%); as the concentration increased, the number of tubules increased. Our simulations also indicated that below a field vector strength of $|H_0^{\parallel}| < |-0.6/a_0|$, the inward membrane tubulation was absent. Based on the tubular morphology in our simulation, we performed geometric analyses of individual tubules to find that the average tubule diameter was $2.6a_0$=36 nm at $H_0^{\parallel} = -1.0/a_0$ and $3.4a_0$=48 nm for $H_0^{\parallel} =$-

$0.6/a_0$. The threshold protein density required to induce tubular invaginations is shown in Figure 2.12F; see also METHODS for the estimation of the threshold.

All together, the simulations suggest that Exo70 generates pronounced negative membrane curvature even at the dimer-level. Estimates of the surface density of proteins required for stabilization of inward tubulation reveals that only the wild type dimers are able to induce sufficient curvature to meet the estimated threshold and the monomer as well as the lipid binding mutant fails to meet the threshold criteria.

## 2.3 DISCUSSION

Combining biochemical and cell biological approaches and *in silico* mathematical simulations, my study reveals a novel function of Exo70 in the generation of negative membrane curvature *in vitro*. In cells, overexpression of Exo70 induces filopodial protrusions, many of which are actin-free at the tips, supporting the role of Exo70 in membrane deforming. Furthermore, cells with inhibition of Exo70, or expressing Exo70 mutants deficient in curvature induction, are defective in generating filopodial protrusions,.

Phospholipid-binding and protein oligomerization-mediated scaffolding is one of the major mechanisms for membrane curvature induction (McMahon and Gallop, 2005; Frost et al., 2009; Mim et al., 2012; Boucrot et al, 2012). By sequence alignment, Exo70 does not belong to any of the BAR domain families. On the other hand, the rod-like structure of Exo70 and its oligomerization may bestow its overall resemblance

functionally to the BAR proteins. Through the characterization of Exo70 mutants, I demonstrate that both phospholipid-binding and oligomerization are needed for Exo70 to induce membrane curvature.

In this study, I find that overexpression of Exo70 can induce actin-free filopodial protrusions, further supporting the role of Exo70 in membrane curvature induction in cells. Similar phenotypes have been observed with the overexpression of I-BAR domains (Suetsugu et al., 2006; Yang et al., 2009) and srGAP2 F-BAR (Guerrier et al., 2009) that are capable of inducing negative membrane curvatures. The "actin-free" filopodial protrusions observed in these studies are consistent with the emerging view that membrane curvature induction plays a role in protrusion formation (Scita et al., 2008; Mattila and Lappalainen, 2008). The actin networks in lamellipodia during cell migration are mostly branched filaments generated by the Arp2/3 complex (Pollard and Borisy, 2003), whereas those in filopodia are bundled filaments generated by formins (Mattila and Lappalainen, 2008). Exo70 was shown to directly interact with and kinetically stimulate the Arp2/3-complex-mediated actin polymerization and branching (Zuo et al., 2006; Liu et al., 2012). Unlike in lamellipodia, the Arp2/3 complex in the distal tips of filopodia is less prevailing (Svitkina et al., 1999). As such, in filopodia, Exo70 cannot effectively exert its stimulatory effect on actin branch formation as it does in lamellipodia (Liu et al., 2012). The filopodial tips devoid of actin in the Exo70-overexpressing cells may reflect that the membrane-deforming activity of Exo70 surpasses its ability to stimulate actin in those regions.

The function of Exo70 in membrane deformation may be independent of the exocyst complex. None of the other exocyst subunits can induce membrane protrusions in cells upon overexpression. Exo70 is able to induce protrusions even when other exocyst subunits are knocked down. Inhibition of Exo70, but not any other exocyst components, affects membrane protrusion formation in cells with or without Cdc42 induction. Exo70 has a clear enrichment in the plasma membrane comparing to other subunits. Furthermore, the endogenous Exo70 exists in free pools as well as being part of the exocyst holo-complex; similar observation has recently been made in yeast cells (Morgera et al., 2012). It is likely that the free pool of Exo70 exerts its function in membrane curvature induction during protrusion formation.

Phospholipid-binding and protein oligomerization-mediated scaffolding is one of the major mechanisms for membrane curvature induction (McMahon and Gallop, 2005; Frost et al., 2009; Mim et al., 2012; Boucrot et al, 2012). By sequence alignment, Exo70 does not belong to any of the BAR domain families. On the other hand, the rod-like structure of Exo70 and its oligomerization may bestow its overall resemblance to the BAR proteins. Through the characterization of Exo70 mutants, we demonstrate that both phospholipid-binding and oligomerization are needed for Exo70 to induce membrane curvature. In addition to the biochemistry and cell biology experiments, we investigate the molecular mechanism of Exo70-induced membrane deformation by molecular dynamics simulations. Based on the known Exo70 sequence and its crystal structure, our analysis of the protein-membrane interactions predicts the ability of dimeric Exo70 to induce *negative* curvature through positively charged residues on its surface that interact

with phospholipids. Moreover, mesoscale Monte Carlo simulations demonstrate that Exo70 generates membrane tubules on liposomes with remarkable similarities to the EM micrographs obtained from our *in vitro* membrane tubulation assay. The simulations of protein-membrane interactions at the atomic scale and membrane tubulation at the mesoscale further suggest an oligomerization-mediated mechanism for Exo70-induced membrane curvature induction.

In summary, my study reveals that Exo70, through an oligomerization-based scaffolding mechanism, generates negative curvature on the plasma membrane. Exo70 and other members of the exocyst have been shown to function in such cellular processes as cell migration, primary ciliogenesis, viral progression, neurite outgrowth and branching, all of which involve plasma membrane remodeling. It will be interesting to test whether the function of Exo70 in membrane deformation reported here applies to these processes. Moreover, as Exo70 is regulated by small GTPases (TC10, Inoue et al., 2003) and kinases (ERK1/2, Ren and Guo, 2012), it will be interesting to investigate how the function of Exo70 is spatially and temporally controlled in various cellular contexts to fulfill different physiological functions.

## 2.4 MATERIALS AND METHODS

### Plasmids and antibodies

Full-length rat Exo70 and Exo70(Δ1–75) were cloned in-frame into pEGFP-C1 vector or p3xFLAG-CMV-14 vector for expression in cells. Full-length rat Exo70 was cloned in-

frame into pJ3-RFP-Ruby for expression in cells. The Exo70 mutant Exo70(K571A/E572A) were generated using the QuikChange site-directed mutagenesis kit (Stratagene). Different Exo70 variants were also cloned in-frame into pGEX-KG (a modified form of pGEX-2T) or pGEX-6P-1 (GE Healthcare/ Amersham Biosciences) for bacterial expression. Mouse MIM-I-BAR (a.a.1-250) in vector pTYB12 was provided by Dr. Roberto Dominguez (University of Pennsylvania). Monoclonal antibodies against Sec8, Sec15, Exo70 were obtained from Dr. Shu-Chan Hsu (Rutgers University). Polyclonal antibody against Exo84 was obtained from Dr. Charles Yeaman (University of Iowa). Mouse anti-actin mAb (MAB 1501, clone C4) was purchased from Chemicon, Millipore, monoclonal antibody against GFP (MMS-118R, clone B34) from Covance, and monoclonal antibody against FLAG (F3165, clone M2) from Sigma.

**Protein purification**

GST fusion proteins were expressed in *E. coli* strain BL21-CodonPlus(DE3)-RP and purified using glutathione Sepharose 4B (GE Healthcare). GST-tagged Exo70 fusion proteins were cleaved with GST-PreScission protease to remove GST in 50 mM Tris-HCl, 150mM NaCl, 1mM EDTA, 1mM dithiothreitol (pH 7.0) overnight at 4°C; the resins were then washed with PBS containing 1mM DTT to elute the liberated recombinant proteins. MIM-I-BAR was purified as previously described (Lee et al., 2007). Briefly, chitin tagged MIM-I-BAR was incubated with chitin beads (New England Biolabs) in 20 mM Tris (pH 7.5), 500 mM NaCl, 1 mM EDTA, 100 μM PMSF. MIM-BAR was eluted

from the beads following DTT-induced self-cleavage of the intein and dialyzed into the desired buffers.

**Cell culture and transfection**

B16F1 mouse melanoma cells were maintained in DMEM/F12 (Invitrogen) supplemented with 10% FBS (Yang et al., 2007). DNA transfections into B16F1 cells were performed using Lipofectamine™ LTX with Plus™ Reagent (Invitrogen). For RNA interference (RNAi), cells were grown to 50% confluence and transfected with small interfering RNA (siRNA) duplexes using Lipofectamine 2000. The human Exo70 siRNA target sequence used in the experiments is 5'-GGTTAAAGGTGACTGATTA-3'. The control Luciferase GL2 siRNA target sequence is 5'-AACGTACGCGGAATACTTCGA-3'. The mouse Sec8 siRNA target sequence used is 5'-GTCCTGATGACAACTTAATTT-3'. The mouse Sec15 siRNA target sequences are 5'-AAAGATATCATTCGATGTAGA-3' and 5'-AACAAGTGACGGATACTAATA-3'. The efficiency of the knockdown was determined by Western blotting.

**LUV preparation and thin-section electron microscopy**

$PI(4,5)P_2$ (L-α-phosphatidylinositol-4,5-bisphosphate; porcine brain triammonium salt) and DOPC (1,2-dioleoyl-*sn*-glycero-3-phosphocholine) were purchased from Avanti Polar Lipids. LUVs were prepared using a protocol adapted from Mattila et al, 2007. $PI(4,5)P_2$ and DOPC were mixed at a molar ratio of 30:70, or $PI(4,5)P_2$: DOPS: DOPE: DOPC were mixed at a molar ratio of 5:15:10:70, dried with nitrogen stream, and

hydrated in 20 mM Hepes-KOH, pH 7.5, and 100 mM NaCl to a total lipid concentration of 0.5mM. The mixed lipids were subjected to five cycles of freeze-thaw and extrusion through 1 μm filters using a mini-extruder. The concentrations of LUVs and proteins were chosen based on previous studies (Peter et al., 2004; Liu, et al., 2007; Mattila et al., 2007). 100 μM LUVs were incubated with 2 μM recombinant proteins at room temperature for 1 hour, fixed with 2% glutaraldehyde and 0.1% tannic acid in 0.1M Na-cacodylate buffer for 1hour at 4°C. Samples were then sedimented (17,000 g, 30 min at 4°C) and post-fixed in 1% $OsO_4$ for 1 hour at 4°C, followed by *en bloc* staining with 2% uranyl acetate for 1 hour at 4°C, dehydration and Spurr embedding. 100 nm sections were prepared and stained with uranyl acetate and lead citrate. All samples were visualized using a JEM 1011 transmission electron microscope (JEOL USA) operated at 100 kV. For tilt series, specimen was tilted ±20º at 5º intervals. Images were captured by ORIUS 835.10W CCD camera (Gatan). The diameters of the membrane tubules inside the LUVs were measured by ImageJ. For 3-D reconstruction, images were aligned and reconstituted with TomoJ plugin in ImageJ.

**GUV preparation and confocal microscopy**

POPC (1-palmitoyl-2-oleoyl-*sn*-glycero-3-phosphocholine), DOPS (1-palmitoyl-2-oleoyl-*sn*-glycero-3-phospho-L-serine, sodium salt) and DSPE-Bio-PEG2000 (1,2-distearoyl-*sn*-glycero-3-phosphoethanolamine-N-[biotinyl(polyethyleneglycol)-200], ammonium salt) were purchased from Avanti Polar Lipids and Texas Red-DHPE (Texas Red-1,2-dihexadecanoyl-*sn*-glycero-3-phosphoethanolamine) from Invitrogen. GUVs

were prepared from a lipid mixture containing POPC, POPS, PI(4,5)$P_2$, Texas Red-DHPE and DSPE-Bio-PEG2000 (molar ratio 80:15:5:0.3:0.3) by electroformation (Angelova et al., 1986; Mathivet et al., 1996), as described (Tian and Baumgart, 2009), except that the sucrose concentration was 350 mM to osmotically balance the solutions.

GUVs were introduced into protein solutions within polypropylene tubes at room temperature at a final protein concentration of 5 μM. Aliquots were transferred between glass coverslips separated by Parafilm. GUV images were collected using a confocal fluorescence microscope (Tian and Baumgart, 2009), with 543 nm laser excitation of Texas Red-DHPE. The contours of the GUVs were transformed to a co-ordinate system using the Polar Transformation plugin in ImageJ.

**Gel filtration**

200 μl (600 μg) recombinant Exo70 or Exo70(Δ1-75) were loaded onto a Superdex 200 10/300GL column and eluted with PBS containing 1mM DTT at a flow rate of 0.5 ml/min. 500 μl fractions were collected. 20 μl of each fraction was subjected to 8% SDS-PAGE and stained with SimplyBlue SafeStain (Invitrogen). The column was calibrated using molecular weight markers (MW-GF-1000, Sigma). For cross-linking, fractions were treated with 40nM BM$(PEG)_2$ (Thermo Scientific) for 1 hour at room temperature prior to SDS-PGAE. Exo70 has 4 cysteines and BM$(PEG)_2$ has a spacer arm of 14.7Å.

Gel filtration of MDA-MB-231 cell lysates was performed using a Superdex 200 10/300GL column in a buffer containing 20 mM HEPES, pH 7.4, 1 % NP-40, 100 mM

KCl, 5 mM $MgCl_2$, 1 mM NaF, 1 mM DTT, 1mM PMSF. Fractions were collected and analyzed by Western blotting.

**Immunoprecipitation assay**

HEK293T cells co-expressing Exo70-FLAG and the following constructs: GFP-Exo70, GFP-Exo70(Δ1-75) or GFP vector were lysed in a buffer containing 50 mM Tris-HCl (pH 8.0), 135 mM NaCl, 1mM EDTA, 1 mM $Va_3VO_4$, 0.5% Triton X-100 and protease inhibitors. Cell lysates were incubated overnight with anti-Flag (M2) agarose (Sigma) at 4°C. The inputs and bound proteins were analyzed by Western blotting using an anti-GFP monoclonal antibody. The same membrane was stripped with Restore Western Blot Stripping Buffer (Thermo Scientific) and blotted with FLAG monoclonal antibody.

**LUV co-sedimentation assay**

Sucrose-loaded LUVs were prepared by size extrusion. Various lipids were mixed at different molar ratios, dried with nitrogen stream, and suspended at a concentration of 2 mM in a buffer containing 12 mM HEPES, pH 7.0, and 176 mM sucrose. The mixed lipids were subjected to five cycles of freeze-thaw and a 1-min bath sonication before being passed through 100-nm filters using a mini-extruder. LUVs were dialyzed overnight in the buffer containing 20mM HEPES, pH 7.5, 150 mM NaCl, 1mM EGTA.150 nM Exo70 or Exo70Δ(1-75) were mixed with 5% $PI(4,5)P_2$+95% DOPC or 100% DOPC LUVs at indicated concentration and centrifuged at 62,000 rpm for 30 min

at 25°C in a TLA-100 rotor. The supernatants and pellets were subjected to 10% SDS-PAGE for quantification of bound and unbound materials.

**Live cell imaging**

B16F1 cells were co-transfected with GFP-Exo70 and mCherry-Lifeact. The cells were re-plated the next day, and transferred into phenol red–free L-15 medium supplemented with 10% FBS and kept on the microscope stage at 37ºC during observation. Light microscopy was performed using an Eclipse TE2000-U inverted microscope (Nikon) equipped with Planapo 100x 1.3 NA objective and Cascade 512B CCD camera (Photometrics) driven by Metamorph imaging software (Molecular Devices). For quantification purposes, filopodia with F-actin-free tips were defined as filopodia lacking detectable mCherry-Lifeact fluorescence signal within a distance of 0.6μm or more from the tip of the GFP-Exo70 signal in the same filopodium.

**Electron microscopy of B16F1 cells**

Cells for platinum replica EM were processed as described previously (Svitkina and Borisy, 2006; Svitkina, 2007). Briefly, cells were extracted for 5 min at room temperature with 1% Triton X-100 in PEM buffer containing 2 μM phalloidin with or without 2% PEG (MW 35,000), followed by fixation with 2% glutaraldehyde in 0.1 M Na-cacodylate (pH 7.3).

Correlative EM was performed as described using cells growing on marked coverslips (Svitkina and Borisy, 2006; Svitkina, 2007). Samples were analyzed using a JEM 1011

transmission electron microscope (JEOL USA) operated at 100 kV. Images were captured by an ORIUS 835.10W CCD camera (Gatan) and presented in inverted contrast.

**Fluorescence microscopy**

To quantify the number of filopodia, B16F1 cells with different treatments were stained with Alexa Fluor 594 phalloidin (Invitrogen/Molecular Probes). To quantify the localization of different exocyst subunits at the protruding plasma membrane, B16F1 cells were co-stained with anti-Exo70 monolocal antibody and anti-Exo84 or Sec10 polyclonal antibody. The fluorescence intensities at the protruding plasma membrane and the whole cell were measured using ImageJ.

**Molecular dynamics (MD) simulations**

A coarse-grained Exo70 model was constructed according to the crystal structure in the protein data bank (pdb code 2PFT) (Moore et al., 2007). Structures for the unresolved loops and alpha-helical N-terminus were constructed with MODELLER (Sali and Blundell, 1993). The resulting structure was relaxed using a short, 10 ns all-atom simulation under the CHARMM27 force field in the GROMACS molecular dynamics simulation package (Bjelkmar et al., 2010). A representative snapshot was then coarse-grained for use in the MARTINI force field (Monticelli et al., 2008). To maintain secondary structure, elastic bonds were applied to all backbone beads within 0.5 – 0.9 nm with a force of 500 kJ/mol-nm$^2$, except for the N-terminal tail, for which we used a much

weaker 5 kJ/mol-nm$^2$ force constant for residues 1-20 and 50 kJ/mol-nm$^2$ for residues 21-90.

Wild type Exo70 was modeled in a parallel or anti-parallel dimer conformation while the Exo70(K571A/E572A) mutant was modeled in an anti-parallel conformation and compared to the corresponding wild type control. Exo70(Δ1-75) model was effectively a monomer as the dimerization domain is considerably shortened. Each modeled Exo70 variant was attached to an equilibrated bilayer containing 12,800 lipids with a 4:1 DOPC:DOPS ratio. The charge (–1) on DOPS partly serves as a surrogate for the higher charge (–4) on $PIP_2$ at a lower concentration. The systems were minimized and simulated with a standard MARTINI time step of 40 fs for 100 ns. Due to the smoothed energy landscape in the MARTINI force field, this corresponds to a real time of 3-4 times longer. The Berendsen thermostat and barostat maintained a temperature of 310K and semi-isotropic pressure coupling of 1.0 bar both parallel and perpendicular to the bilayer plane with coupling time constants of 1.0 and 0.2 ps, respectively. Simulations were solvated with 600,000 water beads, corresponding to 4 water molecules each, and counter-ions were added at a physiological concentration of 150 mM. All other parameters were set per the MARTINI force field specifications (Monticelli et al., 2008). All simulations were performed on supercomputing platforms at the Texas Advanced Computing Center (TACC). The coarse-grained MD (CGMD) simulations of the protein-membrane system were run on parallel architectures with 48-46 processors.

**Characterization of curvature in CGMD simulations**

To characterize the induced curvature from these CGMD simulations, we have modeled the height of the mid-plane of the bilayer as a two-dimensional anisotropic Gaussian function centered and oriented with respect to the location of the protein (see below). This method provides a general description of the induced curvature by separately measuring the position, extent, degree of anisotropy, magnitude of curvature of the associated lipids and fluctuations due to dynamics/membrane undulations.

Since Exo70 dynamically remodels the associated bilayer, it was necessary to analyze the average as well as the fluctuations about the average in bilayer curvature to deconvolute the curvature effect from the undulation modes of the bilayer. Specifically, we must distinguish between negative curvature induction and the random fluctuations in the height of the bilayer. To this end, we first constructed a surface corresponding to the mid-plane of the bilayer and aligned the protein along its principal axis in each frame of the simulation. Then, for each frame, we divided the bilayer mid-plane surface into 5×5 nm patches and considered the patches that were within 10 nm of any atom of the protein. Analysis of a control membrane with no associated protein indicates that this filter effectively removes local undulations, which add noise to our estimate of curvature without changing the overall result. That is, the measured curvature of our control simulation is effectively infinite. The heights of these relevant mid-plane patches were then fit to a two-dimensional Gaussian function given by,

$$z(x,y) = A_0 \exp\left\{\frac{(x-x_0)^2}{2\sigma_x^2}\right\} \exp\left\{\frac{(y-y_0)^2}{2\sigma_y^2}\right\}. \qquad \text{(CGMD-eq-1)}$$

Here, x and y are orthogonal axes chosen with respect to the alignment of the protein. The quantities $\sigma_x$ and $\sigma_y$ are the standard deviations in orthogonal directions, each corresponding to the "width" or extent of curvature of the fitted Gaussian parallel and perpendicular to the aligned axis of the protein. The maximum curvature is induced at the position $(x_0, y_0)$ where the height is $A_0$ higher than the average. This position is not necessarily at the center of the protein. Note that this fitting procedure is a conservative estimate of the negative curvature because it always predicts a curvature smaller than the actual curvature observed in the simulations.

We calculate the strength of the induced curvature according to the following expression for mean curvature,

$$H = \frac{(1+z_x^2)z_{yy}+(1+z_y^2)\,z_{xx} - 2z_x\,z_y\,z_{xy}}{(1+z_x^2+z_y^2)^{\frac{3}{2}}}. \text{(CGMD-eq-2)}$$

Here, $z_{xy}$ terms correspond to the partial derivatives of the height of the fitted function. Thus, for each frame we have obtained a maximum mean curvature, i.e. $H(x_0,y_0)$ from equation CGMD-eq-1, and values $\sigma_x$ and $\sigma_y$ which characterize the parallel and perpendicular extent of curvature, Figure 2.12A-C.

In order to esimate the average deformation induced by the protein on the membrane, we compute the average deformation energy ⟨E⟩ (in units of κ) using the expression:

$$\langle E\rangle = \int_0^{\sigma_x} dx \int_0^{\sigma_y} dy \left[\langle H_{max}\rangle \exp\left\{\frac{(x-x_0)^2}{2\langle\sigma_x^2\rangle}\right\} \exp\left\{\frac{(y-y_0)^2}{2\langle\sigma_y^2\rangle}\right\}\right]^2. \qquad \text{(CGMD-eq-3)}$$

Here $\langle E \rangle$ represents the ensemble average over all the frames of the CGMD simulation; the average quantities and the integrand are summarized in Figure 2.12B-C. These quantities are input into a mesoscale model (described below) in order to predict their effect on vesicle morphology.

**Mesoscale Model**

The physical properties of a biological membrane can be understood using a phenomenological model, the well-known being the Helfrich Hamiltonian given by,

$$\mathcal{H}_{\mathrm{el}} = \int dA \left\{ \frac{\kappa}{2} (H - H_0)^2 + 2\kappa' K + \sigma \right\}. \qquad (Mesoscale - 1)$$

Here, the membrane is approximated to a two dimensional fluid, elastic sheet, with lateral dimensions large enough to neglect its thickness. The phenomenological parameters, $\kappa$, $\kappa'$ and $\sigma$ are the bending rigidity, Gaussian rigidity and surface tension of the membrane, whose surface area is $A$. The gauge invariants $H = (c_1 + c_2) / 2$ and $K = c_1 c_2$ are respectively the mean and Gaussian curvature of the membrane, where $c_1$ and $c_2$ are the two principal radii of curvatures, and $H_0$ is the spontaneous curvature (magnitude of imposed deformation) imposed on the membrane by a curvature modulating factor, which in general denotes any heterogeneity in composition of the membrane. For a membrane with fixed topology and for constant $\kappa'$, by virtue of the Gauss-Bonnet theorem, the Gaussian rigidity term remains a constant irrespective of the membrane morphology, and is hence not included in our studies using Monte Carlo methods.

In our model, the Exo70 proteins interacting with the membrane is represented by a nematic vector $\boldsymbol{n}$, which represents the orientation of proteins averaged over a small membrane patch, the size of which sets the smallest length scale $a_0$ in the mesoscopic model. The nematic field is representative of the anisotropic nature of the membrane deformation seen in the CGMD simulation. These nematic vectors interact among themselves leading to an orientational order in the nematic field. This self-interaction, promoting orientational order, is represented by the Lebwohl-Lasher form of the Frank's free energy for liquid crystals given by,

$$\mathcal{H}_{\text{nem-nem}} = \frac{1}{2}\sum_{v=1}^{N_v}\sum_{v'=1}^{Z_v} -\varepsilon_{LL}(3\cos^2\theta'_{vv} - 1). \qquad (Mesoscale-2)$$

The first summation index $v$ runs over all membrane vertices and $v'$ runs over its $Z_v$ neighboring vertices. $\varepsilon_{LL}$ is the orientational stiffness and $\theta_{vv'}$ is the angle between $\boldsymbol{n}(\boldsymbol{v})$ and $\boldsymbol{n}(\boldsymbol{v'})$, computed on the curved manifold through a discrete parallel transport. $\boldsymbol{n}(\boldsymbol{v})$ is a two-dimensional unit vector confined to the surface of the membrane, as a protein does, and subtends an angle $\varphi$ with the maximally curved direction of the membrane. We extend the Helfrich Hamiltonian, Eq. (Mesoscale-1), to include anisotropic curvature and account for the protein membrane interaction through an anisotropic energy term given by,

$$\mathcal{H}_{\text{nem-mem}} = \frac{1}{2}\sum_{v=1}^{N_v}\left\{\kappa_{\parallel}\left(c_1\cos^2\varphi + c_2\sin^2\varphi - H_0^{\parallel}\right)^2\right\}A_v\,. \quad (Mesoscale-3)$$

where $\kappa_{\parallel}(\kappa_{\perp})$ and $H_0^{\parallel}(H_0^{\perp})$ are respectively the anisotropic bending stiffness and anisotropic spontaneous curvature parallel (perpendicular) to the nematic field $\boldsymbol{n}$. This model has been earlier used (Ramakrishnan 2012; Ramakrishnan 2013) to demonstrate how biologically relevant membrane morphologies can be stabilized in response to the imposed curvature. The nematic field evolves through a set of Monte Carlo moves that sample the phase space of the system that spans over the membrane position, triangulation and nematic field orientations using the Metropolis algorithm. It should also be noted that the anisotropic curvature field is represented in units of $a_0$ such that $H_0^{\parallel} = \alpha a_0^{-1}$. The total energy of the membrane with nematic field is $\mathcal{H}_{\mathrm{tot}} = \mathcal{H}_{\mathrm{el}} + \mathcal{H}_{\mathrm{nem-nem}} + \mathcal{H}_{\mathrm{nem-mem}}$. For the set of elastic parameters $\kappa = 20k_BT, \epsilon_{LL} = 3k_BT$ and $\kappa_{\parallel} = 5k_BT$ membrane invaginations are seen only for directional curvatures with $\alpha < -0.6$, see Figure 2.11. Below, we combine this result from the mesoscale model with the average membrane deformation energy $\langle E \rangle$ computed from the CGMD simulations (Figure 2.12C) in order to predict the threshold protein density required to induce tubular invaginations (Figure 2.11) for various Exo70 systems.

For an imposed value of $H_0^{\parallel}$, the nematic-membrane energy $\mathcal{H}_{\mathrm{nem-mem}}$ is minimized when the directional curvature of the membrane is such that $c_1 \cos^2 \varphi + c_2 \sin^2 \varphi = H_0^{\parallel}$. Hence the mean curvature of the membrane at every vertex (H) and the energy per vertex $E_{vertex}$ of the triangulated surface are given by:

$$H = \frac{H_0^{\parallel}}{2} = \frac{\alpha}{2a_0} \text{ and } E_{vertex} = \frac{1}{2}\left(\frac{H_0^{\parallel}}{2}\right)^2 A_v. \quad (Mesoscale - 4)$$

To account for the presence of multiple proteins (n) represented by the curvature field vector, we assume that the mean curvature energy $\langle E \rangle$ shown in Figure 2.12C scales linearly with the number of proteins n. The minimum value of n per membrane area $A_v$ necessary for inward-tubule invagination is estimated using the criterion $E_{vertex}=n\langle E \rangle$, where $A_v = \sqrt{3}(1.3a_0)^2/2$ is the average area of the vertex in units of $a_0$. The expression for n reduces to (see Figure 2.12F):

$$n = \frac{\sqrt{3}(1.3)^2\alpha^2}{16\langle E \rangle}. \quad (Mesoscale - 5)$$

The theoretical maximum value of the number of proteins $n^*$ in area $A_v$ is estimated as $n^* = (A_v = 294\ \text{nm}^2)$ / (molecular area). Based on the molecular areas of the different systems (monomer=150 nm$^2$, parallel dimer=200 nm$^2$, and anti-parallel dimer=240 nm$^2$), the value of $n^*$ is estimated in Figure 2.12F. Note that n is a parameter set for mesoscale simulations while the maximum number n* is based on CGMD simulations; if n<n*, inward-tubulation is predicted to occur and if n>n*, inward-tubulation is predicted not to occur. Hence, the computed numbers collectively imply that tubulation occurs only for the parallel and anti-parallel wild type dimer systems. Alternatively, noting that the anti-parallel dimer system barely satisfies the constraint n<n* (see Figure 2.12F), we can estimate the critical radius of curvature $R^* = \langle 2H^*_{\text{max}} \rangle^{-1}$ as 53.4 nm. For systems with R>R*, we expect no tubulation and for systems with R<R*,

we expect tubulation, again predicting that the wild type parallel (R=40 nm) and anti-parallel dimers (R=53 nm) are the only systems expected to stabilize inward-tubulation. The different radii of curvature along with the threshold R* are depicted in Figure 2.11 of main text.

*** This work has been published in *Developmental Cell* in August 2013 (Zhao et al., 2013).**

# CHAPTER 3 EXO70 COUPLES MEMBRANE DYNAMICS AND ACTIN DYNAMICS DURING DIRECTIONAL CELL MIGRATION

## ABSTRACT

Directional cell migration requires the coordination of actin assembly and membrane remodeling. A component of the exocyst, Exo70, directly interacts with and activates the Arp2/3 complex, a central nucleating factor for the generation of branched actin networks for cell morphogenesis and migration. Exo70 induces tubular membrane invaginations towards the lumen of synthetic vesicles *in vitro* and generates protrusions on the surface of cells. Here I found that both the stimulatory effect of Exo70 on Arp2/3 and the membrane-deformation function of Exo70 are required for lamellipodia formation and maintaining directional persistence of cell migration. Exo70 thus may couple actin dynamics and plasma membrane remodeling during cell migration.

## 3.1 INTRODUCTION

Membrane protrusions at the leading edge are important for directional cell migration (Pollard and Borisy, 2003; Mattila and Lappalainen, 2008; Ridley, 2011). A branched actin network mediated by the Arp2/3 complex "pushes" the plasma membrane to generate surface protrusions, which is the physical step that initiates directional cell migration (Pollard and Borisy, 2003; Ridley, 2011). Recently, accumulating evidence suggests an important role of membrane curvature induction for protrusion formation (Bereiter-Hahn, 2005; Suetsugu et al., 2006; Mattila et al., 2007; Ji et al., 2008; Yang et al., 2009; Guerrier et al., 2009). It still remains unclear how actin assembly and membrane remodeling are coordinated at the leading edge.

The exocyst complex, consisting of Sec3, Sec5, Sec6, Sec8, Sec10, Sec15, Exo70 and Exo84, mediates the tethering of secretory vesicles at the plasma membrane for exocytosis and cell surface expansion (Hsu et al., 2004; Munson and Novick, 2006; He and Guo, 2009). The exocyst is implicated in many cellular processes such as epithelia formation, cytokinesis, and neurite branching. Recent evidence has demonstrated that the exocyst is involved in cell migration (Zuo et al., 2006; Rosse et al., 2006; Spiczka and Yeaman, 2008; Liu et al., 2009a; Thapa et al., 2012; Ren and Guo, 2012). In particular, the exocyst component Exo70 directly interacts with the Arpc1 subunit of the Arp2/3 complex and kinetically stimulates actin polymerization and branching (Zuo et al., 2006; Liu et al., 2009a; Liu et al., 2012).

Exo70 has a long rod-like structure that binds to $PI(4,5)P_2$ through positively charged residues on its surface (Dong et al., 2005; Hamburger et al., 2006; Moore et al., 2007; Liu et al., 2007). Overexpression of Exo70, but not any other subunit of the exocyst complex, induces filopodia formation in cells independent of its function in exocytosis (Zuo et al., 2006). Recently I found that Exo70 can directly generate membrane curvature on the synthetic vesicles and at the plasma membrane through an oligomerization-based scaffolding mechanism (Chapter 2).

Since Exo70 can stimulate the activity of the Arp2/3 complex for actin polymerization activity and remodel the plasma membrane, in this study, I characterized specific Exo70 mutants and tested whether they affected the formation of lamellipodial protrusion at the leading edge and directional cell migration. I found that not only the Arp2/3-stimulating function but also the membrane-deforming function of Exo70 is required for lamellipodia formation and cell migration. Exo70 may coordinate the actin and membrane dynamics at the leading edge.

## 3.2 RESULTS

### Characterization of Exo70 mutants defective in membrane deformation

Lipid binding and oligomerization are required for Exo70 to generate membrane curvature (Chapter 2). I further characterized the Exo70(K571A/E572A) and Exo70(Δ1-75) mutants, which are defective in lipid binding and oligomerization, respectively. They maintained the ability to bind to other exocyst components Sec8 and Sec6 (Figure 3.1A),

suggesting that they do not interfere with the formation of the exocyst holo-complex. I then tested whether the function of the exocyst in exocytosis was impaired in the presence of Exo70 mutants using VSV-G-ts45-GFP as an exocytosis marker. Exo70 knockdown by RNAi blocked the incorporation of VSV-G-ts45-GFP to the plasma membrane. As shown in Figure 3.2, addition of wild type Exo70 or Exo70(Δ1-75) was able to fully rescue the exocytosis blockade; while addition of Exo70(K571A/E572A) led to a partial rescue, which is consistent with the previous observation that Exo70-lipid interaction is required to target the exocyst to the plasma membrane for exocytosis (Liu et al., 2007).

Exo70 can directly bind to the Arpc1 subunit of the Arp2/3 complex (Zuo et al., 2006); both Exo70(K571A/E572A) and Exo70(Δ1-75) maintained their ability to bind Arpc1 (Figure 3.1B). Exo70 was shown to stimulate the Arp2/3 complex-mediated actin polymerization *in vitro* (Liu et al., 2012). I employed a pyrene actin polymerization assay to test whether Arp2/3-stimulating activity was affected in cells expressing the Exo70(K571A/E572A) and Exo70(Δ1-75) mutants (Figure 3.3). Exo70 knockdown reduced the rate of actin polymerization mediated by Arp2/3 in the presence of VCA domain of N-WASP, a potent Arp2/3 activator (Liu et al., 2009a). Addition of either wild type Exo70, Exo70(K571A/E572A) or Exo70(Δ1-75) fully restored this reduction. By contrast, addition of Exo70(Δ628-630) which is defective in Arp2/3-binding (Zuo et al., 2006; Liu et al., 2012), failed to rescue.

**Figure 3.1**

**A.**

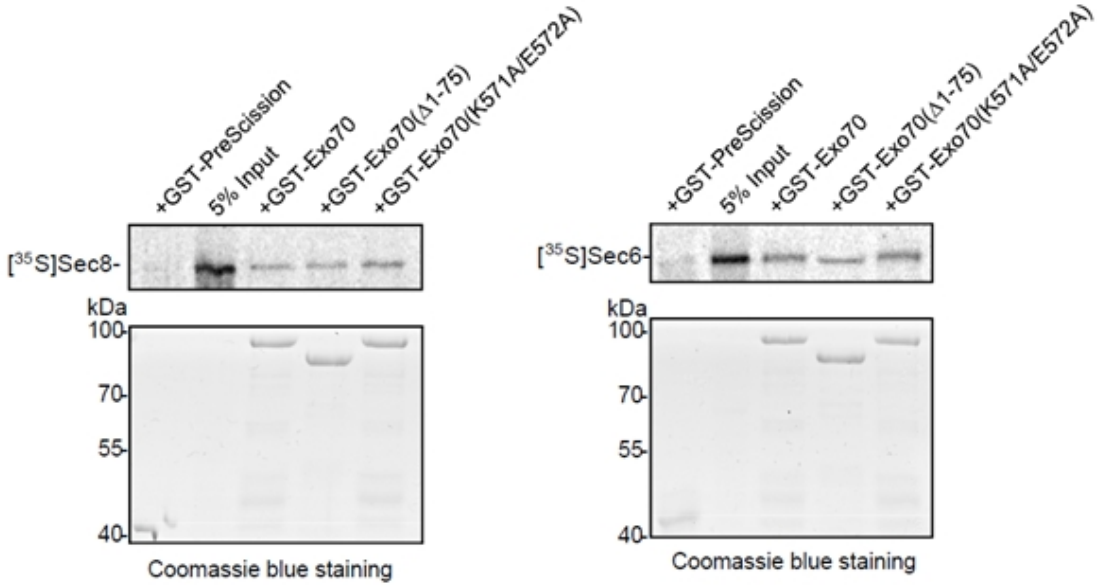
+GST-PreScission
5% Input
+GST-Exo70
+GST-Exo70(Δ1-75)
+GST-Exo70(K571A/E572A)
[35S]Sec8-
kDa
100
70
55
40
Coomassie blue staining
+GST-PreScission
5% Input
+GST-Exo70
+GST-Exo70(Δ1-75)
+GST-Exo70(K571A/E572A)
[35S]Sec6-
kDa
100
70
55
40
Coomassie blue staining

**B.**

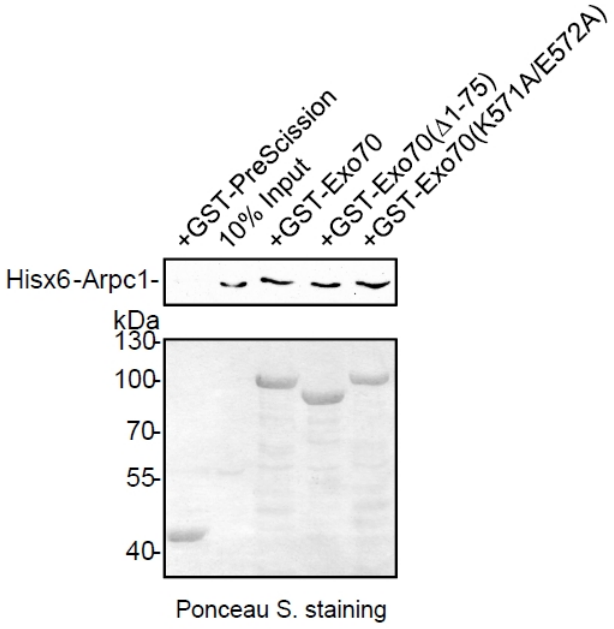
+GST-PreScission
10% Input
+GST-Exo70
+GST-Exo70(Δ1-75)
+GST-Exo70(K571A/E572A)
Hisx6-Arpc1-
kDa
130
100
70
55
40
Ponceau S. staining

**Figure 3.1 Characterization of Exo70 mutants in exocyst and Arpc1 binding**

**(A)** In vitro binding of wild type and mutant Exo70 with Sec8 (top left panel) and Sec6 (top right panel). Sec8 and Sec6 were in vitro transcribed and translated in the presence of [$^{35}$S] methionine using a TnT Quick Kit (Promega), and then incubated with GST-tagged Exo70 conjugated to glutathione Sepharose. The bound proteins were analyzed by SDS-PAGE and autoradiography (top panel). The gel was stained with Coomassie blue (lower panel). The GST-PreScission fusion protein was used as a negative control. **(B)** In vitro binding between Exo70 and Hisx6-Arpc1. Recombinant Hisx6-Arpc1 was incubated with GST-tagged Exo70 conjugated to glutathione Sepharose. The input (10%) and bound Hisx6-Arpc1 were analyzed by Western blotting using an anti-Hisx6 antibody (top panel). Exo70 fusion proteins on the membrane were stained with Ponceau S. (lower panel).

**Figure 3.2**

**A.**

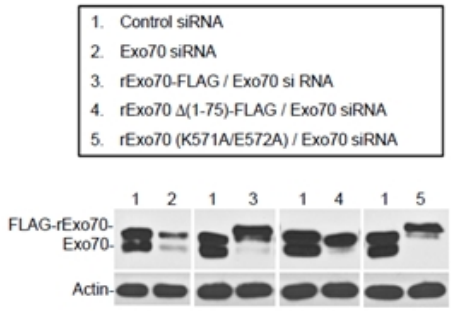


**C.**

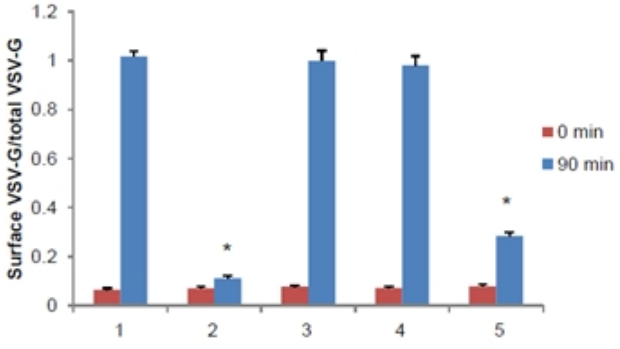


**B.**

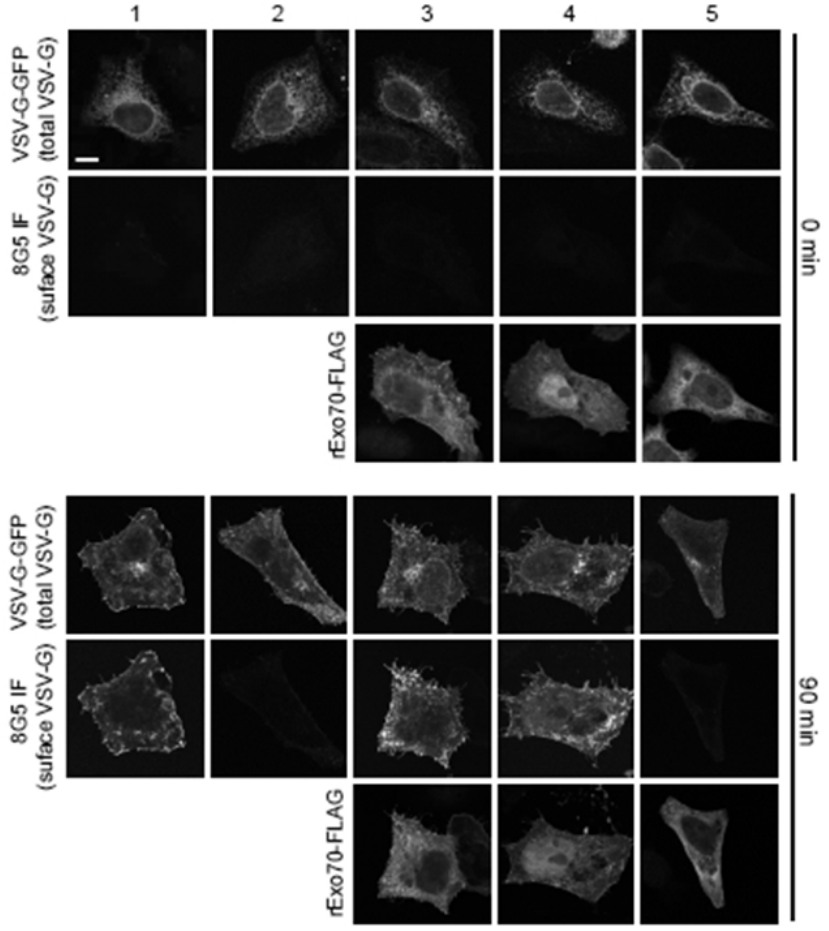

**Figure 3.2 Characterization of Exo70 mutants in regulating VSV-G trafficking**

VSV-G trafficking assay was performed as described previously (Liu et al., 2007). HeLa cells were transfected with Exo70 siRNA. Luciferase siRNA was used as a negative control. After 24 hours of siRNA treatment, HeLa cells were transfected with VSV-G-45ts-GFP mutant and FLAG-tagged rat Exo70 variants and immediately placed in a 40°C incubator. After overnight growth, the cells were shifted to 32°C for different times in the presence of cycloheximide (100 μg/ml). **(A)** Western blots showing Exo70 knockdown in HeLa cells and the expression of FLAG-tagged Exo70 variants. **(B)** Images of the cells at 0 min and 90 min after temperature shift showing total VSV-G-45ts-GFP (GFP signals), surface VSV-G-45ts-GFP (stained with 8G5 monoclonal antibody against the extracellular domain of VSV-G), and Exo70 variants expression (FLAG staining). Scale bar, 5 μm. **(C)** The ratios of surface VSV-G over total VSV-G for each treatment at 0 min and 90 min (also see METHODS). Depletion of Exo70 blocked surface incorporation of VSV-G-45ts-GFP, which were fully rescued by the wild type Exo70-FLAG and Exo70(Δ1-75)-FLAG, and only partially rescued by Exo70(K571A/E572A)-FLAG. Error bars, s.e.m. n=30; *, $p<0.01$.

**Figure 3.3**

**A.**

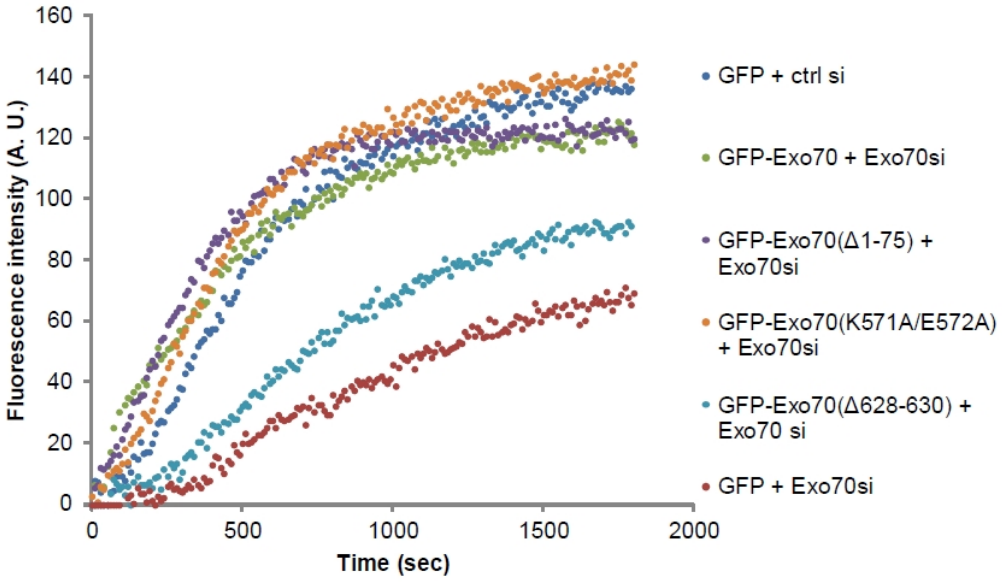
Fluorescence intensity (A. U.)
160
140
120
100
80
60
40
20
0
0
500
1000
1500
2000
Time (sec)
GFP + ctrl si
GFP-Exo70 + Exo70si
GFP-Exo70(Δ1-75) + Exo70si
GFP-Exo70(K571A/E572A) + Exo70si
GFP-Exo70(Δ628-630) + Exo70 si
GFP + Exo70si

**B.**

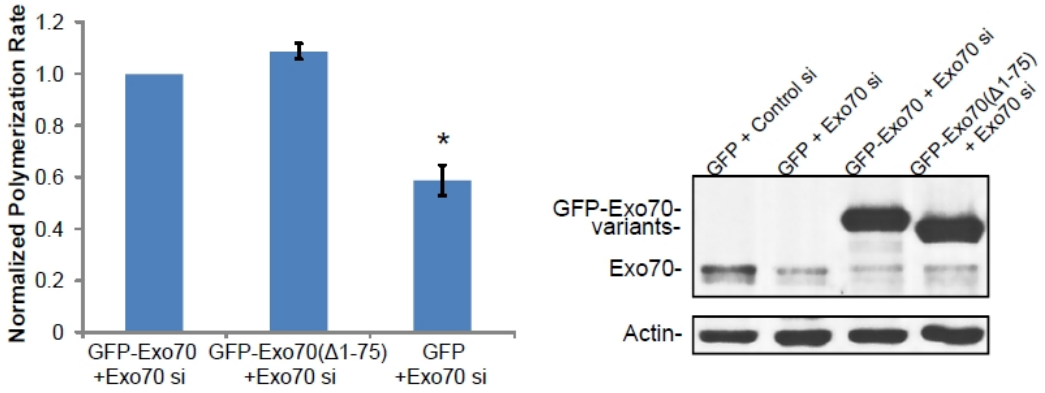
Normalized Polymerization Rate
1.2
1.0
0.8
0.6
0.4
0.2
0
*
GFP-Exo70 +Exo70 si
GFP-Exo70(Δ1-75) +Exo70 si
GFP +Exo70 si
GFP + Control si
GFP + Exo70 si
GFP-Exo70 + Exo70 si
GFP-Exo70(Δ1-75) + Exo70 si
GFP-Exo70-variants-
Exo70-
Actin-

**Figure 3.3 Characterization of Exo70 mutants in stimulating actin polymerization**

The ability of the lysates from Exo70 knockdown cells expressing different Exo70 variants to stimulate actin polymerization was analyzed by pyrene actin assay in the presence of the VCA domain of N-WASP as described in Methods. **(A)** Lysates from Exo70 siRNA knockdown cells showed reduced actin polymerization. Expression of GFP-Exo70, GFP-Exo70(Δ1-75) and GFP-Exo70(K571A/E572A), but not GFP-Exo70(Δ628-630) (Arp2/3-binding-defective), rescued this phenotype induced by Exo70 siRNA. **(B)** Actin polymerization rates (the maximal slops of the elongation phase of each curve) were compared after normalized to GFP-Exo70 + Exo70 siRNA. GFP-Exo70(Δ1-75) had the same activity as GFP-Exo70 to stimulate actin polymerization. Error bars, s.e.m. n=4; *, $p < 0.01$. Endogenous and exogenous Exo70 levels were examined by Western blot, along with the amounts of actin in cell lysates.

The results above suggest that Exo70(Δ1-75) is a specific mutant for Exo70-induced membrane deformation because it does not affect other Exo70 functions such as exocytosis and Arp2/3-stimulation. Exo70(K571A/E572A) is less specific as it is also deficient in exocytosis in addition to membrane deformation.

**Exo70 mediates leading edge protrusion**

To test how Exo70 mutants affect the formation of leading edge protrusions, human MDA-MB-231 cell lines stably expressing GFP-tagged rat Exo70 variants were generated, including wild type Exo70, Exo70(Δ628-630), Exo70(K571A/E572A) and Exo70(Δ1-75). The endogenous Exo70 was then knocked down by siRNA in these cells. The levels of knockdown were confirmed by Western blotting (Figure 3.4A). The Exo70 knockdown cells expressing Exo70 membrane-deformation mutants were dramatically defective in their ability to form lamellipodial protrusions as revealed by Arp3 and F-actin staining (Figure 3.4B). The "lamellipodia ratio", defined as the length of the leading edge divided by the total cell perimeter, was significantly lower in the knockdown cells expressing Exo70 mutants (Figure 3.4C). These results suggest that both membrane-deforming activity and Arp2/3-stimulating activity of Exo70 is required for the formation of lamellipodia.

**Exo70 mediates directional cell migration**

To test the effect of Exo70 mutants in directional cell migration, three assays were performed. First in a transwell assay, cells were allowed to migrate from an upper

**Figure 3.4**

**A.**

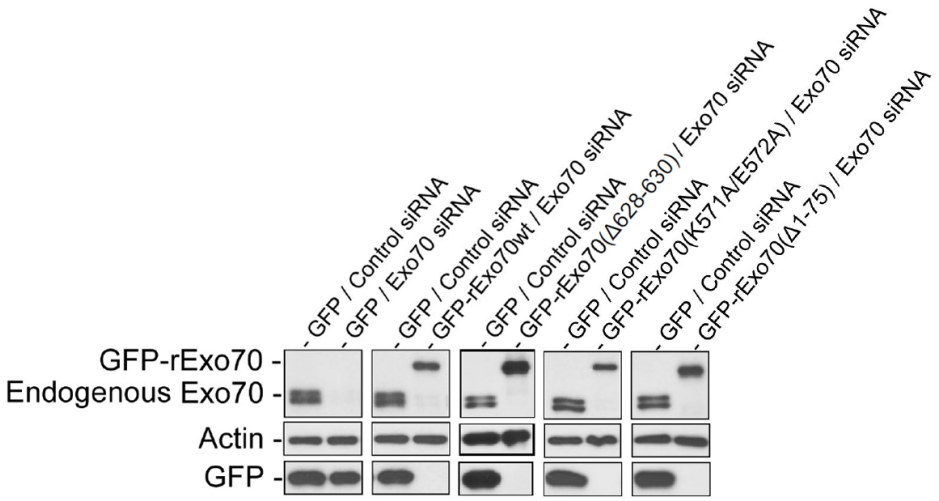


**B.**

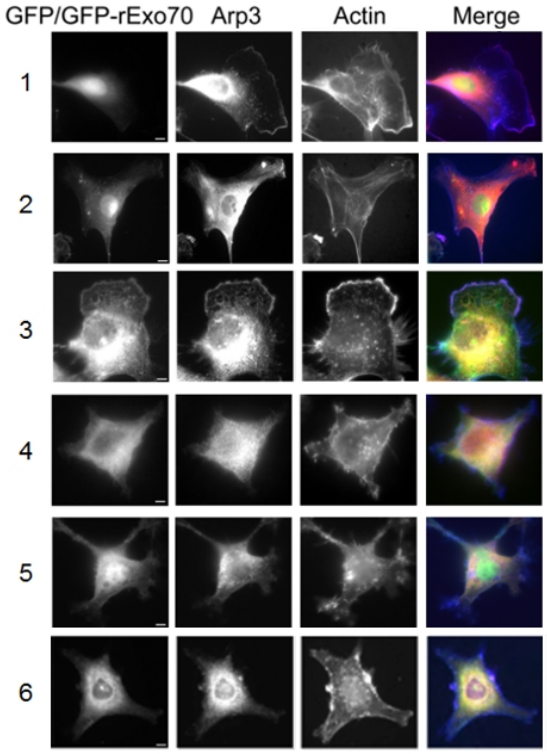


1. GFP / Control siRNA
2. GFP / Exo70 siRNA
3. GFP-Exo70 WT/ Exo70 siRNA
4. GFP-Exo70(Δ628-630)/ Exo70 siRNA
5. GFP-Exo70(K571A/E572A)/ Exo70 siRNA
6. GFP-Exo70(Δ1-75)/ Exo70 siRNA

**C.**

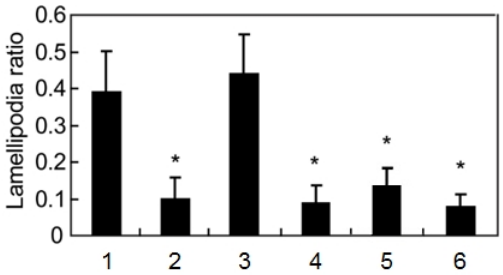

**Figure 3.4 The roles of Exo70 in lamellipodia formation**

**(A)** Exo70 knockdown in MDA-MB-231 cells stably expressing GFP or GFP-tagged rat Exo70 variants. Control siRNA or Exo70 siRNA were transfected into MDA-MB-231 cells stably expressing GFP or GFP-tagged rat Exo70 variants including Exo70, Exo70(Δ628-630), Exo70(K571A/E572A) and Exo70(Δ1-75). The amounts of endogenous Exo70 and exogenously expressed various GFP-tagged rat Exo70 constructs were detected by anti-Exo70 monoclonal antibody. The expression of GFP was detected by anti-GFP monoclonal antibody. The amounts of actin in all treatments, detected by an anti-actin antibody, were also examined as loading controls. **(B)** MDA-MB-231 cells expressing indicated siRNA and GFP-tagged rat Exo70 variants were stained for Arp3 (red) and F-actin (blue) to detect lamellipodia. Control siRNA-treated cells (Panel 1) had clear and extended lamellipodia. In Exo70-knockdown cells (Panel 2), the formation of lamellipodia was impaired. Expression of GFP-rExo70 (Panel 3) rescued lamellipodia formation, whereas the expression of Exo70 mutants failed to rescue the defect (Panel 4-6). Scale bar, 5 μm. **(C)** The ratios between the length of the lamellipodia and the total cell perimeters ("lamellipodia ratio") were compared for each group. The mutant groups have lower lamellipodia ratios. Error bars, SD. n=25; *, $p<0.01$.

**Figure 3.5**

**A.**

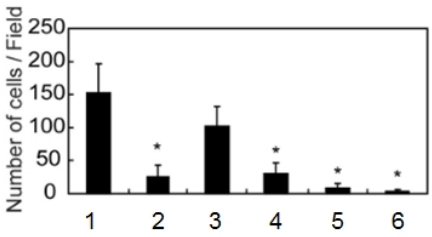


1. GFP / Control siRNA
2. GFP / Exo70 siRNA
3. GFP-Exo70 WT/ Exo70 siRNA
4. GFP-Exo70(Δ628-630)/ Exo70 siRNA
5. GFP-Exo70(K571A/E572A)/ Exo70 siRNA
6. GFP-Exo70(Δ1-75)/ Exo70 siRNA

**B.**

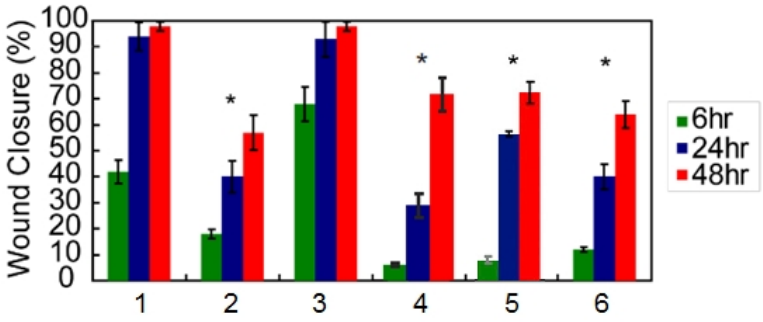


**C.**

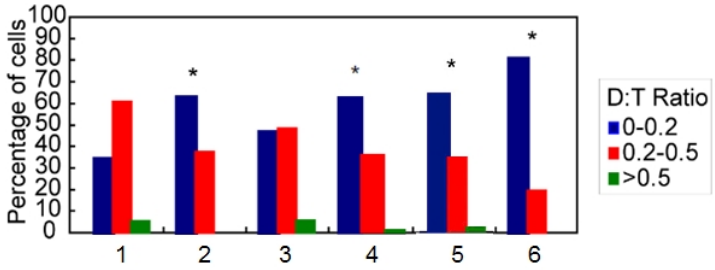

**Figure 3.5 The roles of Exo70 in directional cell migration**

**(A)** Transwell assays were performed using cells described in text. The bars indicate the average number of migrated cells per field for each group. Error bars, SD. n=3; *, $p<0.01$. **(B)** Wound-healing assays were performed. The percentage of wound closure (closure distance over initial opening) after 6, 24, and 48 hours of migration was calculated for each group. Error bars, SD. n=3; *, $p<0.01$. **(C)** Single cell movement was tracked using time-lapse microscopy. Directional persistence of individual cells was calculated as D:T ratio (see text). The percentage of cells with different D:T ratios (0-0.2; 0.2-0.5; >0.5) is indicated. n=60; *, $p<0.01$.

chamber to a lower chamber through a filter membrane. The numbers of cells passing through the filter to the lower chamber were counted (Figure 3.5A). Exo70 knockdown inhibited migration. Addition of wild type Exo70 fully rescued the migration phenotype. Much fewer Exo70 knockdown cells expressing the Exo70 mutants migrated to the lower chamber, as compared to the control cells.

Second, in a wound-healing assay, open space ("wound") was introduced in confluent cell monolayers. The percentages of wound closure at different time points were compared (Figure 3.5B). It took the Exo70 mutant cells longer time to close the wounds than control or wide type Exo70 cells with Exo70 depletion.

Finally, by tracking the trajectories of individual cells over time (see METHODS), I found that cells expressing Exo70 mutants were not only slower in migration, but also less capable of maintaining the direction of their movement (Figure 3.5C). The cells with compromised Exo70 function made more turns than the control cells or cells rescued by wild type Exo70. To quantify the directional persistence, the ratio of the net displacement of the cell to the total migration distance ("D:T ratio") was calculated. The D:T ratio was much smaller in cells expressing Exo70 mutants than control or wild type Exo70 cells with Exo70 depletion.

In summary, these results suggest that the Arp2/3-stimulating activity and the membrane-deforming activity of Exo70 play an important role in membrane protrusion formation and directional cell migration.

## 3.3 DISCUSSION

Exo70 is able to kinetically stimulate the Arp2/3 complex in the presence of WAVE2 for actin polymerization and branching. Exo70 binds to the Arp2/3 complex through Arpc1, the subunit that physically contacts N-WASP/WAVE for activation (Liu et al., 2012). Thus, it follows reasonably that the Exo70(Δ628-630) mutant, which is defective in Arp2/3 complex binding, is not able to rescue the inhibition of lamellipodia formation and cell migration caused by Exo70 knockdown. However, our data suggest that the Exo70(Δ1-75) mutant, which is specifically defective in oligomerization and membrane deformation, is also unable to rescue the inhibition of lamellipodia formation and cell migration. These results suggest a direct link between membrane-deforming activity and cell migration.

Membrane curvature induction is often coupled with cytoskeletal activities (for review, see Doherty and McMahon, 2008; Scita et al., 2008). The function of Exo70 in actin dynamics can be coordinated with its ability to induce membrane curvature during such processes as morphogenesis and cell migration. It is thought in the field that a branched actin network mediated by the Arp2/3 complex "pushes" the plasma membrane for cells to generate protrusion. Recent findings that I-BAR and F-BAR proteins induce filopodia protrusion, led to the appreciation that membrane curvature also contributes to the protrusion formation (Mattila et al., 2007; Mattila and Lappalainen, 2008; Yang et al., 2009; Guerrier et al., 2009). It is plausible that Exo70, like I-BAR and F-BAR proteins, uses its membrane-deforming activity in leading edge protrusion and directional cell

migration. The ability of Exo70 to induce negative membrane curvature may create a space at the leading edge to accommodate active actin polymerization and branching mediated by the Arp2/3 complex. Exo70 may thus couple membrane remodeling and actin dynamics for effective protrusion formation and cell migration.

Previous studies have shown that the Exo70-Arp2/3 complex interaction is stronger in cells treated with EGF (Zuo et al., 2006), or expressing Y527F c-Src (Liu et al., 2009a), which are known to stimulate membrane protrusion and cell migration. Moreover, the plasma membrane association of Exo70 is regulated by small GTPases (e.g., TC10, Inoue et al., 2003) and kinases (e.g., ERK1/2, Ren and Guo, 2012), especially. It will be interesting to examine how different signaling events regulate the Arp2/3-stimulating and/or membrane-deforming activities of Exo70. Future investigation of these regulations will lead to better understanding of many processes such as chemotaxis and tumor cell invasion.

## 3.4 MATERIALS AND METHODS

### Plasmids and antibodies

Full-length rat Exo70 and Exo70(Δ1–75) were cloned in-frame into pEGFP-C1 vector or p3xFLAG-CMV-14 vector for expression in cells. Full-length rat Exo70 was cloned in-frame into pJ3-RFP-Ruby for expression in cells. The Exo70 mutant Exo70(K571A/E572A) and Exo70(Δ628-630) were generated using the QuikChange site-directed mutagenesis kit (Stratagene). Different Exo70 variants were also cloned in-

frame into pGEX-KG (a modified form of pGEX-2T) or pGEX-6P-1 (GE Healthcare/ Amersham Biosciences) for bacterial expression. Monoclonal antibody against Exo70 was obtained from Dr. Shu-Chan Hsu (Rutgers University). Mouse anti-actin mAb (MAB 1501, clone C4) was purchased from Chemicon, Millipore; mouse monoclonal anti-Hisx6 antibody (MMS-156R) and monoclonal antibody against GFP (MMS-118R, clone B34) from Covance, monoclonal antibody against FLAG (F3165, clone M2) was purchased from Sigma and polyclonal antibody against FLAG (A00170) was purchased from Genescript. The 8G5 monoclonal antibody against the extracellular domain of VSV-G was a kind gift from Dr. Douglas Lyles (Wake Forest University).

**Protein purification**

GST fusion proteins were expressed in *E. coli* strain BL21-CodonPlus(DE3)-RP and purified using glutathione Sepharose 4B (GE Healthcare). His6-Arpc1 was purified from *E. coli* with TALON beads.

**Cell culture and transfection**

MDA-MB-231 and HeLa cells were maintained at 37°C in DMEM (Invitrogen) supplemented with 10% FBS, 2 mmol/L l-glutamine, 100 U /ml penicillin, and 100 µg/ml streptomycin in a 5% $CO_2$ incubator. DNA transfections into cells were carried out using Lipofectamine 2000 (Invitrogen). For RNA interference (RNAi), cells were grown to 50% confluence and transfected with small interfering RNA (siRNA) duplexes using Lipofectamine 2000. The human Exo70 siRNA target sequence used in the experiments

is 5'-GGTTAAAGGTGACTGATTA-3'. The control Luciferase GL2 siRNA target sequence is 5'-AACGTACGCGGAATACTTCGA-3'. The efficiency of the knockdown was determined by Western blotting. Stable MDA-MB-231 cell lines expressing GFP, GFP-tagged wild-type and mutant Exo70 were selected by G418 at a concentration of 1 μg/ml. The cells were further selected using fluorescence activated cell sorting (FACS) and maintained in growth medium for 2 weeks.

### *In vitro* binding assay

For *in vitro* binding assay, rat Sec8 and Sec6 were *in vitro* transcribed and translated in the presence of [$^{35}$S] methionine using a TnT Quick Kit (Promega), and then incubated with GST-tagged Exo70 variants conjugated to glutathione Sepharose 4B beads in binding buffer (50 mM Tris-HCl pH 8.0, 135 mM NaCl, 1mM EDTA, 1 mM $Va_3VO_4$, 0.5% Triton X-100). After overnight incubation at 4°C, beads were washed three times. The bound proteins were analyzed by SDS-PAGE and autoradiography. Recombinant Hisx6-Arpc1 was incubated with GST-tagged Exo70 variants as described above. The bound proteins were analyzed by Western blotting using an anti-Hisx6 antibody.

### VSV-G trafficking assay

VSV-G trafficking assay was performed as described previously (Liu et al., 2007). HeLa cells were transfected with Exo70 siRNA. Luciferase siRNA was used as a negative control. After 24 hours of the siRNA treatment, HeLa cells were transfected with VSV-G-45ts-GFP mutant and FLAG-tagged Exo70 variants and immediately placed at 40°C.

After overnight growth, the cells were shifted to 32°C for different times in the presence of cycloheximide (100μg/ml). The cells were then fixed for GFP observation and immunofluorescence using the 8G5 mAb against the extracellular domain of VSV-G without cell permeabilization. Subsequently, cells were permeabilized and stained with anti-FLAG polyclonal antibody to detect the expression of transfected FLAG-tagged Exo70. Anti-mouse Alexa594 and anti-rabbit Alexa633 were used as secondary antibodies in these experiments. Images were obtained using Leica DMI 6000B inverted microscope equipped with a DFC350 FX camera and a 63x objective. Surface VSV-G intensity (8G5 signal) and total VSV-G intensity (GFP signal) were measured by ImageJ software. Three independent experiments were carried out. 30 cells were analyzed for each treatment.

**Pyrene actin assay**

Pyrene actin assay was performed as described in Liu et al., 2009a. Cell lysates were collected in a buffer containing 20 mM Tris-HCl, pH 7.5, 25 mM KCl, 1 mM $MgCl_2$, 0.5 mM EGTA, 0.1 mM ATP, and protease inhibitor cocktail [Sigma P8340, 4-(2-aminoethyl) benzenesulfonyl fluoride, pepstatin A, E-64, bestatin, leupeptin, and aprotinin], and 1 mM DTT and spun successively at 16,000 × g for 15 min and 80,000 rpm in a Beckman TLA-100.3 rotor (Fullerton, CA) for 20 min at 4°C. The resulting high-speed supernatant (HSS) was used for later experiments. Pyrenyl-actin was dissolved in column buffer (TEA, 0.3 mM $CaCl_2$, 0.1 mM EDTA, 0.7 mM ATP, and 6.25 mM $NaN_3$) for 1 hour, spun at 80,000 rpm in a Beckman TLA-100.3 rotor for 20 min at 4°C to remove F-actin,

and mixed with $Mg^{2}$+ converting buffer for 5 min to convert $Ca^{2+}$-actin to $Mg^{2+}$-actin. $Mg^{2+}$-pyrenl-actin was then diluted in the polymerization buffer (60 mM KCl, 2.5 mM NaCl, 0.6 mM $MgCl_2$, 5 mM Tris-HCl, pH 7.5, 2.5 mM HEPES, pH 7.1, 0.5 mM EGTA, 30 μM $CaCl_2$, 0.2 mM ATP, and 0.3 mM $NaN_3$) to a final concentration of 1.5 μM and immediately mixed with HSS, which contained 2.4–2.6 μM unlabeled G-actin as estimated by Western blot (data not shown) in the presence of 0.2 mM ATP and 50 nM GST-tagged verprolin, cofilin, and acidic (VCA) domain of mammalian N-WASP. The mixture was quickly transferred into a well of 96-well plate, and the fluorescence intensity was read every 10 s in a Molecular Device SpectraMax Gemini EM plate reader at the wavelength of 365/407 (Ex/Em). Polymerization curves and rates were obtained using Excel (Microsoft). The polymerization rate was represented as the maximal slope of the elongation phase of each curve.

**Fluorescence microscopy**

MDA-MB-231 cells with different treatments were grown on coverslips, washed with phosphate-buffered saline (PBS), fixed in 4% formaldehyde at room temperature for 12 min, washed, permeabilized for 5 min with PBST (PBS-Tween), and blocked for 10 min with 2% bovine serum albumin in PBST. To quantify lamellipodial protrusion, MDA-MB-231 cells were co-stained with an anti-Arp3 polyclonal antibody and Alexa Fluor 350 phalloidin (Invitrogen/Molecular Probes) for fluorescence observation using Leica DMI 6000B inverted microscope equipped with a DFC350 FX camera and a 63x objective. Images were processed with Adobe Photoshop (Adobe Systems, version 7.0).

"Lamellipodia ratio" was defined as the perimeter occupied by the lamellipodia to the whole cell perimeter as measured by ImageJ 1.73v software.

**Transwell migration assay**

MDA-MB-231 cells (1 $x10^5$ cells per well) with different treatments were seeded in the upper chamber of a transwell filter with 6.5-mm diameter, 8-μm pore size membrane (Corning Inc.) in DMEM without serum. Cells were allowed to migrate across the filter for 24 hours at 37°C towards the lower side of the chamber containing DMEM plus 10% FBS. Cells on the upper side of the filter were removed with cotton swabs, and migrated cells on the lower side of the chamber were fixed and stained with Giemsa stain. The average number of migrated cells in five randomly chosen fields per transwell insert was counted to quantify the extent of migration.

**Wound healing assay**

MDA-MB-231 cells were seeded in 6-well plates (~$2x10^6$ cells per well) for 24 hours. When the cells grew to confluence, scratches were introduced using a sterile 20-μl pipette tip. Cells were washed with PBS and refreshed with regular growth medium. Cells were imaged after wounding at 0, 6, 24 and 48 hours by phase contrast microscopy using Leica DMI 6000B inverted microscope equipped with a DFC350 FX camera and a 10x objective. The percentage of wound closure was calculated by dividing the wound distance by the initial distance.

**Tracking individual cell migration by time-lapse microscopy**

MDA-MB-231 cells were plated on 35-mm glass bottom dishes (MatTek Corporation) at a density of $4x10^4$ cells in Leibovitz's (L-15) medium (GIBCO) and placed in a temperature-controlled chamber. The movement of individual cells was traced with an inverted microscope (Eclipse TE2000-U, Nikon) using a 4× objective. Phase time-lapse recording started 24 hours after plating and images were collected at 5-min intervals over 15 hours. The motility parameters, including migration path, net distance and rate, were obtained from time-lapse movies using Metamorph imaging software. The migration paths were shown as graphs using the Excel (Microsoft). The directional persistence was calculated as a ratio of the net displacement and the total length of migration paths (the "D:T ratio") during a 400-min period. 60 cells were analyzed for each treatment. Each set of experiments was performed in duplicate.

*** This work has been published in *Current Biology* in August 2012 (Liu et al., 2012) and *Developmental Cell* in August 2013 (Zhao et al., 2013).**

# CHAPTER 4 THE ROLE OF MAMMALIAN SEC3 AND AMISYN IN EXOCYTOSIS


## ABSTRACT

The late stage of exocytosis is mediated by the tethering complex the exocyst and the fusion machinery SNARE complexes. The secretory vesicles are first tethered to the plasma membrane by the exocyst and then docking and fusion to the plasma membrane is facilitated by SNARE complex assembly. Accumulating evidence suggests that the exocyst and the plasma membrane SNAREs share several binding partners. Some exocyst components such as Sec3 and Sec6 share sequence homology and structural similarity with known SNARE binding proteins. Other tethering factors like HOPS and Dsl1 directly bind to their cognate SNAREs and regulate SNARE complex assembly. Here I showed that the mammalian exocyst component Sec3, based on its sequence similarity to a SNARE-binding protein amisyn, directly binds to the plasma membrane SNARE Syntaxin4. Both Sec3 and amisyn bind to $PI(4,5)P_2$ through basic residues on the N-terminus. Sec3 may regulate MMP and VSV-G exocytosis in mammalian cells. These results reveal a novel direct interaction between the exocyst and the plasma membrane SNARE and suggest that Sec3 may regulate SNARE activity during mammalian exocytosis.

## 4.1. INTRODUCTION

The exocyst is localized in a polarized fashion to sites of active exocytosis and cell surface expansion, acting as a tethering factor for post-Golgi vesicles to the plasma membrane (He and Guo, 2009; Heider and Munson, 2012). Several lines of evidence suggest that the exocyst complex cross-talks to the plasma membrane SNARE complex. In budding yeast, the plasma membrane SNARE complex assembly is blocked in the exocyst mutants indicating that the exocyst acts upstream of SNARE (Grote et al., 2000). Yeast Sec6p biochemically interacts with the plasma membrane t-SNARE Sec9p (Sivaram et al., 2005). The exocyst and the plasma membrane SNAREs also share several binding partners. Yeast Exo84p interacts with the yeast lethal giant larvae (Lgl) homologue Sro7p (Zhang et al., 2005), which interacts with Sec9p and regulates SNARE complex assembly (Hattendorf et al., 2007). The exocyst complex associates with Sec1p (Wiederkehr et al., 2004), a Sec1/Munc18 (SM) protein which binds to t-SNAREs and stimulates SNARE-mediated membrane fusion *in vitro* (Scott et al., 2004). Mammalian Exo70 interacts with Snapin, a t-SNARE SNAP-23/25 binding partner (Bao et al., 2008).

Some known SNARE binding proteins share sequence homology and structural similarity with the exocyst components. Amisyn, a mammalian protein which contains a v-SNARE domain and binds to plasma membrane t-SNAREs, shows 32% sequence homology with Sec3 N-terminus (Scales et al., 2002). The MUN domain of SM protein Munc-13, which binds to t-SNARE complex (Guan et al., 2008) and regulates fusion activity (Ma et al., 2013), shows remote homology and structural similarity to the

tethering complexes including the exocyst (Pei et al., 2009; Croteau et al., 2009; Li et al., 2011).

Other tethering factors such as the HOPS complex which functions at the yeast vacuole and the Dsl1p complex which functions in Golgi-to-ER transport, interact with their cognate SNAREs (Starai et al., 2008; Ren et al., 2009). HOPS stimulates fusion of reconstituted liposomes containing vacuole SNAREs (Starai et al., 2008; Stroupe et al., 2009; Wickner, 2010). Similarly Dsl1p stimulates the assembly of its cognate SNARE complex (Ren et al., 2009; Spang, 2012). Dsl1p and the exocyst both belong to CATCHR family of tethering factors and the structural similarity may suggest the functional similarity.

Based on the evidence above, I hypothesized that the exocyst may directly regulate SNARE activity and sought for additional direct interactions between the exocyst and t-SNAREs resident on the plasma membrane. The best candidate among the eight exocyst subunits is Sec3. Mammalian Sec3 has been shown to localize to the plasma membrane in addition to the internal compartments and has been implicated in desmosome assembly (Andersen and Yeaman, 2010). Mammalian Sec3 is homologous to t-SNARE binding protein amisyn. We therefore directly assessed the ability of Sec3 to bind to the plasma membrane t-SNAREs and regulate their assembly.

In polarized epithelial cells, the membrane and protein compositions of the apical and basolateral plasma membrane are distinct. The exocyst complex has been implicated in the establishment of this asymmetry and has been shown to localize to the basolateral

membrane (Grindstaff et al., 1998) as well as to the vesicles to initiate the formation of the apical membrane (Bryant et al., 2010). Syntaxin4 is a t-SNARE protein at the basolateral plasma membrane and Syntaxin3 functions at the apical plasma membrane (Low et al., 1996; ter Beest et al., 2005). Thus it is important to test whether Sec3 has any binding preference to Syntaxin4 versus Syntaxin3.

Biochemical and structural studies on yeast Sec3 revealed that the N-terminus of yeast Sec3 has a Pleckstrin Homology (PH) fold which binds to $PI(4,5)P_2$ and small Rho GTPases Cdc42 and Rho1(Zhang et al., 2008; Yamashita et al., 2010; Baek et al., 2010). Despite the low similarity of primary sequences, the mammalian Sec3 and amisyn adopt a similar secondary fold as yeast Sec3. Amisyn (STXBP6) is a 24kDa mammalian protein, which contains a v-SNARE domain to bind t-SNAREs on plasma membrane and negatively regulate secretion of dense core vesicles (Scales et al., 2002; Constable et al., 2005; Castermans et al., 2010). Amisyn is differentially expressed in a human cell model of breast cancer progression (Fernandez et al., 2010) and is a candidate gene for autism (Castermans et al., 2008; Castermans et al., 2010); however, the cellular function of amisyn still remains elusive. It will be informative to compare mammalian Sec3 and amisyn in lipid binding and SNARE binding to investigate their roles in regulating exocytosis and reveal the molecular mechanisms.

Here I first tested the interaction between Sec3 and Syntaxins and found that Sec3 preferentially bound to Syntaxin4. Second, I tested the interaction of mammalian Sec3 and amisyn with $PI(4,5)P_2$ and identified the residues responsible for the interaction.

Finally I employed several cellular trafficking assays to test the role of Sec3 in exocytosis and set up several *in vitro* biochemical assays to investigate the molecular significance of Sec3-Syntaxin4 binding in the future.

## 4.2 RESULTS

### Sec3 binds to the basolateral plasma membrane resident t-SNARE syntaxin4

Mammalian Sec3 contains a PH domain at the N-terminus, followed by a coiled-coil domain (Figure 4.1A). First, I examined whether mammalian Sec3 can directly bind to Syntaxin4 and Syntaxin3 by pull down assay using recombinant proteins (Figure 4.1B and C). The 1-268aa of Sec3 (Sec3N) preferentially bound to Syntaxin4.

Next, I tried to map the domains of Syntaxin4 (Figure 4.1A) and Sec3 required for the interaction (Figure 4.1D). The 1-140aa (PH) of Sec3, which consists of the PH domain, did not bind to Syntaxin4. The N-terminal region (N-peptide, 1-29aa) of Syntaxin4, which has been shown to regulate Syntaxin4 binding to other proteins such as Munc18c (Hu et al., 2007), is required for Sec3 binding. Mutations in v-SNARE domian of Amisyn can abolish the interaction with t-SNARE (Scales et al., 2002; Constable et al., 2005); according to the sequence similarity between Sec3 and Amisyn, I mutated the corresponding residues in Sec3 (L163A, R166Q, I171A) and found that the binding to Syntainx4 was largely reduced by the mutations (Figure 4.1E).

In summary, I found that Sec3 can directly bind to Syntaxin4; this interaction may be through the coiled-coil region of Sec3 and require N-peptide of Syntaxin4.

**Amisyn and Sec3 bind to PI(4,5)$P_2$-containing liposomes**

PI(4,5)$P_2$ is the major phosphatidylinositide in the plasma membrane and comprises 1–5% of total cellular phospholipids (McLaughlin and Murray, 2002). I employed a liposomes co-sedimentation assay to test the protein-lipid interaction as described previously (Zhang et al., 2008). Binding assays were carried out with large unilamellar vesicles (LUVs) composed of the neutral PC and negative charged PI(4,5)$P_2$ at 5% or PS at 20%. As shown in Figure 4.2A, Amisyn bound to LUVs containing 5% PI(4,5)$P_2$ (Kd: 60.31 μM), but not to LUVs containing 100% neutral PC. Amisyn bound very weakly to 20% PS, however in the presence of both 5% PI(4,5)$P_2$ and 20% PS, the binding was enhanced (Kd: 28.67 μM).

The basic stretches in yeast Sec3 are required for PI(4,5)$P_2$ binding (Zhang et al., 2008; Baek et al., 2010). By sequence alignment, I generated Amisyn and Sec3 mutants in which the corresponding Lys were mutated to Ala. I found that the liposome binding of Amisyn (K29-31A) was largely reduced compared to the wild type (Figure 4.2B). Similarly, the basic residues K31-34 of Sec3 N-terminus were required for binding to liposomes containing 5% PI(4,5)$P_2$ (Figure 4.2C).

**Sec3 may regulate the exocytosis of MMPs and VSV-G**

To investigate how Sec3 regulates exocytosis in cells, I assessed the secretion of two exocytic cargos such as matrix metalloproteinases (MMPs) and VSV-G by depleting endogenous Sec3 and/or replacing with Sec3 truncates and mutants.

## Figure 4.1

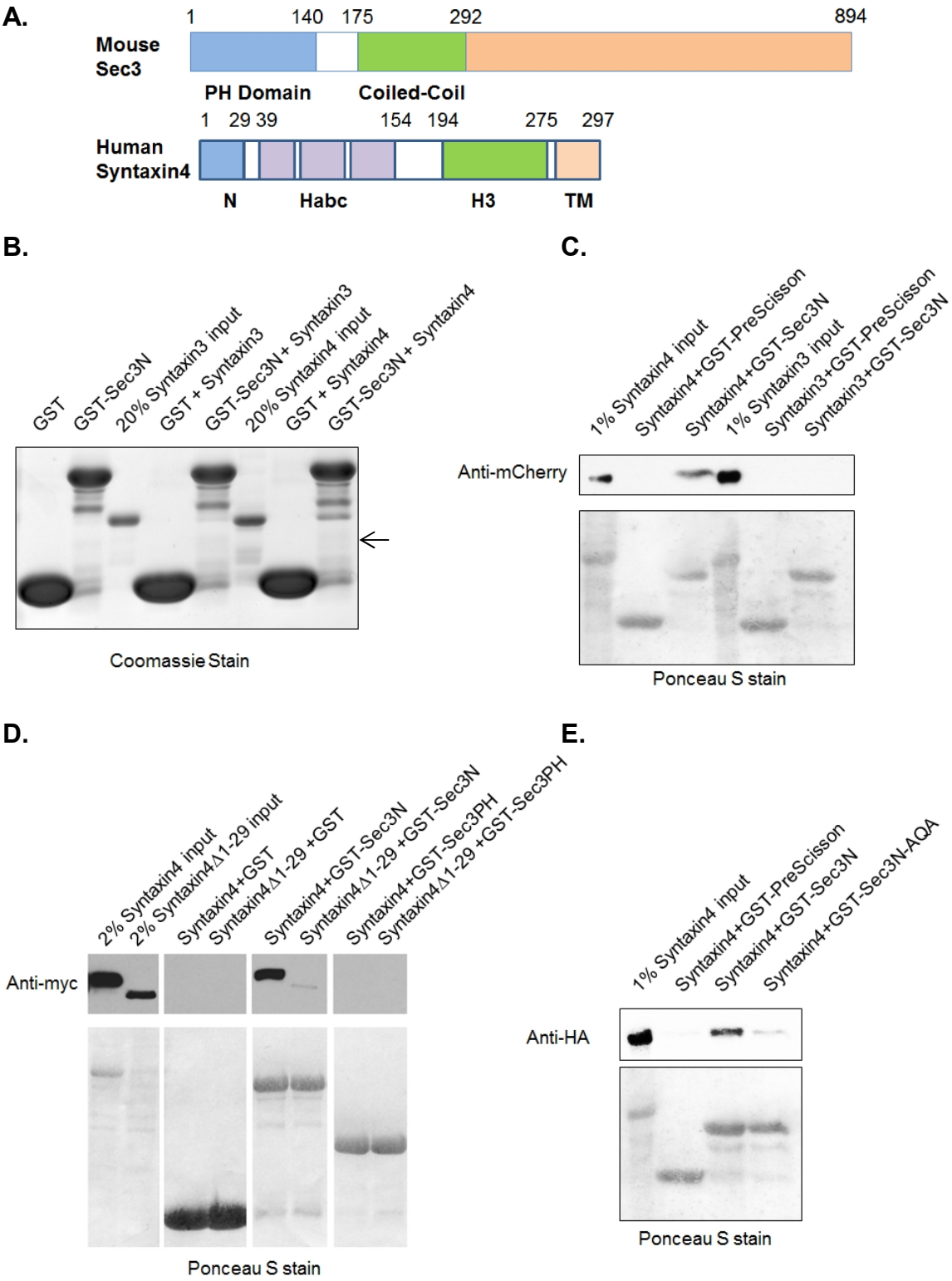
A.
1
140
175
292
894
Mouse Sec3
PH Domain
Coiled-Coil
1
29
39
154
194
275
297
Human Syntaxin4
N
Habc
H3
TM
B.
GST
GST-Sec3N
20% Syntaxin3 input
GST + Syntaxin3
GST-Sec3N + Syntaxin3
20% Syntaxin4 input
GST + Syntaxin4
GST-Sec3N + Syntaxin4
Coomassie Stain
C.
1% Syntaxin4 input
Syntaxin4+GST-PreScisson
Syntaxin4+GST-Sec3N
1% Syntaxin3 input
Syntaxin3+GST-PreScisson
Syntaxin3+GST-Sec3N
Anti-mCherry
Ponceau S stain
D.
2% Syntaxin4 input
2% Syntaxin4Δ1-29 input
Syntaxin4+GST
Syntaxin4Δ1-29 +GST
Syntaxin4+GST-Sec3N
Syntaxin4Δ1-29 +GST-Sec3N
Syntaxin4+GST-Sec3PH
Syntaxin4Δ1-29 +GST-Sec3PH
Anti-myc
Ponceau S stain
E.
1% Syntaxin4 input
Syntaxin4+GST-PreScisson
Syntaxin4+GST-Sec3N
Syntaxin4+GST-Sec3N-AQA
Anti-HA
Ponceau S stain

**Figure 4.1 The interaction between Sec3 and Syntaxin4**

**(A)** Domains of mouse Sec3 and human Syntaxin4 (PH: Pleckstrin homology; TM: transmembrane). **(B)** Recombinant Syntaxin3 and Syntaxin4 purified from bacteria were incubated with glutathione 4B beads coupled with GST and GST-Sec3N (1-268aa). The inputs (20%) and pull-downs were analyzed by SDS-PAGE and SimplyBlue SafeStain staining. **(C)** Lysates of 293T cell expressing cytosolic domain of syntaxins mCherry-Syntaxin3ΔTM and mCherry-Syntaxin4ΔTM were incubated with glutathione 4B beads coupled with GST-PreScission and GST-Sec3N (1-268aa). The inputs and pull-downs were analyzed by Western blot using anti-mCherry polyclonal antibody. The inputs of GST fusion proteins were stained with Ponceau S. Sec3N pulled down Syntaxin4 (arrow) but not Syntaxin3. GST-PreScission serves as a negative control. **(D)** Lysates of 293T cell expressing Syntaxin4-myc and Syntaxin4Δ1-29-myc were incubated with glutathione 4B beads coupled with GST, GST-Sec3N (1-268aa) and GST-Sec3PH(1-140aa). The inputs and pull-downs were analyzed by Western blot using anti-myc monoclonal antibody. The inputs of GST fusion proteins were stained with Ponceau S (data not shown). Sec3N pulled down less Syntaxin4Δ1-29 than Syntaxin4. Sec3PH did not pull down Syntaxin4. **(E)** Lysates of 293T cell expressing Syntaxin4-HA were incubated with glutathione 4B beads coupled with GST-PreScission and GST-Sec3N (1-268aa) and GST-Sec3N-AQA (1-268aa, L163A, R166Q, I171A). The inputs and pull-downs were analyzed by Western blot using anti-HA monoclonal antibody. The inputs of GST fusion proteins were stained with Ponceau S. Sec3N-AQA pulled down much less Syntainx4 than Sec3N. GST-PreScission serves as a negative control.

Previous studies have shown that Exo70 and Sec8 regulate the secretion of the gelatinases MMP-2 and MMP-9 in a human breast cancer cell (Liu et al., 2009a). I performed gelatin zymography assay using a human breast cancer cell line, MDA-MB-231. When GFP-Sec3N was overexpressed in these cells, MMP-2 and MMP-9 secretion was increased comparing to the overexpression of GFP alone (Figure 4.3A). Using lentiviral-based shRNA, I knocked down endogenous Sec3 in a human sarcoma cell line, HT1080 and found a reduction in MMP-2 and MMP-9 secretion, suggesting that Sec3 is required for MMP secretion (Figure 4.3B).

To visualize post-Golgi trafficking in Sec3 knockdown cells, VSV-G trafficking assay was performed as described previously (Liu et al., 2007). A temperature-sensitive VSV-G-GFP was expressed in HeLa cells and arrested in ER (at 40°C), arrested in Golgi (temperature shift to 20°C) or released for exocytosis (temperature shift to 32°C). The incorporation of VSV-G to the plasma membrane was monitored using an antibody against the extracellular domain of VSV-G without cell permeabilization. Knockdown of Sec3 led to accumulated VSV-G vesicles in post-Golgi puncta and reduced VSV-G incorporation to the plasma membrane shown in Figure 4.3C. In addition, depletion of Sec3 impaired transferrin trafficking to recycling endosomes but had no detectable effect on transferrin or epidermal growth factor (EGF) endocytosis (data not shown).

Efficient and stable knockdown of Sec3 and amisyn was difficult to achieve, thus hindering the further characterization of their roles in exocytosis using wild type and mutant proteins. Future studies will focus on alternative approaches for efficient

knockdown such as CRISPR/Cas9 systems (Cong et al., 2013; Qi et al., 2013). When Sec3 can be stably knocked down, Sec3 mutants and truncates will be introduced to test if the MMP secretion and VSV-G trafficking can be restored.

**Establishing assays to test SNARE-mediated fusion, SNARE assembly and Syntaxin self-interaction**

To test the effect of regulatory proteins on SNARE-mediated fusion, I first established a fusion assay. Syntaxin4/SNAP23 were reconstituted into synthetic vesicles containing 15% PS and and 85% PC while VAMP3 into synthetic vesicles with 15% PS, 82% PC plus 1.5% NBD-PE and 1.5% rhodamine-PE as previously described (Weber et al., 1998; Shen et al., 2007). Upon fusion of the vesicles, the FRET between NBD and rhodamine fluorophores will be decreased and the signal of NBD will be increased. As shown in Figure 4.4A, Syntaxin4/SNAP23 vesicles were fused to VAMP3 vesicles; in the presence of soluble VAMP (VAMP3ΔTM) which competed with VAMP3 on the vesicles to bind to Syntaxin4/SNAP23 vesicles, the fusion was inhibited.

The t- and v-SNAREs can form a heat-sensitive and SDS-resistant ternary complex (Flaumenhaft et al., 1999). I tested the effect of regulatory proteins on SNARE complex formation using a SDS-resistance assay where the VAMP3 was fluorescently labeled. The presence of fluorescent VAMP3 in high molecular weight species in unboiled samples indicated the formation of a ternary complex (Figure 4.4B). When Amisyn was added, the amount of VAMP3-containing ternary complex was reduced, suggesting that Amisyn competed with VAMP3 to bind t-SNAREs.

**Figure 4.2**

**A.**

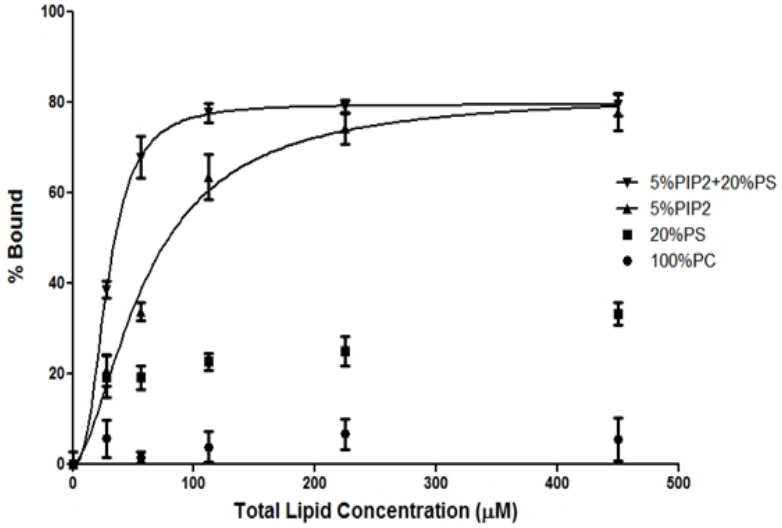


**B.**

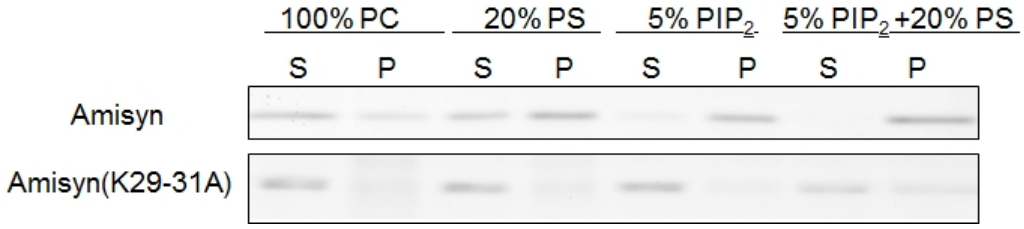


**C.**

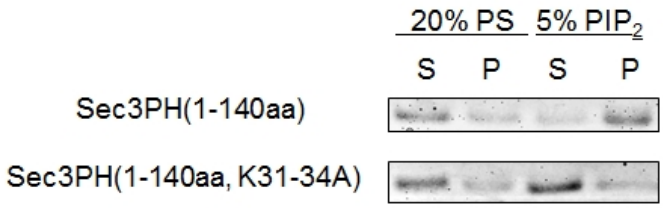

**Figure 4.2 Lipid binding of Amisyn and Sec3**

**(A)** Liposomes with 100-nm diameter were prepared by size extrusion. The percentages of phosphatidylserine (PS) and PI(4,5)$P_2$ ($PIP_2$) are the molar percentages of total lipids, with the remainder being phosphatidylcholine (PC). The binding of 500 nM Amisyn-$His_6$ to liposomes was determined by sedimentation assays conducted in 100 μl total volume in an ultracentrifuge TLA-100 rotor. Sucrose-loaded LUVs were precipitated at 150,000 g (62,000 rpm) for 30 min at 25°C. The supernatants and pellets were subjected to 15% SDS–PAGE and stained with SimplyBlue SafeStain for quantification of free and bound materials with ImageJ software. Each point was the average of three individual experiments. Error bars, SD. Binding curves were fitted with Prism 5.0 software (GraphPad) using 'one-site specific binding model with Hill slope'. Amisyn bound to 5% $PIP_2$ liposomes (kDa: 60.31 μM) and 5% $PIP_2$+20% PS liposomes (kDa: 28.67 μM). **(B)** The binding of 500nM Amisyn-$His_6$ and Amisyn(K29-31A)-$His_6$ to 100 μM liposomes was determined by sedimentation assays as described in (A). S: supernatants (unbound fraction), P: pellets (bound fraction). Amisyn(K29-31A) failed to bind 5% $PIP_2$ liposomes. **(C)** The binding of 300 nM GST-Sec3PH(1-140aa) and GST-Sec3PH(1-140aa, K31-34A) to 100 μM liposomes was determined by sedimentation assays as described in (A). Sec3PH(1-140aa) bound to 5% $PIP_2$ liposomes but not 20% PS liposomes; Sec3PH(1-140aa, K31-34A) failed to 5% $PIP_2$ liposomes. The basic residues in N-termini of Amisyn and Sec3 are required for and PI(4,5)$P_2$ binding.

**Figure 4.3**

**A.**

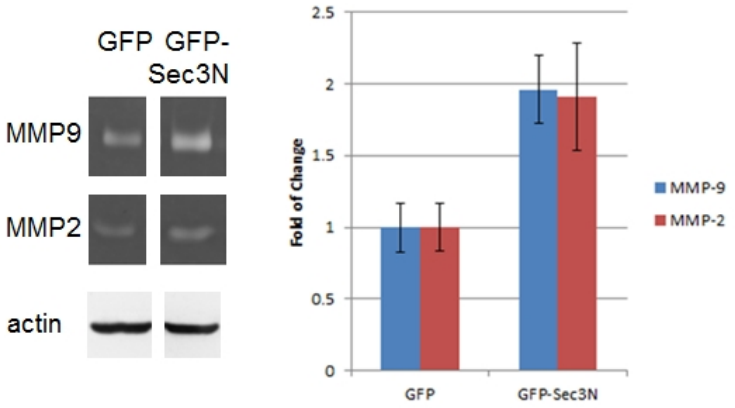


**B.**

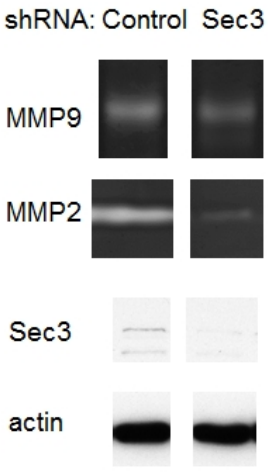


**C.**

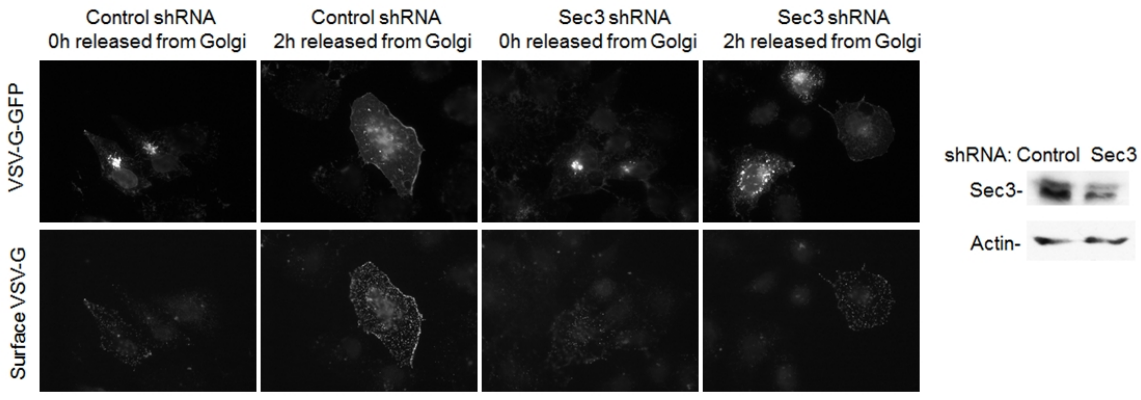

**Figure 4.3 Sec3 is required for MMPs secretion and VSV-G trafficking**

**(A)** Sec3 may regulate MMP2/9 secretion. MDA-MB-231 cells expressing GFP and GFP-Sec3N(1-268aa) were serum starved for 48 hours. Conditioned media were then collected and concentrated and subject to 8% SDS-PAGE containing 0.3% gelatin A. After in-gel digestion overnight, the gel was stained with Coomassie blue R-250 and analyzed with ImageJ software. The amount of secreted MMP2 or MMP9 was normalized to actin amount in total cell lysates. Right panel showed the fold of change of different treatments comparing to GFP. Overexpression of Sec3N increased the amount of secreted MMP2 and MMP9. **(B)** HT1080 sarcoma cells were transduced with lentiviruses expressing control or Sec3 shRNA. The cells were serum starved for 48 hours and conditioned media were collected and subject to gelatin zymography as described in (A). The efficiency of Sec3 knockdown was checked by Western blot. Knockdown of Sec3 led to reduction in secreted MMPs. **(C)** HeLa cells were transduced with lentiviruses expressing control or Sec3 shRNA then transfected with VSV-G-45ts-GFP mutant and incubated at 40°C. After overnight growth, the cells were moved to 20°C for 2 hours for Golgi arrest and then shifted to 32°C for 2 hours for post-Golgi trafficking in the presence of 100 μg/ml cycloheximide. The cells were then fixed and stained with the 8G5 monoclonal antibody against the extracellular domain of VSV-G. The efficiency of Sec3 knockdown was checked by Western blot. VSV-G post-Golgi trafficking to the plasma membrane and incorporation to the plasma membrane were impaired in Sec3 knockdown cells.

Syntaxin1A has a Habc domain and H3 domain (a.k.a SNARE domain, similar to Syntaxin4, Figure 4.1A), which can interact with each other, forming a closed conformation and result in auto-inhibition (Misura et al., 2000). Syntaxin4 has similar domain arrangements as Syntaxin1A (Misura et al., 2000); however, little is known aboutn how the auto-inhibition is released in order for Syntaxin4 to assemble into SNARE complex during membrane fusion. No protein has thus far been identified to directly induce the opening of the closed Syntaxin4.

I employed a bioluminescence resonance energy transfer (BRET) assay to monitor the intramolecular interaction within Syntaxin4. Syntaxin4 was tagged with NanoLuc at the N-terminus and HaloTag at the C-terminus and purified as a recombinant protein. NanoBret ligand was used for HaloTag as an energy acceptor. In the presence of the substrate furimazine, NanoLuc produces high intensity luminescence (maximal emission at 460nm). When the NanoBret ligand is in close proximity (< 10nm), it accepts the energy from luminescence and emits fluorescence (maximal emission at 620 nm).When N-terminus and C-terminus of Syntaxin4 bind to each other, BRET will occur. The BRET ratio of 460nm/620nm is shown in Figure 4.4C, and BRET was detected for NanoLuc-Syntaxin4-HaloTag, suggesting an intramolecular interaction. To validate that BRET did not occur between the NanoLuc tag and free NanoBret ligand in solution, I used NanoLuc-Syntaxin4 as a control and no BRET signal was detected. This assay can be later employed to test whether the addition of proteins of interest (e.g.., Sec3) can induce the opening of Syntaxin4 and reduce BRET ratio.

**Figure 4.4**

**A.**

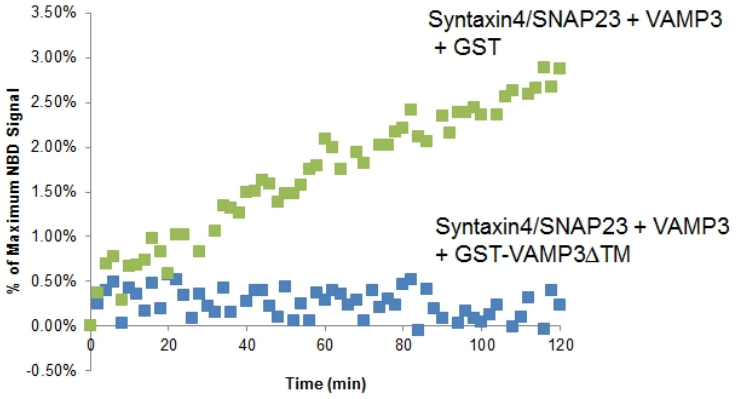


**B.**

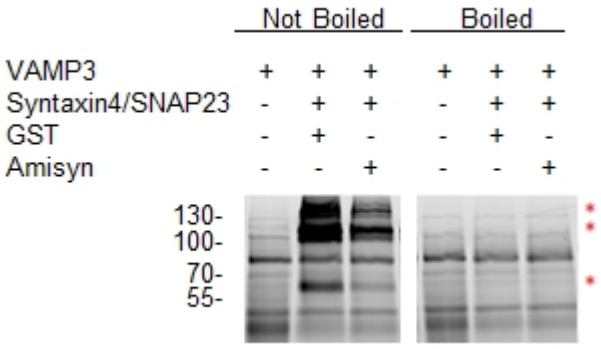


**C.**

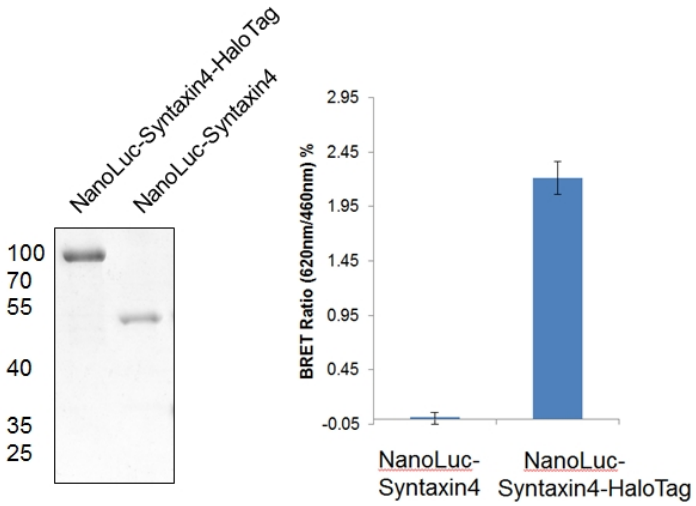

**Figure 4.4 Assays for SNARE activities**

**(A)** Liposome fusion assay were performed between t-vesicles containing Syntaxin4/SNAP23 and v-vesicles containing VAMP3 and NBD/rhodamine-labeled lipids at 37°C. The fluorescence of NBD was monitored for 2h until the reaction was stopped by addition of 2.5% Triton X-100 to reach the maximal fusion and allow for normalization. The increase of NBD signal over time indicates the fusion of t-vesicles and v-vesicles. Addition of GST-VAMP3ΔTM inhibited fusion. **(B)** Amisyn reduces the formation of ternary SNARE complex among syntaxin4, SNAP23 and VAMP3. Cytosolic domain of syntaxin4, VAMP3 (TAMRA labeled) and $His_6$-SNAP23 were incubated with GST or Amisyn-$His_6$ overnight; upon solubilization with SDS sample buffer, half of the samples were incubated at room temperature ("not boiled") while half at 95 °C ("boiled") for 5 min followed by SDS-PAGE and TAMRA signal scanning. Asterisks: SDS-resistant, heat sensitive and VAMP3-containing complexes. In the presence of Amisyn, the formation of ternary complex was reduced. **(C)** NanoLuc-Syntaxin4-HaloTag was purified from bacteria, and HaloTag was removed by TEV cleavage (left panel). 20nM NanoLuc-Syntaxin4-HaloTag and NanoLuc-Syntaxin4 were incubated with or without 100nM NanoBRET ligand. Then 10 μM furimazine substrate was quickly added to the protein and luminescence intensities at 460nm and 620nm were recorded. BRET ratio was calculated as $I_{620nm}/I_{460nm}$ (with NanoBRET ligand) - $I_{620nm}/I_{460nm}$ (without NanoBRET ligand). BRET was observed for NanoLuc-Syntaxin4-HaloTag not for NanoLuc-Syntaxin4.

## 4.3 DISCUSSION

Mammalian Sec3 can preferentially bind to t-SNARE on the basolateral plasma membrane. Similarly, yeast Sec3 binds to SSO1/2, the yeast homolog of Syntaxins on the plasma membrane; yeast Sec3 facilitates the binding of SSO1/2 to Sec9 and promotes fusion *in vitro* (Guo lab, unpublished data). However, the mammalian Sec3 seems to bind much weaker to Syntaxin4 comparing to their yeast counterparts, which may make it difficult to detect any effect of Sec3 on Syntaxin4 activities in the assays described in Figure 4.4. Additional activation of Sec3 may be required to enhance Syntaxin4 binding, such as binding to lipids and small GTPases, or phosphorylation by kinases. Since Sec3 binds $PI(4,5)P_2$, liposomes containing $PI(4,5)P_2$ can be included in the future test between Sec3 and Syntaxin4.

To test the role of Sec3 and amisyn in exocytosis, loss-of-function and rescue/complementation approaches were employed. However, siRNA or shRNA treatments did not yield efficient, homogenous and stable knockdown of Sec3 or amisyn. Future studies will focus on alternative approaches for efficient knockdown such as CRISPR/Cas9 systems (Cong et al., 2013; Qi et al., 2013). Once successful knockdown is achieved, MMPs secretion and VSV-G trafficking assays will be performed in the presence of wild type and mutant Sec3/amisyn proteins which fail to bind Syntaxin4 or lipids.

## 4.4 MATERIALS AND METHODS

### Plasmids and antibodies

mCherry-Syntaxin3ΔTM, mCherry-Syntaxin4ΔTM and Syntaxin4-HA were obtained from Dr. Michael Ehlers (Duke University). Syntaxin4-myc and Syntaxin4Δ1-29-myc were obtained from Dr. Thomas Weimbs (University of California, Santa Barbara). $His_6$-SNAP23 was obtained from Dr. Fabienne Paumet (Thomas Jefferson University). NanoLuc-Syntaxin4-HaloTag was obtained from Promega; $His_6$ tagged was added after HaloTag and a TEV protease cleavage site prior to HaloTag. Mouse Sec3 fragments and human amisyn were cloned in-frame into pEGFP-C1 for expression in cells. Mouse Sec3, human amisyn, human Syntaxin3, human Syntaxin4, rat VAMP3 full length and fragments were cloned in-frame into pGEX-4T-1, pGEX-6P-1 or pET21a vector for bacterial expression. The Sec3 mutant Sec3PH(140aa, K31-34A) and Sec3N-AQA (1-268aa, L163A, R166Q, I171A), Amisyn(K29-31A), VAMP3 (T66C, for labeling) were generated using the QuikChange site-directed mutagenesis kit (Stratagene). Mouse anti-actin mAb (MAB 1501, clone C4) was purchased from Chemicon, Millipore; mouse monoclonal anti-Hisx6 antibody (MMS-156R), monoclonal anti-HA antibody (16B12), monoclonal anti-myc antibody (9E10) from Covance; polyclonal anti-mCherry antibody (5993-100) from BioVision; polyclonal anti-Sec3 antibody (AP9562b) from Abgent. The 8G5 monoclonal antibody against the extracellular domain of VSV-G was a kind gift from Dr. Douglas Lyles (Wake Forest University).

**Protein purification**

GST fusion proteins were expressed in *E. coli* strain BL21-CodonPlus(DE3)-RP and purified using glutathione Sepharose 4B (GE Healthcare). GST fusion proteins were expressed in *E. coli* strain BL21-CodonPlus(DE3)-RP and purified using glutathione Sepharose 4B (GE Healthcare). GST fusion proteins were cleaved with PreScission protease to remove GST in 50 mM Tris-HCl, 150mM NaCl, 1mM EDTA, 1mM dithiothreitol (pH 7.0) overnight at 4°C; the resins were then washed with PBS containing 1mM DTT to elute the liberated recombinant proteins. His6-tagged proteins was purified from *E. coli* with TALON beads. TEV protease was used to remove HaloTag.

**Cell culture, transfection and transduction**

MDA-MB-231, 293T, HT1080 and HeLa cells were maintained at 37°C in DMEM (Invitrogen) supplemented with 10% FBS, 2 mmol/L l-glutamine, 100 U /ml penicillin, and 100 μg/ml streptomycin in a 5% CO2 incubator. DNA transfections into cells were carried out using Lipofectamine 2000 (Invitrogen). Sec3 shRNAs in pLKO.1 lentiviral vector, targeting both splice variants of human Sec3 were obtained from Open Biosystems. The shRNA targets nucleotides 1473-1493 (sense: 5'-CCTGTTGGATATGGGAAACAT-3', hairpin 1) of human Sec3 mRNA (NM_018261) and nucleotides 1244-1264 (sense: 5'-CCCGACTATATGAAAGAGAAA-3', hairpin 2) of human Sec3 mRNA (NM_018261). Third generation packaging systems (REV, RRE,

VSV-G and shRNA) were used for lentiviral packaging in 293T cells. Cells were transduced with the viruses for two days before selection with 1 μg/mL puromycin.

### *In vitro* binding assay

For *in vitro* binding assay, 293T cell lysates expressing Syntaxin variants or bacterial purified Syntaxin variants were incubated with GST fusion Sec3 variants conjugated to glutathione Sepharose 4B beads in binding buffer (50 mM Tris-HCl pH 8.0, 135 mM NaCl, 1mM EDTA, 1 mM $Va_3VO_4$, 0.5% Triton X-100). After overnight incubation at 4°C, beads were washed three times. The bound proteins were analyzed by SDS-PAGE or Western blotting.

### Liposome co-sedimentation assay

Sucrose-loaded LUVs were prepared by size extrusion. Various lipids were mixed at different molar ratios, dried with nitrogen stream, and suspended at a concentration of 2 mM in a buffer containing 12 mM HEPES, pH 7.0, and 176 mM sucrose. The mixed lipids were subjected to five cycles of freeze-thaw and a 1-min bath sonication before being passed through 100-nm filters using a mini-extruder. LUVs were dialyzed overnight in the buffer containing 20mM HEPES, pH 7.5, 150 mM NaCl, 1mM EGTA.500 nM Amisyn or 300nM Sec3PH and mutants were mixed with LUVs at indicated concentration and centrifuged at 62,000 rpm for 30 min at 25°C in a TLA-100 rotor. The supernatants and pellets were subjected to 10% SDS-PAGE for quantification

of bound and unbound materials. Binding curves were fitted with Prism 5.0 software (GraphPad) using 'one-site specific binding model with Hill slope'.

**Zymography**

The "in-gel" zymography was performed as previously described (Liu et al., 2009a). After treatments, cells were cultured in serum-free DMEM for 48 h. Conditioned media from MDA-MB-231 were concentrated 50 times by filtration on Microcon concentrators (Millipore). Samples were mixed with SDS loading buffer (10% SDS, 50% glycerol, 0.4 M Tris, pH 6.8, and 0.1% bromophenol blue) and separated on 8% polyacrylamide/0.3% gelatin gels. Gels were then washed in 2.5% Triton X-100, 30 min each time, and incubated in reaction buffer (50 mM Tris, pH 8.0, and 5 mM $CaCl_2$) at 37°C overnight. After the reaction, gels were stained with staining buffer (0.12% Coomassie blue R-250, 50% methanol, and 20% acetic acid) for 1 h and destained overnight with destaining buffer (22% methanol and 10% acetic acid). Gel loadings were normalized to total protein measured with a Bio-Rad Protein Assay (Richmond, CA).

**VSV-G trafficking assay**

VSV-G trafficking assay was performed as described previously (Liu et al., 2007; Ren and Guo, 2013). HeLa cells were transduced with Sec3 shRNA or non-targeting shRNA. After 48 hours of the shRNA treatment, HeLa cells were transfected with VSV-G-45ts-GFP mutant and and immediately placed at 40°C. After overnight growth, the cells were moved to 20°C for 2 hours for Golgi arrest and then shifted to 32°C for different times in

the presence of cycloheximide (100μg/ml). The cells were then fixed for GFP observation and immunofluorescence using the 8G5 mAb against the extracellular domain of VSV-G without cell permeabilization. Anti-mouse Alexa594 was used as secondary antibodies in these experiments. Images were obtained using Leica DMI 6000B inverted microscope equipped with a DFC350 FX camera and a 63x objective.

**Liposome fusion assay**

Purified Stx4/SNAP23 complexes were reconstituted into phospholipids composed of 85% phosphatidylcholine (PC) and 15% phosphatidylserine (PS) (t-vesicle). VAMP3 was reconstituted into phospholipids containing 82% PC and 15% PS plus 1.5% NBD-PE [N-(7-nitro-2,1,3-benzoxadiazole-4-yl)-phosphatidylethanolamine] and 1.5% rhodamine-PE (v-vesicle). Proteoliposomes were formed by dilution of the detergent n-octyl-β-D-glucoside (OG) below critical micelle concentration. OG was removed by dialysis and proteoliposomes were concentrated by Nycodenz gradient. The t-vesicle and v-vesicle were pre-incubated overnight at 4°C and shifted to 37°C for fusion reaction. NBD fluorescence intensity was monitored in a Molecular Device SpectraMax Gemini EM plate reader at the wavelength of 460nm/530nm (Ex/Em) for 2 hours until the reaction was stopped by addition of 2.5% Triton X-100 to reach the maximal fusion and allow for normalization.

**SDS-resistant assay**

VAMP3 (T66C) protein was labeled with TAMRA to Cys66. Cytosolic domain of syntaxin4, VAMP3 (TAMRA labeled) and SNAP23 were incubated with overnight at 4°C; upon solubilization with SDS sample buffer, half of the samples were incubated at room temperature for SDS-resistant heat-sensitive SNARE complex to form, while half were boiled at 95 °C for 5 min. Samples were subjected to SDS-PAGE and TAMRA signals were scanned in a Typhoon 9410 fluorescent scanner.

**BRET assay**

Intramolecular BRET between NanoLuc and HaloTag was tested. 20nM NanoLuc-Syntaxin4-HaloTag and NanoLuc-Syntaxin4 were incubated with or without 100nM NanoBRET ligand. 10 μM furimazine substrate was quickly added to the protein and luminescence intensities at 460nm and 620nm were recorded in a Molecular Device SpectraMax Gemini EM plate reader. BRET ratio was calculated as $I_{620nm}/I_{460nm}$ (with NanoBRET ligand) - $I_{620nm}/I_{460nm}$ (without NanoBRET ligand).

# CHAPTER 5 DISCUSSION AND FUTURE PERSPECTIVES

## 5.1 The molecular mechanism of Exo70 scaffolding the membrane

Lipid binding and protein oligomerization of Exo70 is required for curvature induction (Chapter 2). I speculated that Exo70 scaffolds membrane to generate curvature; however the molecular details of the scaffolding remain unclear. FRAP analyses of GFP-I-BAR proteins (Saarikangas et al., 2009) and GFP-Exo70 on filopodia showed that Exo70 had a bigger immobile population and a slower exchange rate than those of I-BAR of IRSp53 (data not shown). To obtain further information of Exo70 in the filopodia, I collaborated with Dr. Yujie Sun group at Peking University. We employed stochastic optical reconstruction microscopy (STORM) to analyze the distribution of Exo70 tagged with mEos3.2, a true monomeric fluorescent protein. We found that the number of Exo70 molecules in filopodia is three fold of that in cytoplasm (data not known), suggesting that Exo70 has an enhanced self-association in filopodia. A further analysis will reveal the distribution of Exo70 molecules or oligomers in filopodia in cells.

To determine the size of Exo70 oligomers, I will perform gradient centrifugation with purified proteins. The orientation and shape of Exo70 oligomers will be investigated with rotary-shadowing EM. The residues in N-terminal helix responsible for the oligomerization will be determined to further confirm the orientation of the oligomer.

In collaboration with Dr. Radhakrishnan group, we investigated the molecular mechanism of Exo70-induced membrane deformation by molecular dynamics and

mesoscale simulations using modeled membranes and vesicles (Chapter 2). Exo70 parallel and anti-parallel dimers induced tubules in the interior of the modeled vesicles, but not the Exo70(Δ1-75) monomer (Figure 2.11). However, Exo70(Δ1-75) was able to induce tubules in GUVs, albeit the number of tubules induced was significantly fewer than that of Exo70 (Figure 2.2). The difference of the ability of Exo70(Δ1-75) in inducing tubules between the simulation and experimental results could be explained as follows. In simulations, the modeled membrane and vesicles contained 20% PS and 80% PC while the GUV contained 5% $PI(4,5)P_2$, 15% PS and 80% PC. In the absence of $PI(4,5)P_2$ , the binding of Exo70(Δ1-75) to the membrane was reduced; therefore the effect of tubule induction in simulations might be weaker than the GUV experiment. In addition, the binding of Exo70 protein to $PI(4,5)P_2$ might re-orientate the protein-lipid and/or protein-protein interaction surface. We will include $PI(4,5)P_2$ in the modeled membrane and test the effect on Exo70-induced membrane curvature.

I will also investigate the effect of Exo70 oligomerization on $PI(4,5)P_2$ clustering. BAR and I-BAR have been shown to cluster $PI(4,5)P_2$ on synthetic liposomes (Saarikangas et al., 2009). It will be interesting to examine whether $PI(4,5)P_2$ is clustered on biological membrane, especially in filopodia where Exo70 shows enhanced clustering. The regulation of $PI(4,5)P_2$ distribution is of importance because certain $PI(4,5)P_2$ binding proteins will be recruited to the sites of $PI(4,5)P_2$ clusters and/or be activated to transmit signals to other proteins. Exo70 may regulate the activities of $PI(4,5)P_2$ binding proteins by clustering $PI(4,5)P_2$.

Using biochemical, biophysical and imaging approaches, I hope to better understand how Exo70 scaffolds the membrane and whether it can cluster $PI(4,5)P_2$, which may signaling to other proteins in filopdia.

**5.2 The functions of Exo70 in directional cell migration**

In cells, overexpression of Exo70 induced numerous filopodia, a substantial portion of which was actin-free; overexpression of Exo70 mutants, including lipid-binding deficient mutant Exo70(K571A/E572A), oligomerization deficient mutant Exo70(Δ1-75), Arp2/3-stimulation deficient mutant Exo70(Δ628-630), did not induce filopodia (Chapter 2, Figure 2.7). Exo70(Δ1-75) is a specific mutant for curvature induction because it does not affect other cellular events that Exo70 participates such as exocytosis and regulating the activity of the Arp2/3 complex (Figure 3.1-3); Exo70(Δ1-75) did not induce filopodia, suggesting that the excess amount of Exo70 exerts the ability to induce curvature independent of actin. Although Exo70(Δ628-630) mutant may not affect curvature induction, it did not stimulate Arp2/3-mediated actin polymerization and did not induce filopodia, suggesting that Arp2/3 activity also plays an important role in filopodia formation, consistent with previous studies (Korobova and Svitkina, 2008; Yang and Svitkina, 2011). In summary, both membrane dynamics and actin dynamics regulated by Exo70 are essential for filopodia formation.

The endogenous Exo70 exists in a free pool as well as being part of the exocyst holo-complex (Chapter 2, Figure 2.10). It is possible that the free pool of Exo70 exerts its function in membrane curvature induction during protrusion formation, independent of

the other exocyst components. According to the molecular weight standards, the free pool of Exo70 may not be monomeric Exo70. Further investigation will be carried out to determine whether this free pool is oligomeric Exo70 or Exo70 associated with other proteins.

By several migration assays, I observed that Exo70 not only affected the rate of migration but also the directional persistence (Chapter 3). Knockdown of Exo70 slowed down the rate of cells passing through filter membranes in transwell assay and the rate of wound closure in wound healing assay, which could not be restored by expressing Exo70 mutants; when looking at the migratory trajectories of individual cells, I found that during migration the Exo70 RNAi cells expressing Exo70 mutants made more turns at the front than the cells expressing Exo70 wild type (Figure 3.5). These results suggest integral Exo70 is required for effective and efficient directional migration. The membrane dynamics and actin dynamics at the leading edge are important for motility as well as the establishment and maintenance of the front-rear polarity.

Exo70 plays multiple roles at the leading edge during cell migration. The ability of Exo70 to induce negative membrane curvature may create a space at the leading edge to accommodate active actin polymerization and branching mediated by the Arp2/3 complex. Exo70 may thus couple membrane remodeling and actin dynamics for effective protrusion formation and cell migration. As the plasma membrane and actin network at the leading edge moving forward, Exo70 may assemble into the exocyst complex and

regulate the trafficking of integrins to the basal membrane at the front (Thapa et al., 2012).

### 5.3 The functions of Exo70 in other cellular processes

Exo70 regulates both actin dynamics and membrane dynamics at the leading edge during directional cell migration (Chapter 3). Exo70 may also play a role in other cellular processes such as primary ciliogenesis, tunneling nanotubes (TNTs) formation, and vesicular-tubular carrier formation.

The exocyst is shown to regulate primary ciliogenesis (Das and Guo, 2011; Feng et al., 2012) and Exo70 also localizes to the basal body and along the length of the primary cilia (Guo lab, unpublished data), which is a microtubule-based membrane protrusion with high negative membrane curvature. It will be interesting to investigate if the membrane-deforming activity of Exo70 in involved for generation or maintenance of primary cilia using Exo70 mutant specific defective in curvature induction.

Tunneling nanotubes (TNTs) are actin-based membrane connections between distant cells mediating intercellular transfer of cargos like calcium, vesicles, and viruses (Zhao and Guo, 2009). The exocyst has been implicated in the formation of TNTs (Hase et al., 2009). Similar to filopodia, TNTs also have high negative membrane curvature. It is likely that Exo70 plays a role in initiating TNTs as it induces filopodia; moreover, vesicles are transported along TNTs and Exo70 may mediate vesicle targeting as well.

Using various Exo70 mutants which affect membrane curvature, Arp2/3 activity, or exocytosis, the roles of Exo70 in the formation of TNTs can be tested.

In addition to the plasma membrane localization, Exo70 localizes to internal membrane compartments including endosomes (Oztan et al., 2007). Arp2/3-mediated actin polymerization is required for the generation of vesicular or tubular carriers in multiple vesicle trafficking pathways, depending on the nucleation-promoting factors (NPFs) (Campellone and Welch, 2010). Exo70 can kinetically stimulate Arp2/3 complex in actin polymerization in the presence of different NPFs (Liu et al., 2012; Guo lab, unpublished data). Therefore, Exo70 is likely to cooperate with NPFs on endosomes such as WASH (Park et al., 2013) and regulate vesicular or tubular carriers formation for exocytosis or other routes. In vitro actin polymerization assays will be carried out with actin, Arp2/3 complex and WASH, in the presence or absence of Exo70 to test if Exo70 can enhance Arp2/3-mediated actin assembly. If this is the case, Exo70 mutants will be employed to test whether tubular carriers can be formed from endosomes when the Exo70-Arp2/3 interaction or Exo70-induced curvature is impaired.

### 5.4 The regulation of SNARE complex by the exocyst

Tethering complexes can directly regulate the activities of SNARE complexes (Starai et al., 2008; Stroupe et al., 2009; Ren et al., 2009). Sec3 interacts with Syntaxin4, a t-SNARE resident on the plasma membrane (Chapter 4), providing a possibility that the exocyst can open up t-SNARE for SNARE assembly and membrane fusion. Future work will focus on the binding mode of Sec3 to Syntaxin4, in comparison with

Munc18/Syntaxin interactions (Jahn and Scheller, 2006; Rizo and Südhof, 2012). A minimal exocyst such as Sec3/Sec5/Sec8/Exo84 will also be investigated for efficient tethering of vesicles to the target membrane for fusion.

In summary, my dissertation investigated different components of the exocyst complex and their roles in various cellular processes. The complexity makes the exocyst a center for signaling integration and processing to ensure the tight temporal and spatial regulation of multiple pathways in cells.

## REFERENCES


Agrawal, N.J., Nukpezah, J., and Radhakrishnan, R. (2010). Minimal mesoscale model for protein-mediated vesiculation in clathrin-dependent endocytosis. PLoS Comput. Biol. *6*, e1000926.

Andersen, N.J., and Yeaman, C. (2010). Sec3-containing exocyst complex is required for desmosome assembly in mammalian epithelial cells. Mol. Biol. Cell *21*, 152-164.

Angelova, M.I., and Dimitrov, D.S. (1986). Liposome electroformation. Faraday Discuss. Chem. Soc. *81*, 303-311.

Arkhipov, A., Yin, Y., and Schulten, K. (2008). Four-scale description of membrane sculpting by BAR domains. Biophys. J. *95*, 2806-2821.

Ayton, G.S., and Voth, G.A. (2009). Systematic multiscale simulation of membrane protein systems. Curr. Opin. Struct. Biol. *19*, 138 – 144.

Baek, K., Knödler, A., Lee, S.H., Zhang, X., Orlando, K., Zhang, J., Foskett, T.J., Guo, W., and Dominguez, R. (2010). Structure-function study of the N-terminal domain of exocyst subunit Sec3. J. Biol. Chem. *285*, 10424-10433.

Bao, Y., Lopez, J.A., James, D.E., and Hunziker, W. (2008). Snapin interacts with the Exo70 subunit of the exocyst and modulates GLUT4 trafficking. J. Biol. Chem. *283*, 324-331.

Baumgart, T., Capraro, B.R., Zhu, C., and Das, S.L. (2011). Thermodynamics and mechanics of membrane curvature generation and sensing by proteins and lipids. Annu Rev Phys Chem. *62*, 483-506.

Bereiter-Hahn, J. (2005). Mechanics of crawling cells. Med. Eng. Phys. *27*, 743–753.

Bjelkmar, P., Larsson, P., Cuendet, M.A., Hess, B., and Lindahl, E. (2010). Implementation of the CHARMM force field in GROMACS: Analysis of protein stability effects from correction maps, virtual interaction sites, and water models. J. Chem. Theory Comput. *6*, 459-466.

Boucrot, E., Pick, A., Çamdere, G., Liska, N., Evergren, E., McMahon, H.T., and Kozlov, M.M. (2012). Cell membrane fission is promoted by insertion of amphipathic helices and is restricted by crescent BAR domains. Cell *149*, 124-136.

Bodemann, B.O., Orvedahl, A., Cheng, T., Ram, R.R., Ou, Y.H., Formstecher, E., Maiti, M., Hazelett, C.C., Wauson, E.M., Balakireva, M., Camonis, J.H., Yeaman, C., Levine, B., and White, M.A. (2011). RalB and the exocyst mediate the cellular starvation response by direct activation of autophagosome assembly. Cell *144*, 253–267.

Bryant, D.M., Datta, A., Rodríguez-Fraticelli, A.E., Peränen, J., Martín-Belmonte, F., and Mostov, K.E. (2010). A molecular network for de novo generation of the apical surface and lumen. Nat. Cell Biol. *12*, 1035-1045.

Cai, H., Reinisch, K., and Ferro-Novick, S. (2007). Coats, tethers, Rabs, and SNAREs

work together to mediate the intracellular destination of a transport vesicle. Dev. Cell *12*, 671-682.

Campellone, K.G., and Welch, M.D. (2010). A nucleator arms race: cellular control of actin assembly. Nat Rev Mol Cell Biol. *11*, 237-251.

Castermans, D., Thienpont, B., Volders, K., Crepel, A., Vermeesch, J.R., Schrander-Stumpel, C.T., Van de Ven, W.J., Steyaert, J.G., Creemers, J.W., and Devriendt, K. (2008). Position effect leading to haploinsufficiency in a mosaic ring chromosome 14 in a boy with autism. Eur. J. Hum. Genet. *16*, 1187-1192.

Castermans, D., Volders, K., Crepel, A., Backx, L., De Vos, R., Freson, K., Meulemans, S., Vermeesch, J.R., Schrander-Stumpel, C.T., De Rijk, P., Del-Favero, J., Van Geet, C., Van De Ven, W.J., Steyaert, J.G., Devriendt, K., and Creemers, J.W. (2010). SCAMP5, NBEA and AMISYN: three candidate genes for autism involved in secretion of large dense-core vesicles. Hum. Mol. Genet. *19*, 1368-1378.

Cavanaugh, L.F., Chen, X., Richardson, B.C., Ungar, D., Pelczer, I., Rizo, J., and Hughson, F.M. (2007). Structural analysis of conserved oligomeric Golgi complex subunit 2. J Biol Chem *282*, 23418-23426.

Cong, L., Ran, F.A., Cox, D., Lin, S., Barretto, R., Habib, N., Hsu, P.D., Wu, X., Jiang, W., Marraffini, L.A., and Zhang, F. (2013). Multiplex genome engineering using CRISPR/Cas systems. Science *339*, 819-823.

Constable, J.R., Graham, M.E., Morgan, A., and Burgoyne, R.D. (2005). Amisyn regulates exocytosis and fusion pore stability by both syntaxin-dependent and syntaxin-independent mechanisms. J. Biol. Chem. *280*, 31615-31623.

Croteau, N.J., Furgason, M.L., Devos, D., and Munson, M. (2009). Conservation of helical bundle structure between the exocyst subunits. PLoS One *4*, e4443.

Das, A., and Guo, W. (2011). Rabs and the exocyst in ciliogenesis, tubulogenesis and beyond. Trends Cell Biol. *21*,383–386.

Doherty, G.J., and McMahon, H.T. (2008). Mediation, modulation, and consequences of membrane-cytoskeleton interactions. Annu. Rev. Biophys. *37*, 65-95.

Dong, G., Hutagalung, A.H., Fu, C., Novick, P., and Reinisch, K.M. (2005). The structures of exocyst subunit Exo70p and the Exo84p C-terminal domains reveal a common motif. Nat. Struct. Mol. Biol. *12*, 1094-1100.

Esposito, G., Ana Clara, F., and Verstreken, P. (2012). Synaptic vesicle trafficking and Parkinson's disease. Dev. Neurobiol. *72*, 134-144.

Farsad, K., Ringstad, N., Takei, K., Floyd, S.R., Rose, K., and De Camilli, P. (2001). Generation of high curvature membranes mediated by direct endophilin bilayer interactions. J. Cell Biol. *155*, 193-200.

Feng, S., Knödler, A., Ren, J., Zhang, J., Zhang, X., Hong, Y., Huang, S., Peränen, J., and

Guo, W. (2012). A Rab8 guanine nucleotide exchange factor-effector interaction network regulates primary ciliogenesis. J. Biol. Chem. *287*, 15602-15609.

Fernandez, S.V., Snider, K.E., Wu, Y.Z., Russo, I.H., Plass, C., and Russo, J. (2010). DNA methylation changes in a human cell model of breast cancer progression. Mutat. Res. *688*, 28-35.

Flaumenhaft, R., Croce, K., Chen, E., Furie, B., and Furie, B.C. (1999). Proteins of the exocytotic core complex mediate platelet alpha-granule secretion. Roles of vesicle-associated membrane protein, SNAP-23, and syntaxin 4. J. Biol. Chem. *274*, 2492-2501.

Ford, M.G., Mills, I.G., Peter, B.J., Vallis, Y., Praefcke, G.J., Evans, P.R., and McMahon, H.T. (2002). Curvature of clathrin-coated pits driven by Epsin. Nature *419*, 361–366.

Frost, A., Perera, R., Roux, A., Spasov, K., Destaing, O., Egelman, E.H., De Camilli, P., and Unger, V.M. (2008). Structural basis of membrane invagination by F-BAR domains. Cell *132*, 807-817.

Frost, A., Unger, V.M., and De Camilli, P. (2009). The BAR Domain Superfamily: Membrane-Molding Macromolecules. Cell *137*, 191-196.

Gerges, N.Z., Backos, D.S., Rupasinghe, C.N., Spaller, M.R., and Esteban, J.A. (2006). Dual role of the exocyst in AMPA receptor targeting and insertion into the postsynaptic membrane. EMBO J. *25*, 1623-1634.

Goley, E.D., and Welch, M.D. (2006). The ARP2/3 complex: an actin nucleator comes of age. Nat. Rev. Mol. Cell Biol. *7*, 713–726.

Grindstaff, K.K., Yeaman, C., Anandasabapathy, N., Hsu, S.C., Rodriguez-Boulan, E., Scheller, R.H., and Nelson, W.J. (1998). Sec6/8 complex is recruited to cell-cell contacts and specifies transport vesicle delivery to the basal-lateral membrane in epithelial cells. Cell *93*, 731-740.

Gromley, A., Yeaman, C., Rosa, J., Redick, S., Chen, C.T., Mirabelle, S., Guha, M., Sillibourne, J., and Doxsey, S.J. (2005). Centriolin anchoring of exocyst and SNARE complexes at the midbody is required for secretory-vesicle-mediated abscission. Cell *123*, 75–87.

Grote, E., Carr, C.M., and Novick, P.J. (2000). Ordering the final events in yeast exocytosis. J. Cell Biol. *151*, 439-452.

Guan, R., Dai, H., and Rizo, J. (2008). Binding of the Munc13-1 MUN domain to membrane-anchored SNARE complexes. Biochemistry *47*, 1474-1481.

Guerrier, S., Coutinho-Budd, J., Sassa, T., Gresset, A., Jordan, N.V., Chen, K., Jin, W.L., Frost, A., and Polleux, F. (2009). The F-BAR domain of srGAP2 induces membrane protrusions required for neuronal migration and morphogenesis. Cell *138*, 990-1004.

Hase, K., Kimura, S., Takatsu, H., Ohmae, M., Kawano, S., Kitamura, H., Ito, M., Watarai, H., Hazelett, C.C., Yeaman, C., and Ohno, H. (2009). M-Sec promotes

membrane nanotube formation by interacting with Ral and the exocyst complex. Nat. Cell Biol. *11*, 1427-1432.

Hattendorf, D.A., Andreeva, A., Gangar, A., Brennwald, P.J., and Weis, W.I. (2007). Structure of the yeast polarity protein Sro7 reveals a SNARE regulatory mechanism. Nature *446*, 567-571.

Hamburger, Z.A., Hamburger, A.E., West, A.P., Jr., and Weis, W.I. (2006). Crystal structure of the S.cerevisiae exocyst component Exo70p. J. Mol. Biol. *356*, 9-21.

He, B., Xi, F., Zhang, X., Zhang, J., and Guo, W. (2007). Exo70 interacts with phospholipids and mediates the targeting of the exocyst to the plasma membrane. EMBO J. *26*, 4053-4065.

He, B., and Guo, W. (2009). The exocyst complex in polarized exocytosis. Curr. Opin. Cell Biol. *21*, 537-542.

Heider, M.R., and Munson, M. (2012). Exorcising the exocyst complex. Traffic. *13*, 898-907.

Hinshaw, J.E., and Schmid, S.L. (1995). Dynamin self-assembles into rings suggesting a mechanism for coated vesicle budding. Nature *374*, 190-192.

Hsu, S.C., TerBush, D., Abraham, M, and Guo, W. (2004). The exocyst complex in polarized exocytosis. Inter. Rev. Cytology. *233*, 243-265.

Hu, S.H., Latham, C.F., Gee, C.L., James, D.E., and Martin, J.L. (2007). Structure of the Munc18c/Syntaxin4 N-peptide complex defines universal features of the N-peptide binding mode of Sec1/Munc18 proteins. Proc. Natl. Acad. Sci. USA. *104*, 8773-8778.

Hui, E., Johnson, C.P., Yao, J., Dunning, F.M., and Chapman, E.R. (2009). Synaptotagmin-mediated bending of the target membrane is a critical step in $Ca(^{2+})$-regulated fusion. Cell *138*, 709-721.

Humphrey, W., Dalke, A., and Schulten, K. (1996). VMD: Visual molecular dynamics. J. Mol. Graph. *14*, 33 – 38.

Inoue, M., Chang, L., Hwang, J., Chiang, S. H., and Saltiel, A. R. (2003). The exocyst complex is required for targeting of Glut4 to the plasma membrane by insulin. Nature *422*, 629-633.

Jahn, R., and Scheller, R.H. (2006). SNAREs--engines for membrane fusion. Nat. Rev. Mol. Cell Biol. 7, 631-643.

James, D.J., Khodthong, C., Kowalchyk, J.A., and Martin, T.F. (2008). Phosphatidylinositol 4,5-bisphosphate regulates SNARE-dependent membrane fusion. J. Cell Biol. 182, 355-366.

Ji, L., Lim, J., and Danuser, G. (2008). Fluctuations of intracellular forces during cell protrusion. Nat. Cell Biol. *10*, 1393-1400.

Korobova, F., and Svitkina, T. (2008). Arp2/3 complex is important for filopodia formation, growth cone motility, and neuritogenesis in neuronal cells. Mol. Biol. Cell. *19*, 1561-1574.

Lai, C.L., Jao, C.C., Lyman, E., Gallop, J.L., Peter, B.J., McMahon, H.T., Langen, R., Voth, G.A. (2012). Membrane binding and self-association of the epsin N-terminal homology domain. J. Mol. Biol. *423*, 800-817.

Lee, S.H., Kerff, F., Chereau, D., Ferron, F., Klug, A., and Dominguez, R. (2007). Structural basis for the actin-binding function of missing-in-metastasis. Structure *15*, 145-155.

Leto, D., and Saltiel, A.R. (2012). Regulation of glucose transport by insulin: traffic control of GLUT4. Nat. Rev. Mol. Cell Biol. *13*, 383-396.

Li, W., Ma, C., Guan, R., Xu, Y., Tomchick, D.R., and Rizo, J. (2011). The crystal structure of a Munc13 C-terminal module exhibits a remarkable similarity to vesicle tethering factors. Structure *19*, 1443-1455.

Liu, J., Kaksonen, M., Drubin, D.G., and Oster, G. (2006). Endocytic vesicle scission by lipid phase boundary forces. Proc. Natl. Acad. Sci. USA *103*, 10277-10282.

Liu, J., Zuo, X., Yue, P., and Guo, W. (2007). Phosphatidylinositol 4,5-bisphosphate mediates the targeting of the exocyst to the plasma membrane for exocytosis in

mammalian cells. Mol. Biol. Cell *18*, 4483-4492.

Liu, J., Yue, P., Artym, V.V., Mueller, S.C., and Guo, W. (2009). The role of the exocyst in matrix metalloproteinase secretion and actin dynamics during tumor cell invadopodia formation. Mol. Biol. Cell *20*, 3763-3771.

Liu, J., Sun, Y., Drubin, D.G., and Oster, G.F. (2009). The Mechanochemistry of Endocytosis. PLoS Biol. *7*, e1000204.

Liu, J., Zhao, Y., Sun, Y., He, B., Yang, C., Svitkina, T., Goldman, Y.E., and Guo, W. (2012). Exo70 Stimulates the Arp2/3 Complex for Lamellipodia Formation and Directional Cell Migration. Curr. Biol. *22*, 1510-1515.

Low, S.H., Chapin, S.J., Weimbs, T., Kömüves, L.G., Bennett, M.K., and Mostov, K.E. (1996). Differential localization of syntaxin isoforms in polarized Madin-Darby canine kidney cells. Mol Biol Cell. *7*, 2007-2018.

Lupas, A., Van Dyke, M., and Stock, J. (1991). Predicting coiled coils from protein sequences. Science *252*, 1162-1164.

Ma, C., Su, L., Seven, A.B., Xu, Y., and Rizo, J. (2013). Reconstitution of the vital functions of Munc18 and Munc13 in neurotransmitter release. Science *339*, 421-425.

Martens, S., and McMahon, H.T. (2008). Mechanisms of membrane fusion: disparate players and common principles. Nat. Rev. Mol. Cell Biol. *9*, 543-556.

Mathivet, L., Cribier, S., and Devaux, P.F. (1996). Shape change and physical properties

of giant phospholipid vesicles prepared in the presence of an AC electric field. Biophys. J. *70*, 1112-1121.

Mattila, P.K., Pykalainen, A., Saarikangas, J., Paavilainen, V.O., Vihinen, H., Jokitalo, E., and Lappalainen, P. (2007). Missing-in-metastasis and IRSp53 deform PI(4,5)P2-rich membranes by an inverse BAR domain-like mechanism. J. Cell Biol. *176*, 953-964.

Mattila, P.K., and Lappalainen, P. (2008). Filopodia: molecular architecture and cellular functions. Nat. Rev. Mol. Cell Biol. *9*, 446-454.

McLaughlin, S., and Murray, D. (2005). Plasma membrane phosphoinositide organization by protein electrostatics. Nature *438*, 605-611.

McMahon, H.T., and Gallop, J.L. (2005). Membrane curvature and mechanisms of dynamic cell membrane remodelling. Nature *438*, 590-596.

Mim, C., Cui, H., Gawronski-Salerno, J.A., Frost, A., Lyman, E., Voth, G.A., Unger, V.M. (2012). Cell Structural Basis of Membrane Bending by the N-BAR Protein Endophilin. Cell *149*, 137-145.

Misura, K.M., Scheller, R.H., and Weis, W.I. (2000). Three-dimensional structure of the neuronal-Sec1-syntaxin 1a complex. Nature *404*, 355-362.

Monticelli, L., Kandasamy, S.K., Periole, X., Larson, R.G., Tieleman, D.P., and Marrink, S.J. (2008). The MARTINI coarse-grained force field: Extension to proteins. J. Chem. Theory Comput. *4*, 819-834.

Moore, B.A., Robinson, H.H., and Xu, Z. (2007). The crystal structure of mouse Exo70 reveals unique features of the mammalian exocyst. J. Mol. Biol. *371*, 410-421

Munson, M., and Novick, P. (2006). The exocyst defrocked, a framework of rods revealed. Nat. Struct. Mol. Biol. *13*, 577-581.

Nachury, M.V., Seeley, E.S., and Jin, H. (2010). Trafficking to the ciliary membrane: how to get across the periciliary diffusion barrier? Annu. Rev. Cell Dev. Biol. *26*, 59-87.

Nichols, C.D., and Casanova, J.E. (2010). Salmonella-directed recruitment of new membrane to invasion foci via the host exocyst complex. Curr. Biol. *20*, 1316-1320.

Novick, P., and Guo, W. (2002). Ras family therapy: Rab, Rho and Ral talk to the exocyst. Trends Cell Biol. *12*, 247-249.

Ohya, T., Miaczynska, M., Coskun, U., Lommer, B., Runge, A., Drechsel, D., Kalaidzidis, Y., and Zerial, M. (2009). Reconstitution of Rab- and SNARE-dependent membrane fusion by synthetic endosomes. Nature *459*, 1091-1097.

Oztan, A., Silvis, M., Weisz, O.A., Bradbury, N.A., Hsu, S.C., Goldenring, J.R., Yeaman, C., and Apodaca, G. (2007). Exocyst requirement for endocytic traffic directed toward

the apical and basolateral poles of polarized MDCK cells. Mol. Biol. Cell *18*, 3978-3992.

Park, L., Thomason, P.A., Zech, T., King, J.S., Veltman, D.M., Carnell, M., Ura, S., Machesky, L.M., and Insall, R.H. (2013). Cyclical action of the WASH complex: FAM21 and capping protein drive WASH recycling, not initial recruitment. Dev. Cell. *24*, 169-181.

Pashkova, N., Jin, Y., Ramaswamy, S., and Weisman, L.S. (2006). Structural basis for myosin V discrimination between distinct cargoes. EMBO J. *25*, 693–700.

Pei, J., Ma, C., Rizo, J., and Grishin, N.V. (2009). Remote homology between Munc13 MUN domain and vesicle tethering complexes. J. Mol. Biol. *391*, 509-517.

Peter, B.J., Kent, H.M., Mills, I.G., Vallis, Y., Butler, P.J., Evans, P.R., and McMahon, H.T. (2004). BAR domains as sensors of membrane curvature: the amphiphysin BAR structure. Science *303*, 495-499.

Pérez-Victoria, F.J., Abascal-Palacios, G., Tascón, I., Kajava, A., Magadán, J.G., Pioro, E.P., Bonifacino, J.S., and Hierro, A. (2010). Structural basis for the wobbler mouse neurodegenerative disorder caused by mutation in the Vps54 subunit of the GARP complex. Proc. Natl. Acad. Sci. USA. *107*, 12860-12865.

Qi, L.S., Larson, M.H., Gilbert, L.A., Doudna, J.A., Weissman, J.S., Arkin, A.P., and Lim, W.A. (2013). Repurposing CRISPR as an RNA-guided platform for sequence-

specific control of gene expression. Cell *152*, 1173-1183.

Pollard, T.D., and Borisy, G.G. (2003). Cellular motility driven by assembly and disassembly of actin filaments. Cell 112, 453-465.

Ramakrishnan, N., Sunil Kumar, P.B., and Ipsen, J.H. (2010). Monte Carlo simulations of fluid vesicles with in-plane orientational ordering. Phys. Rev. E. Stat. Nonlin. Soft Matter Phys. *81*, 041922.

Ramakrishnan, N., Ipsen, J.H., Sunil Kumar, P.B. (2012). Role of disclinations in determining the morphology of deformable fluid interfaces. Soft Matter *8*, 3058–3061.

Ramakrishnan, N., Kumar, P. B. S., Ipsen, J. H. (2013) Curvature mediated oligomerization of curvature inducing nematogens and membrane tubulation, Biophysical Journal *104*, 1-11.

Ren, Y., Yip, C.K., Tripathi, A., Huie, D., Jeffrey, P.D., Walz, T., and Hughson, F.M. (2009). A structure-based mechanism for vesicle capture by the multisubunit tethering complex Dsl1. Cell *139*, 1119-1129.

Ren, J., and Guo, W. (2012). ERK1/2 Regulate exocytosis through direct phosphorylation of the exocyst component Exo70. Dev. Cell *22*, 967-978.

Richardson, B.C., Smith, R.D., Ungar, D., Nakamura, A., Jeffrey, P.D., Lupashin, V.V., and Hughson, F.M. (2009). Structural basis for a human glycosylation disorder caused by mutation of the COG4 gene. Proc. Natl. Acad. Sci. USA. *106*, 13329–13334.

Ridley, A.J. (2011). Life at the leading edge. Cell *145*, 1012-1022.

Rizo J, and Südhof TC. (2012). The membrane fusion enigma: SNAREs, Sec1/Munc18 proteins, and their accomplices--guilty as charged? Annu. Rev. Cell Dev. Biol. 28, 279-308.

Rosse, C., Hatzoglou, A., Parrini, M.C., White, M.A., Chavrier, P., and Camonis, J. (2006). RalB mobilizes the exocyst to drive cell migration. Mol. Cell Biol. *26*, 727-734.

Saarikangas, J., Zhao, H., Pykäläinen, A., Laurinmäki, P., Mattila, P.K., Kinnunen, P.K., Butcher, S.J., and Lappalainen, P. (2009). Molecular mechanisms of membrane deformation by I-BAR domain proteins. Curr. Biol. 19, 95-107.

Sali, A., and Blundell, T.L. (1993). Comparative protein modelling by satisfaction of spatial restraints. J. Mol. Biol. *234*, 779 – 815.

Sakurai-Yageta, M., Recchi, C., Le Dez, G., Sibarita, J.B., Daviet, L., Camonis, J., D'Souza-Schorey, C., and Chavrier, P. (2008). The interaction of IQGAP1 with the exocyst complex is required for tumor cell invasion downstream of Cdc42 and RhoA. J. Cell Biol. *181*, 985-998.

Scales, S.J., Hesser, B.A., Masuda, E.S., and Scheller, R.H. (2002). Amisyn, a novel syntaxin-binding protein that may regulate SNARE complex assembly. J. Biol. Chem. *277*, 28271-28279.

Scita, G., Confalonieri, S., Lappalainen, P., and Suetsugu, S. (2008). IRSp53: crossing the road of membrane and actin dynamics in the formation of membrane protrusions. Trends Cell Biol. *18*, 52-60.

Scott, B.L., Van Komen, J.S., Irshad, H., Liu, S., Wilson, K.A., and McNew, J.A. (2004). Sec1p directly stimulates SNARE-mediated membrane fusion in vitro. J. Cell Biol. *167*, 75-85.

Shen, J., Tareste, D.C., Paumet, F., Rothman, J.E., and Melia, T.J. (2007). Selective activation of cognate SNAREpins by Sec1/Munc18 proteins. Cell *128*, 183-195.

Sivaram, M.V., Saporita, J.A., Furgason, M.L., Boettcher, A.J., and Munson, M. (2005). Dimerization of the exocyst protein Sec6p and its interaction with the t-SNARE Sec9p. Biochemistry *44*, 6302-6311.

Spang, A. (2012). The DSL1 complex: the smallest but not the least CATCHR. Traffic *13*, 908-913.

Spiczka, K.S., and Yeaman, C. (2008). Ral-regulated interaction between Sec5 and paxillin targets Exocyst to focal complexes during cell migration. J. Cell Sci. *121*, 2880-2891.

Stachowiak, J.C., Hayden, C.C., and Sasaki, D.Y. (2010). Steric confinement of proteins on lipid membranes can drive curvature and tubulation. Proc. Natl. Acad. Sci. USA. *107*, 7781-7786.

Starai, V.J., Hickey, C.M., and Wickner, W. (2008). HOPS proofreads the trans-SNARE complex for yeast vacuole fusion. Mol. Biol. Cell *19*, 2500-2508.

Stroupe, C., Hickey, C.M., Mima, J., Burfeind, A.S., and Wickner, W. (2009). Minimal membrane docking requirements revealed by reconstitution of Rab GTPase-dependent membrane fusion from purified components. Proc. Natl. Acad. Sci. USA *106*, 17626-17633.

Suetsugu, S. Murayama, K., Sakamoto, A., Hanawa-Suetsugu, K., Seto, A., Oikawa, T., Mishima, C., Shirouzu, M., Takenawa, T., and Yokoyama, S. (2006). The RAC binding domain/IRSp53-MIM homology domain of IRSp53 induces RAC-dependent membrane deformation. J. Biol. Chem. *281*, 35347-35358.

Svitkina, T.M., and G.G. Borisy. (1999). Arp2/3 complex and actin depolymerizing factor/cofilin in dendritic organization and treadmilling of actin filament array in lamellipodia. J Cell Biol. *145*, 1009-1026.

Svitkina, T.M., and Borisy, G.G. (2006). Correlative light and electron microscopy studies of cytoskeletal dynamics. Cell Biology: A Laboratory Handbook, 3rd Edition, 277–285.

Svitkina, T.M. (2007). Electron microscopic analysis of the leading edge in migrating cells. Methods Cell Biol. *79*, 295-319.

Takei, K., McPherson, P.S., Schmid, S.L., and De Camilli, P. (1995). Tubular membrane

invaginations coated by dynamin rings are induced by GTPgamma S in nerve terminals. Nature *374*, 186-190.

Takei, K., Slepnev, V.I., Haucke, V., and De Camilli, P. (1999). Functional partnership between amphiphysin and dynamin in clathrin-mediated endocytosis. Nat. Cell Biol. *1*, 33-39.

ter Beest, M.B., Chapin, S.J., Avrahami, D., and Mostov, K.E. (2005). The role of syntaxins in the specificity of vesicle targeting in polarized epithelial cells. Mol. Biol. Cell *16*, 5784-5792.

Thapa, N., Sun, Y., Schramp, M., Choi, S., Ling, K., and Anderson, R.A. (2012). Phosphoinositide signaling regulates the exocyst complex and polarized integrin trafficking in directionally migrating cells. Dev. Cell *22*, 116-130.

Tian, A., and Baumgart, T. (2009). Sorting of lipids and proteins in membrane curvature gradients. Biophys. J. *96*, 2676-2688.

Vasan, N., Hutagalung, A., Novick, P., and Reinisch, K.M. (2010). Structure of a C-terminal fragment of its Vps53 subunit suggests similarity of Golgi-associated retrograde protein (GARP) complex to a family of tethering complexes. Proc. Natl. Acad. Sci U.S.A. *107*, 14176-14181.

Weber, T., Zemelman, B.V., McNew, J.A., Westermann, B., Gmachl, M., Parlati, F., Söllner, T.H., and Rothman, J.E. (1998). SNAREpins: minimal machinery for

membrane fusion. Cell *92*, 759-772.

Wickner, W., Schekman, R. (2008). Membrane fusion. Nat. Struct. Mol. Biol. *15*, 658-664.

Wickner, W. (2010). Membrane fusion: five lipids, four SNAREs, three chaperones, two nucleotides, and a Rab, all dancing in a ring on yeast vacuoles. Annu. Rev. Cell Dev. Biol. *26*, 115-136.

Wiederkehr, A., De Craene, J.O., Ferro-Novick, S., and Novick, P. (2004). Functional specialization within a vesicle tethering complex: bypass of a subset of exocyst deletion mutants by Sec1p or Sec4p. J. Cell Biol. *167*, 875-887.

Yamashita, M., Kurokawa, K., Sato, Y., Yamagata, A., Mimura, H., Yoshikawa, A., Sato, K., Nakano, A., and Fukai, S. (2010). Structural basis for the Rho- and phosphoinositide-dependent localization of the exocyst subunit Sec3. Nat. Struct. Mol. Biol. *17*, 180-186.

Yang, C., Czech, L., Gerboth, S., Kojima, S., Scita, G., and Svitkina, T. (2007). Novel roles of formin mDia2 in lamellipodia and filopodia formation in motile cells. PLoS Biol. *5*, e317.

Yang, C., Hoelzle, M., Disanza, A., Scita, G., and Svitkina, T. (2009). Coordination of membrane and actin cytoskeleton dynamics during filopodia protrusion. PLoS One *4*, e5678.

Yang, C., and Svitkina, T. (2011).Filopodia initiation: focus on the Arp2/3 complex and formins. Cell Adh. Migr. *5*, 402-408.

Yin, Y., Arkhipov, A., and Schulten, K. (2009). Simulations of membrane tubulation by lattices of amphiphysin N-BAR domains. Structure *17*, 882-892.

Yu, I.M., and Hughson, F.M. (2010). Tethering factors as organizers of intracellular vesicular traffic. Annu. Rev. Cell Dev. Biol. *26*, 137–156.

Zhang, X., Wang, P., Gangar, A., Zhang, J., Brennwald, P., TerBush, D., and Guo, W. (2005). Lethal giant larvae proteins interact with the exocyst complex and are involved in polarized exocytosis. J. Cell Biol. *170*, 273-283.

Zhang, X., Orlando, K., He, B., Xi, F., Zhang, J., Zajac, A., and Guo, W. (2008). Membrane association and functional regulation of Sec3 by phospholipids and Cdc42. J .Cell Biol. *180*, 145-158.

Zhao, Y., and Guo, W. (2009). Sec-ure nanotubes with RalA and exocyst. Nat. Cell Biol. *11*, 1396-1397.

Zhao, H., Pykalainen, A. and Lappalainen, P. (2011). I-BAR domain proteins: linking actin and plasma membrane dynamics. Curr. Opin. Cell Biol. *23*, 14-21.

Zhao, Y., Liu, J., Yang, C., Capraro, B.R., Baumgart, T., Bradley, R.P., Ramakrishnan, N., Xu, X., Radhakrishnan, R., Svitkina, T., Guo, W. (2013). Exo70 generates membrane curvature for morphogenesis and cell migration. Dev. Cell. *26*, 266-278.

Zimmerberg, J., and Kozlov, M.M. (2006). How proteins produce cellular membrane curvature. Nat. Rev. Mol. Cell Biol. *7*, 9-19.

Zuo, X., Zhang, J., Zhang, Y., Hsu, S.C., Zhou, D., and Guo, W. (2006). Exo70 interacts with the Arp2/3 complex and regulates cell migration. Nat. Cell Biol. *8*, 1383-1388.